SURFACE PLASMONIC CORE-SHELL PARTICLES FOR SOLAR ENERGY HARVESTING

by

Bo Ding

ME, Zhejiang University, China, 2008

BE, Tianjin University, China, 2006

Submitted to the Graduate Faculty of

the Swanson School of Engineering in partial fulfillment

of the requirements for the degree of

Doctor of Philosophy

University of Pittsburgh

2014

UNIVERSITY OF PITTSBURGH

SWANSON SCHOOL OF ENGINEERING

This dissertation was presented

by

Bo Ding

It was defended on

July 10th, 2013

and approved by

Jung-Kun Lee, PhD, Associate Professor, Department of Mechanical Engineering and Materials Science

Paul W. Leu, PhD, Assistant Professor, Department of Industry Engineering

John A. Barnard, PhD, Professor, Department of Mechanical Engineering and Materials Science

Ian Nettleship, PhD, Associate Professor, Department of Mechanical Engineering and Materials Science

Guofeng Wang, PhD, Assistant Professor, Department of Mechanical Engineering and Materials Science

Dissertation Director: Jung-Kun Lee, PhD, Associate Professor,

Department of Mechanical Engineering and Materials Science

SURFACE PLASMONIC CORE-SHELL PARTICLES FOR SOLAR ENERGY HARVESTING

Bo Ding, PhD

University of Pittsburgh, 2014

Plasmonic core-shell particles, consisting of a spherical dielectric core coated with a concentric layer of metallic nanoshell, are versatile subwavelength optical components. Their surface plasmon resonance can be tuned by simply varying the thickness of the metallic nanoshell and the diameter of the inner core. A facile two step method has been developed to synthesize core-shell particles with well coated Ag nanoshell. Embedding these plasmonic core-shell particles into TiO_2 mesoporous photoelectrode enlarges the optical cross-section of dye sensitizers coated onto the photoelectrode and increases the energy conversion efficiency of dye sensitized solar cells (DSSCs). The enhanced photon-electron conversion is attributed to localized surface plasmons of the core-shell particles, which increase the absorption and scattering of the incoming light in the photoelectrode. We also show that the extinction spectra of the photoelectrode can be effectively controlled by changing the geometric factor of the plasmonic particles. This tuning capability allows us to design the surface plasmons of the core-shell particles to maximize the absorption of the dye molecules with different optical absorption spectrum for dye sensitized solar cells. In addition, simulation has been applied based on Mie scattering theory to demonstrate the plasmon absorption and scattering effect of the core-shell particles. Furthermore, we report that the light harvesting efficiency of PbS nanoparticle solar cells is significantly increased by SiO_2@Au@SiO_2 plasmonic particles (SGSs). A mechanism underlying enhanced light harvesting of F-doped SnO_2 (FTO)/TiO_2/PbS/Au heterojunction solar cells is investigated

using both experimental and theoretical methods. Finite-difference time-domain (FDTD) simulation demonstrates that the effect of the plasmonic particles on the light absorption by PbS nanoparticles depends on the location of the plasmonic particles. When SGSs are placed between PbS and TiO_2, nanodomes are formed on a top Au layer and additional light scattering at the nanodomes is found. Our results demonstrate that SGSs can promote the light harvesting of the thin film solar cells in two ways. The first enhancement effect is due to the localized surface plasmon resonance of SGSs themselves and the second one is attributed to the increased roughness of the top Au electrode with the nandomes.

TABLE OF CONTENTS

LIST OF TABLES

LIST OF FIGURES

PREFACE

This dissertation includes some contents published/submitted in peer reviewed journal papers, and a list of journal papers is as following:

Chapter 3 Bo Ding, Bong Jae Lee, Mengjin Yang, Hyun Suk Jung and Jung-Kun Lee, Surface-Plasmon Assisted Energy Conversion in Dye-Sensitized Solar Cells, Adv. Energy Mater. 2011, 1, (3), 415-421.

Chapter 4. Bo Ding, Mengjin Yang, Bong Jae Lee, and Jung-Kun Lee, Tunable Surface Plasmons of Dielectric Core-Metal Shell Particles for Dye Sensitized Solar Cells, RSC Advances 2013, 3, (25), 9690-9697.

During my PhD study, I got a lot of help and encouragement. I would glad to express my appreciation and acknowledgement during this exciting journey.

First and foremost, I would like to thank my advisor Professor Jung-Kun Lee for his kind guidance during my PhD study. His passionate, diligent, critic-thinking influences my research tremendously. I am impressed by his knowledge, strong logic and creativity. Without his mentoring, it is impossible for me to survive and finish my PhD study.

Also, thanks a lot to the other committee members, Professor Paul W. Leu, Professor John A. Barnard, Professor Ian Nettleship and Professor Guofeng Wang. Their kindness and pertinent advice always broaden my horizons in research. Here, I especially appreciate the great help from Professor Paul W. Leu, Professor David Waldeck and Professor Bong Jae Lee, who

are the collaborators with our group. Professor Leu is very professional in nanophotonics simulation and helps me a lot in explaining and proving the plasmon effect in PbS based solar cells by theoretical calculations. Professor Waldeck is a very kind and generous expert in interfacial charge transfer and nanophotonics, and shares brilliant ideas and some test tools for my research. Professor Bong Jae Lee is a knowledgeable researcher and contributed a lot at the beginning of my study in plasmon assisted DSSCs.

I am very lucky to have great members in our dynamic group: You-Hwan Son, Mengjin Yang, Po-shun Huang, Youngsoo Jung and Salim Caliskan. They are smart and diligent. Particularly grateful to Mengjin, who helped me a lot either in research or daily life when I joined this group. Also, he setup the OCVD and SLIM-PCV systems for electron lifetime measurement, which brings convenience to solar device characterization.

Thanks to my other colleagues and friends, who give selfless collaboration and contribution to my work: Matt Barry, Yang He, Xiahan Sang, Feng Zhou, Zhongfan Zhang, Gautam Reddy, and especially Tongchuan Gao and Yang Wang, who are very smart and patient collaborators and friends. With their assistance, my research became much easier and more productive.

Moreover, thanks to Materials Science Characterization Lab and Nano-Scale Fabrication and Characterization facility, and their staffs: Albert Stewart, who is always the best staff I ever met, Cole Van Ormer, Shusheng Tan, Matthew France and Joel Gillespie.

Finally, I want to express my gratitude to my parents, who give me life and support me unconditionally and constantly.

1.0 INTRODUCTION

Surface plasmons (SPs) are a result of electromagnetic radiation induced coherent oscillations of free electrons on a metal.[1, 2] Their unique properties have attracted much attention due to its practical applications, including light guiding and manipulation at the nanoscale, high resolution optical imaging below the diffraction limit, as well as biodetection at the single molecule level. This diverse and rapidly growing field of research on such optical-metallic interactions is well known as 'plasmonics'.[3-5]

The first scientific study of surface plasmons dates back to 1902 when Prof. Robert W. Wood observed unexplained phenonema in optical reflection test on metallic gratings.[6, 7] In 1908, Gustav Mie developed his famous and widely used Mie theory, a rigorous analytical solution of Maxwell's equations for light scattering by spherical particles.[8] In 1957, Rufus Ritchie found that plasmon modes could exist near the surface of metal, which represents the first theoretical description of surface plasmons.[9] A main breakthrough was made in 1968 by Andreas Otto et al.[10, 11] who designed methods for optical excitation of surface plasmons on metallic films, facilitating experiments on surface plasmons to many other researchers.

Surface plasmon resonances (SPRs) usually can be divided into two kinds: (i) propagating surface plasmon polaritons (SPPs) and (ii) nonpropagating localized surface plasmon resonances (LSPRs).[12] The SPP, firstly introduced by Stephen Cunningham et al. in 1974,[13] can be excited on the thin metallic film by using prism or grating couplers. LSPR is

excited by ordinary or nonevanescent propagating light, and intimately coupled to such light as well. In other words, it is nonpropagating plasmon excitations that can be resonantly excited on metal nanoparticles (NPs) or in metal films. These two types of SPRs propagate along the metal film with an associated electric field which decays normally and exponentially from the metal-dielectric interface.[14] In addition, the plasmon resonance peak can be shifted by changing the refractive index above the metal.

1.0.1 Plasmonic Metal Nanoparticles

Nobel metal NPs, especially gold (Au) and silver (Ag), are frequently studied due to their strong SPRs in the visible wavelength range.[15] The incident photon frequency can be resonant with collective oscillation of the free electrons in the metal NPs, causing LSPRs. The free electrons in the particle will all move in phase under plane-wave excitation, leading to a buildup polarization charges on the surface of the particle as a restoring force (Fig. 1-1).[16] This restoring force will allow a resonance to occur at a specific frequency named particle dipole plasmon frequency. In the meanwhile, a dipolar field is produced outside, resulting in an intensified surface plasmon absorption band, and enhanced near-field in the vicinity of the particle surface. The absorption bandwidth and the position and intensity of the maximum absorption peak is determined by the material, as well as its morphology and dimension.[17]

Thanks to the talented chemist and physicist, in the past decades, various synthetic methodologies for generating nanostructures with well controlled sizes and shapes from a variety of materials were set up.[18-21] By this way, plasmonic metal nanostructures with different morphologies and dimensions, like spheres,[22] cubes,[23, 24] rods[25, 26] and plates[27] were designed, merging the ability to accurately control and tailor their optical properties.[28, 29]

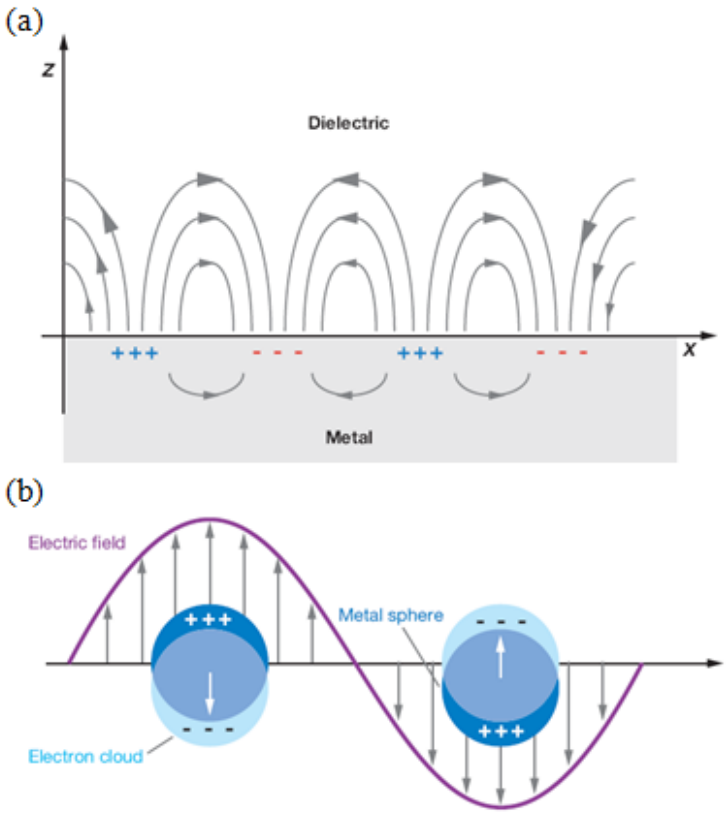

Figure 1-1. Schematic diagrams illustrating (a) a surface plasmon polariton and (b) a localized surface plasmon [16]

1.0.2 Plasmonic Nanoparticles Composed of Dielectric Core - Metal Shell

Plasmonic core-shell particles, consisting of a spherical dielectric core coated with a concentric layer of metallic nanoshell, are versatile subwavelength optical components, whose surface plasmon resonance can be tuned by simply varying the thickness of the metallic nanoshell and the diameter of the inner core.[30, 31] So far, the well prepared and widely used plasmonic core shell particles is Au shell – silica core nanostructures.[32] Researchers[33, 34] developed a mature Au seed mediated two step method to form gold shell – silica core structures. The thickness of the Au shell can be modified by readily changing the amount of pre-added $HAuCl_4$ in the reacting

solution. By varying the core size and shell thickness, the optical property of this plasmonic structure can be readily tuned (Fig. 1-2).[35]

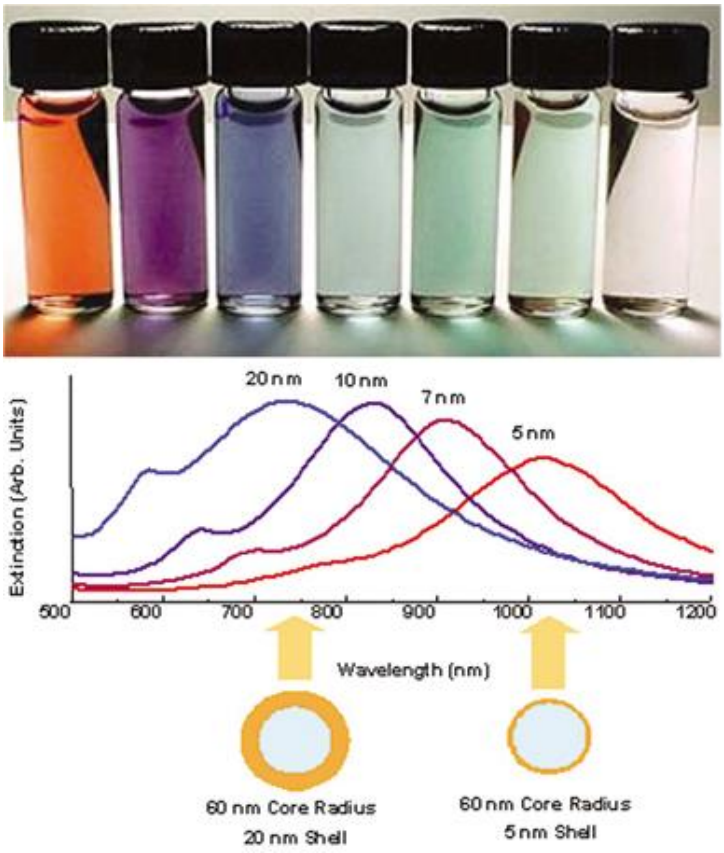

Figure 1-2. Visual demonstration of the tunability of metal nanoshells (top), and optical spectra of Au shell – silica core nanostructures as a function of their core/shell ratio [35]

The plasmonic properties of this composite nanostructure can be understood as a hybridization of the surface plasmons on the inner and outer surfaces of the metallic shells. The shell thickness corresponds to the interparticle distance of a plasmonic dimer,[36] Within the shell, the lowest energy mode has a symmetric charge distribution, which is similar to that of the surface plasmons of a thin metal film.[37] Halas and co-workers[38] established a sphere-cavity mode to explain the plasmon hybridization of the nanoshell (Fig. 1-3). Two simpler plasmons, of a solid metallic sphere and of a cavity, were introduced in the mode. In the nanoshell, a strong

dipole corresponds to the lowest energy ω_-, or 'bonding' plasmon, and a smaller dipole due to antisymmetric charge distribution corresponds to higher energy ω_+, or 'anti-bonding' plasmon. Only the lower energy plasmon interacts strongly with the incident optical field, so when the thickness of the nanoshell decreases, the plasmon shifts to lower energies, meaning stronger coupling with the incident optical field. This mode was further applied to multilayer metallodielectric nanomatryushkas.[39]

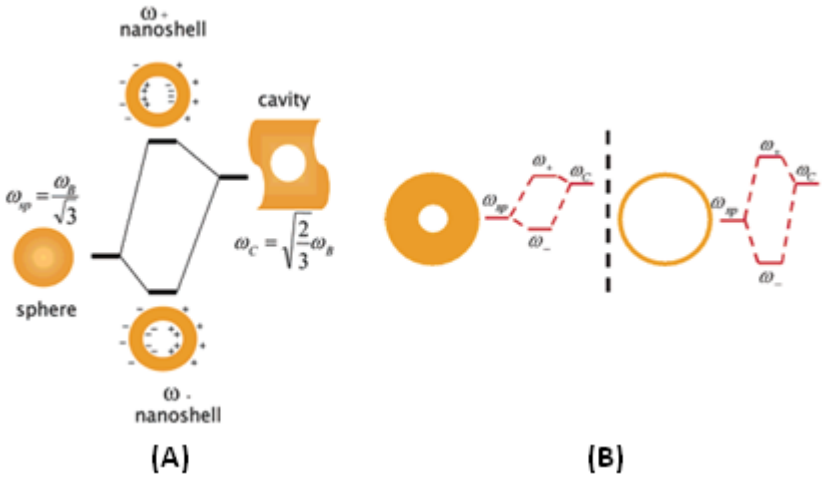

Figure 1-3. Energy level diagrams (A) depicting plasmon hybridization in metal nanoshells resulting from interacting sphere and cavity plasmons with two hybridized plasmon modes and (B) illustrating the dependence of nanoshell plasmon energies [38]

1.1 DYE SENSITIZED SOLAR CELLS

Dye sensitized solar cell (DSSC), also known as Grätzel cell, was first introduced in 1991.[40] This kind of photoelectrochemical cell is different from traditional silicon based solar cell, in which electron-hole pair is separated by the built-in potential of p-n junction. However, light absorption and charge separation are fulfilled by the association of photosensitizers with wide band gap

semiconductors. The theoretical efficiency of the DSSC is as high as 19.6 % and very compatible to that of commercial silicon based solar cell.[41] Furthermore, several other advantages, like low fabrication cost, easy scale-up using flexible substrate, and good performance under weak/diffuse light, make DSSC to be a promising alternative to high cost and polluted silicon industry in the future. During the last two decades, DSSCs have been greatly studied, leading to a great increase of the cell performance. So far, the best efficiency of the DSSCs in the lab scale has already surpassed 11 %.[42, 43] And the manufacturers, like Sharp and Sony, announce that the submodule efficiencies have been reaching up to 10.4 % and 9.2 % separately,[44] which means a pioneer footstep to commercial market.

The principle of operation and energy level scheme of the DSSCs are shown in Figure 1-4.[45] In the DSSC, organic dye molecule, which is comparable with chlorophyll in green plants for natural photosynthesis, works as the photosensitizer. Typically, the dye molecules absorb incoming photons and generate electron-hole pairs. The electrons are then quickly separated from the counterpart holes at the interface of sensitizer and semiconductor, and then injected into the conduction band of the oxide semiconductor mesoporous film before being recombined. The dye molecules are later regenerated by a redox system in the electrolyte to fulfill a circle. The monochromatic current yield can be expressed by the equation η_i (λ) = LHE (λ) × $Ø_{inj}$ × η_e, in which LHE (light harvesting efficiency) is the fraction of the incident photons absorbed by dye, $Ø_{inj}$ is the quantum yield for charge injection and η_e is the charge collection efficiency at the back contact.

The maximum output voltage generated under illumination is equal to the difference between the Fermi level of the semiconductor and the redox potential of the electrolyte.

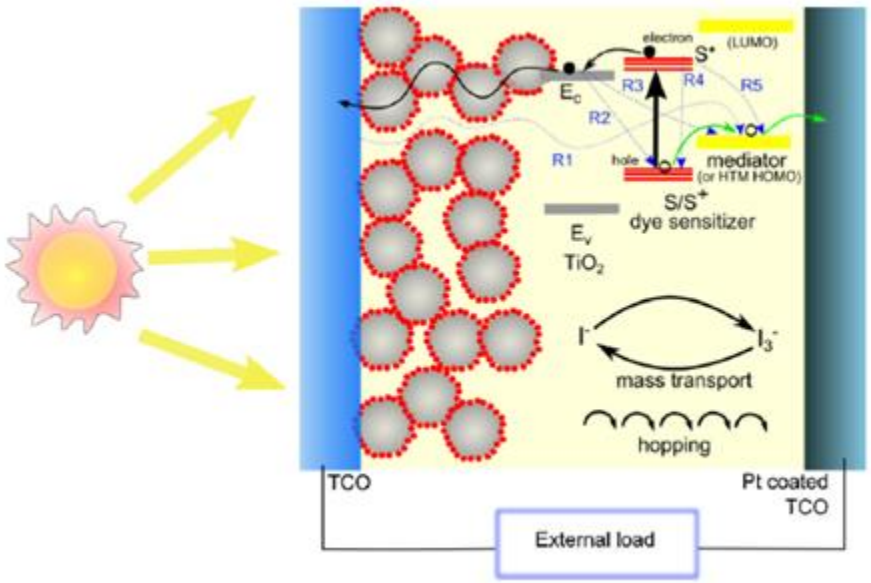

Figure 1-4. DSSC structure and energy band alignment superposition diagram [45]

The photosensitizer plays a critical role in generating electron-hole pairs in the DSSC. Although quantum dots such as CdSe[46] and PbSe[47] were employed as the sensitizing materials recently, organic dyes containing polypyridyl complex of ruthenium (Ru) are widely used as the photosensitizer due to its high efficiency and long term stability.

The photoanode acts as electron transport path, light path, and dye anchoring scaffold. The use of TiO_2 nanocrystals with high surface area in DSSCs matches the lowest unoccupied molecular orbital (LUMO) and the conduction level of the anodes and improves the charge transfer properties, leading to high energy conversion efficiency.[48]

Electrolyte works as an electron-transfer mediator which regenerates the dye sensitizer from its oxidized state. So far, liquid electrolytes are mostly common used because of the effective catalytic reaction at the counter electrode and its fast ionic diffusion. Although some new redox systems, such as Br^-/Br_3^-,[49] cobalt (II/III),[50] disulfide / thiolate,[51] and ferrocene / ferrocenium[52] redox mediator, have been investigated, they are still unrivaled to conventional I^- /

I_3^- electrolyte, which keeps the record efficiency of 12 %,[42] for its very low recombination kinetic between electrons in TiO_2 and triiodide.[53] However, liquid volatile electrolyte will cause leaking problem under thermal and light-soaking dual stress, and evaporation of the organic solvent drops the long-term stability of the cell.[54] Recently, solvent-free ionic liquid electrolyte,[55] solid-state electrolyte[56, 57] and quasi-solid electrolyte[58, 59] have been explored to overcome the weakness of the liquid electrolyte and enhance the long stability of the DSSC.

1.2 APPLICATION OF THE PLASMONIC STRUCTURES

1.2.1 Photovoltaic

Photovoltaics (PVs), conversion of solar energy to electricity, has been growing rapidly and attracting much attention of researchers and government energy agencies, due to the urgent global demand for renewable energy sources. In order to lower the production cost and make large scale PV panel, thin film solar cell has become the main trend,[60] and convenient roll-to-roll technique is applied for flexible module fabrication.[61] In addition, thin film with thickness smaller than the carrier diffusion length (L_n) would greatly suppress the bulk recombination. Apart from above mentioned DSSC, various semiconductors have been used for thin film solar cell, such as monocrystalline and polycrystalline silicons, GaAs, CdTe and $CuInSe_2$, as well as organic semiconductors.[62] One major limitation of the thin film solar cell is that the absorbance of near-bandgap light is suppressed due to small light path length. However, traditional light trapping method, using pyramidal surface texture,[63] is not proper to thin film solar cell, since the

surface roughness would surpass the film thickness, and minority carrier recombination is increased due to larger surface area and junction regions.

Plasmon has been considered as a useful tool for light harvesting in thin film solar cells due to resonances and electromagnetic field enhancements and light path folding effect.[64] Prof. Atwater argued that three ways would be applied for light harvesting by plasmonic structures in PVs (Fig. 1-5).[65] (a) The light path length can be exponentially increased by multiple and high angle scattering with metallic nanoparticles, trapping and folding the light in the thin absorber layer. (b) Light can be trapped by the excitation of localized surface plasmons on the metal nanoparticles. The photon induced plasmonic near-field will be coupled to the semiconductor to increase the effective optical cross-section, causing the creation of electron-hole pairs in the thin film. (c) If applying a corrugated metallic film on the back surface of the thin semiconductor film, light will be trapped by the excitation of surface plasmon polaritons (SPPs) at the interface of metal and semiconductor.

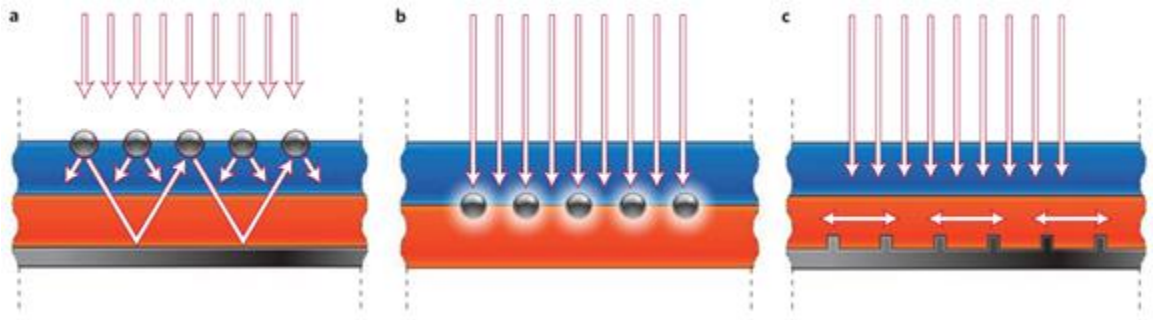

Figure 1-5. Plasmonic light-trapping geometries for thin-film solar cells. a, Light trapping by scattering from metal nanoparticles. b, Light trapping by the excitation of localized surface plasmons on metal nanoparticles. c, Light trapping by the excitation of surface plasmon polaritons at the metal/semiconductor interface [65]

Due to the unique plamonic properties, metallic nanostructures have been largely employed in thin film PVs with various methods, resulting in an improved photocurrent and energy conversion efficiency. Such as embedding metal nanoparticles in single-crystalline Si,[66] contacting Ag film in organic solar cells,[67] and mixing small metal clusters in DSSCs.[68]

1.2.2 Other Applications

1.2.2.1 Surface-Enhanced Raman Spectroscopy

Raman spectroscopy is a very useful tool for capturing molecule-specific data, since the Raman signal contains detailed information of the molecule vibration. However, it lacks the intrinsic sensitivity required for high output detection due to weak signal intensity. To address this problem, plasmonic nanostructures were employed for signal enhancement. A million-fold enhancement can be realized attributing to excitation of surface plasmons of the metallic substrate.[69] The strong local fields at the metal surface coupled with its plasmon resonance are responsible for this dramatic enhancement. This high sensitivity of surface-enhanced Raman scattering (SERS) can even be applied to much complex environment, like inside live cells.[70] Researchers later found that aggregated Au and Ag clusters or films had larger enhancement effect than individual metal nanoparticle, for the high-field intensities are associated with dimer plasmons or junctions between neighbor nanoparticles.[71]

SERS in near-infrared region has become a very attracting research area, since unwanted background fluorescence from molecules is dramatically suppressed when probing chemical complex environments, and Raman scattering signal is much weaker in infrared region than that of visible wavelengths. In order to solve this problem, metal nanoshells are designed, and the

plasmon resonance is tuned near the pump laser wavelength via changing the geometry of the core-shell nanostructures.[72] Three Stokes modes were applied to understand the nanoshell accompanied SERS. And the significant enhancement was found when absorption of the Stokes emission is minimized.[73]

1.2.2.2 Photoacoustic Signal Nanoamplifiers

Photoacoustic is the effect of absorbed light on matter by means of acoustic detection. This phenomenon was firstly discovered by Alexander Graham Bell in 1880 that is after exposing to sunlight, a thin disc produced sound in response. Photoacoustic was originally controlled by an energy conversion procedure from light to local heating. Later on, photoacoustic imaging technology was developed by applying a laser pulse on an object, and photogenerated heat was expanded and captured by a remote sensor as acoustic wave. The distribution of optical absorption within such object can be depicted as acoustic field.[74] The contrast of photoacoustic imaging depends upon the optoacoustic efficiency, which is determined by the number of absorbed incident photons for heat generation and the speed of heat release during thermal expansion and wave generation.[75] Au nanostructures have usually been chosen as contrast and therapeutic agents due to their excellent plasmonic effect.[76] The photoacoustic contrast can be optimized by maximizing the optical absorption cross section of the metallic nanostructures. So far, Au nanorods,[77] nanocages[78] and nanoshells[79] have been successfully applied as the photoacoustic amplifier. The photoacoustic imaging system and typical image are shown in Figure 1-6.

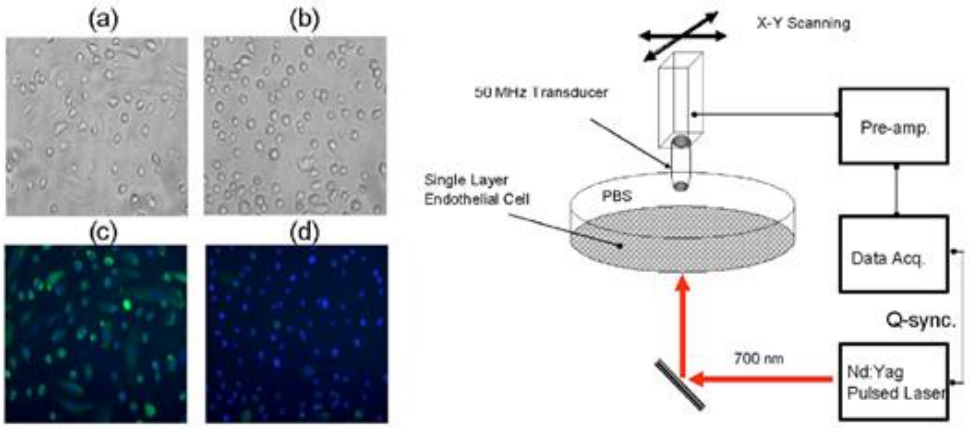

Figure 1-6. Left: microscope images of (a) stimulated and (b) unstimulated cells. Fluorescence images of (c) stimulated and (d) unstimulated cells. Right: Photoacoustic imaging system [74]

1.3 CHALLENGES OF METALLIC CORE-SHELL PARTICLES

As described above, metallic nanoshell - silica core structures have unique properties that advance current technology in the fields of photovoltaics, SERS, and photoacoustic imaging. However, several issues still have to be addressed to maximize the potential of plasmonic core-shell structures.

First of all, although Au nanoshell - silica core ($Au@SiO_2$) structures have been well prepared and widely used so far, another noble element Ag has been less considered as a plasmonic core-shell structure, due to lacking of effective method to synthesize complete Ag nanoshell – silica core ($Ag@SiO_2$) particles. Ag nanoshell owns some unique optical properties, like strong scattering spectrum and tunable blue shifted extinction (absorption + scattering) spectrum. In addition, Ag has stronger resonance strength[80] and much cheaper cost than Au, so there is no reason to hide it from shining. Several methods, like sonication,[81] seed mediation[82] and electroless plating,[83, 84] have been explored for $Ag@SiO_2$ preparation, however, only Ag nanoparticles or nanoclusters have been achieved for surface decorating instead of forming complete Ag nanoshells. Therefore, it is required to develop a new way to form complete Ag nanoshell on silica core. Figure 1-7 shows the TEM images of the incomplete Ag nanoshell – silica core particles prepared by previous trials.

Second issue is that no metallic shell - dielectric core plasmonic structures have been applied in DSSCs. Although plasmonic nanoparticles have been widely used in various PVs as we discussed before, however, only until very recently, metal nanoparticles have been investigated in DSSCs.[85, 86] Since plasmonic core – shell particles are considered to have strong

localized surface plasmons and optical scattering capability, they have the potential for light harvesting enhancement in DSSCs.

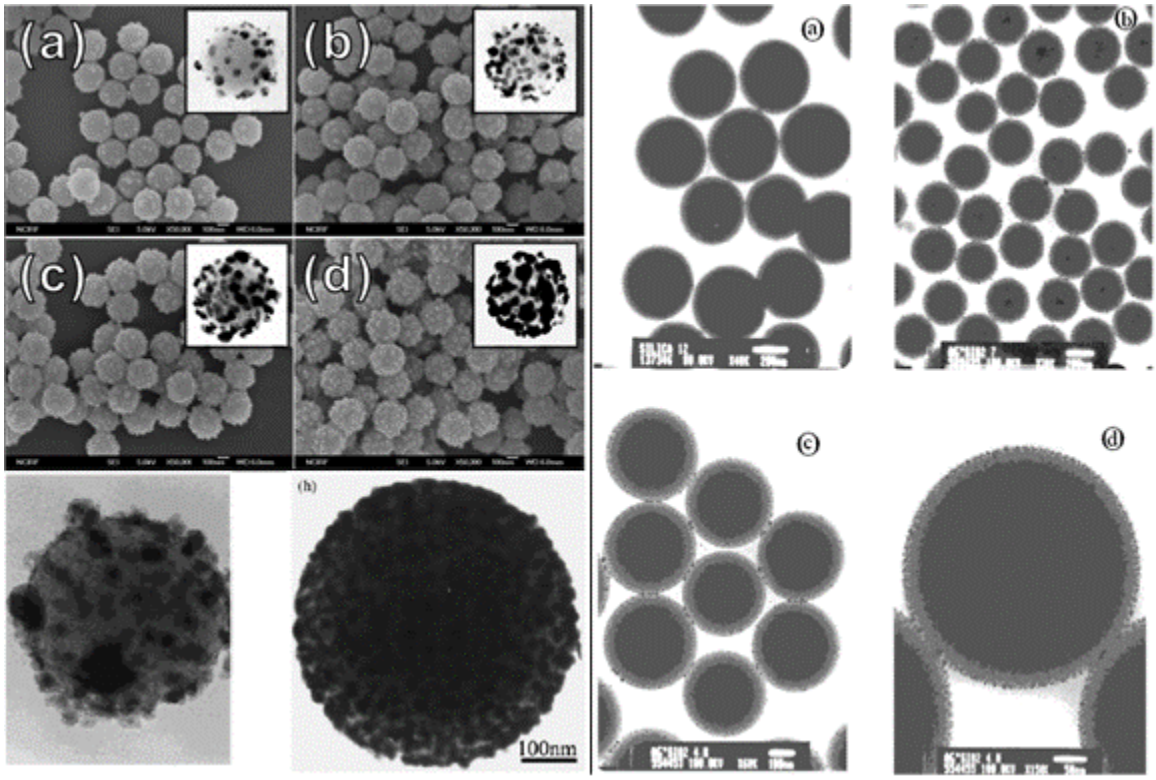

Figure 1-7. TEM images of incomplete Ag nanoshells with silica cores [81-84]

The third concern is that the dye molecule, photosensitizer in DSSCs, can only cover a specific partial of solar spectrum, so plasmonic core – shell particles are expected to intensify and broaden its absorption peak. However, different dye molecule preserves unmatchable absorption spectrum (Figure 1-8), so one kind of core – shell particles might be not proper to fulfill demands from all kinds of dyes. To address this problem, the optical properties of the plamonic structures will be tuned by changing the dimension of the core and thickness of the metallic nanoshell.

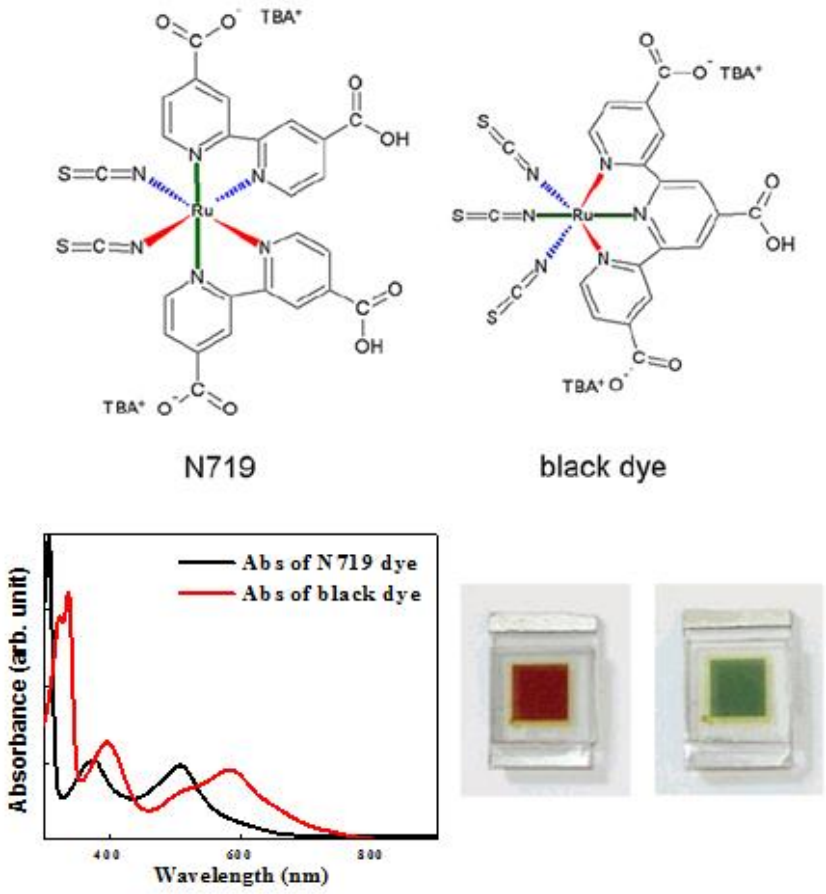

Figure 1-8. (Top) Molecule structures of N719 and black dyes. (Bottom left) Absorption spectra of N719 and black dyes. (Bottom right) Prototype DSSCs employing N719 and black dyes

2.0 OPTICAL SIMULATION OF PLASMONIC STRUCTURES

2.1 MOTIVATION

Surface plasmons can be successfully described by macroscopic electromagnetic theory, and the most classical one is Maxwell's equations.[87] Although, strictly speaking, this theory is applicable in a macroscopic sense, however, so far, it has been well extrapolated to the region of nanometer scale.[88] The Maxwell's equations describe how electric charges and currents influence electric and magnetic fields. Typically, four equations are included to describe the electromagnetic field at a time *t* and any point *r* in a medium characterized by their bulk dielectric constant $\varepsilon(r, t)$ and magnetic permeability $\mu(r, t)$. Conceptually, Gauss's law and Gauss's law for magnetism describe how charges emanate fields, and Ampere's law and Faraday's law depict how fields circulate around relevant sources. The differential form of the equations is defined below, in which *E* is the electric field, ρ the charge density, *B* the magnetic induction, *H* the magnetic field, *J* the current density, and *D* the displacement.

$$\nabla \cdot E(r,t) = \rho(r,t) \qquad \text{(Gauss's Law)} \qquad (1.1)$$

$$\nabla \cdot B(r,t) = 0 \qquad \text{(Gauss's Law for Magnetism)} \qquad (1.2)$$

$$\nabla \times H(r,t) = J(r,t) + \frac{\partial D(r,t)}{\partial t} \quad \text{(Ampere's Law)} \tag{1.3}$$

$$\nabla \times E(r,t) = -\frac{\partial B(r,t)}{\partial t} \quad \text{(Faraday's Law)} \tag{1.4}$$

Above classical Maxwell's equations are not sufficient in themselves, and constitutive relations are needed as well. These relations have the form as follows where P is the electric polarization, M the magnetization, σ the conductivity. In addition, μ and χ are the permeability and electric susceptibility of the medium separately; ε_0 and μ_0 are the permittivity and permeability of the free space individually.

$$D = \varepsilon_0 E + P \tag{1.5}$$

$$H = \frac{B}{\mu_0} - M \tag{1.6}$$

$$J_F = \sigma E \tag{1.7}$$

$$B = \mu H \tag{1.8}$$

To solve the optical scattering problem, two parameters have to be considered: d, the physical size of the scattering object and λ, the wavelength of electromagnetic waves. For one extreme case when $d >> \lambda$, the problem is readily solved without involving Maxwell's equations. With respect to another limiting case when $d << \lambda$, the solution in the quasistatic limit is obtained by invoking Laplace's equation. However, the problem is further more complicated when $d \sim \lambda$. In this case, many numerical methods have been developed to fulfill the requirement, such as Green dyadic method (GDM),[89] discrete dipole approximation (DDA),[90-92] finite-difference frequency-domain method,[93] and finite-difference time-domain (FDTD).[94] In particular, to obtain

a FDTD solution of Maxwell's equation, a computational domain is established first to describe the corresponding physical region in the sample, and every point within the computational domain needs to be processed to describe the electric or magnetic field around the whole region. The advantage of these numerical methods is that it can be applied to objects with arbitrary geometries. However, these methods are based on discretization of the fields on a numerical grid, and a very fine grid resolution is necessary at the metal-dielectric interface to resolve the local fields adequately. As a result, more coding complexity leads to less calculation efficiency.

Another way is to use analytical method, e.g. Mie theory. Based on this theory, the incident plane wave and the scattering field are expanded into radiating spherical vector wave functions. On the other hand, the internal field is expanded into regular spherical vector wave functions. Finally, the expansion coefficients of the scattered field can be calculated by applying the boundary condition on the spherical surface.[95] Although this method, in principle, can only be applied to objects with specific shapes, such as planar geometries, spheres and cylinders, to some extent, it is still applicable to nonspherical particles.[15] In sum, the Mie theory is far more eligible to depict and calculate the optical properties of plasmonic nanoparticles and core-shell structures in most cases.

2.2 SIMULATION OF PLASMONIC CORE-SHELL PARTICLES

2.2.1 Formulas for Optical Simulation of Silver Nanoparticles

Based on the excellent descriptions of Mie Scattering by Bohren and Huffman,[15] Mie calculations are realized by applying formulas below in MATLAB. For simulation of

homogeneous spheres, the key parameters are the Mie coefficients a_n, b_n, c_n and d_n, which are defined by equation 4.1-4.4. The amplitude of the scattered field can be computed from parameter a_n and b_n, and internal field from c_n and d_n.

$$a_n = \frac{m^2 j_n(mx)[x j_n(x)]' - \mu_1 j_n(x)[mx j_n(mx)]'}{m^2 j_n(mx)\left[x h_n^{(1)}(x)\right]' - \mu_1 h_n^{(1)}(x)[mx j_n(mx)]'} \tag{4.1}$$

$$b_n = \frac{\mu_1 j_n(mx)[x j_n(x)]' - j_n(x)[mx j_n(mx)]'}{\mu_1 j_n(mx)\left[x h_n^{(1)}(x)\right]' - h_n^{(1)}(x)[mx j_n(mx)]'} \tag{4.2}$$

$$c_n = \frac{\mu_1 j_n(x)\left[x h_n^{(1)}(x)\right]' - \mu_1 h_n^{(1)}(x)[x j_n(x)]'}{\mu_1 j_n(mx)\left[x h_n^{(1)}(x)\right]' - h_n^{(1)}(x)[mx j_n(mx)]'} \tag{4.3}$$

$$d_n = \frac{\mu_1 m j_n(x)\left[x h_n^{(1)}(x)\right]' - \mu_1 m h_n^{(1)}(x)[x j_n(x)]'}{m^2 j_n(mx)\left[x h_n^{(1)}(x)\right]' - \mu_1 h_n^{(1)}(x)[mx j_n(mx)]'} \tag{4.4}$$

In above equations, m is the refractive index of the sphere relative to the ambient medium; a is the average radius of the spherical particles; x, the production of k and a, is the size parameter; k, which is equal to $2\pi/\lambda$, is the wave number of the electromagnetic wave; λ is the corresponding wavelength. In addition, μ_1 is the ratio of the magnetic permeability of the particle to that of the ambient medium. The spherical Bessel functions, $j_n(z)$ and $h_n^{(1)}$, are involved in Mie coefficients calculation. $h_n^{(1)}$ can be obtained by defining

$$h_n^{(1)} = j_n(z) + i y_n(z) \tag{4.5}$$

The primes mean derivatives, which following from the spherical Bessel functions themselves

$$[zj_n(z)]' = zj_{n-1}(z) - nj_n(z) \tag{4.6}$$

$$[zh_n^{(1)}(z)]' = zh_{n-1}^{(1)}(z) - nh_n^{(1)}(z) \tag{4.7}$$

The relationships between Bessel and spherical Bessel functions are expressed as

$$j_n(z) = \sqrt{\frac{\pi}{2z}} J_{n+0.5}(z) \tag{4.8}$$

$$y_n(z) = \sqrt{\frac{\pi}{2z}} Y_{n+0.5}(z) \tag{4.9}$$

where J_n and Y_n are Bessel functions of the first and second kind. The recurrence formula is defined as

$$f_{n-1}(z) + f_{n+1}(z) = \frac{2n+1}{z} f_n(z) \tag{4.10}$$

and for n = 0 and 1, we have initial functions

$$j_0(z) = sinz/z; \qquad y_0(z) = -cosz/z \tag{4.11}$$

$$j_1(z) = sinz/z^2 - cosz/z; \qquad y_1(z) = -cosz/z^2 - sinz/z \tag{4.12}$$

The optical efficiencies *Qi*, which describe the interaction of radiation with a scattering sphere, can be calculated by the cross section σ_i and geometrical particle cross section πa^2, shown as

$$Q_i = \frac{\sigma_i}{\pi a^2} \tag{4.13}$$

Since extinction is equal to the summation of absorption and scattering, energy conservation deduces the following expression

$$Q_{ext} = Q_{abs} + Q_{sca} \tag{4.14}$$

where Q_{sca} is obtained from the integration of the scattered power on all directions, and Q_{sca} can be deduced from forward-scattering theorem, as

$$Q_{sca} = \frac{2}{x^2}\sum_{n=1}^{\infty}(2n+1)(|a_n|^2 + |b_n|^2) \tag{4.15}$$

$$Q_{ext} = \frac{2}{x^2}\sum_{n=1}^{\infty}(2n+1)Re(a_n + b_n) \tag{4.16}$$

2.2.2 Formulas for Optical Simulation of Ag@SiO_2 Nanostructures

For silver nanoshell - silica core particles, Mie coefficients a_n and b_n are sufficient enough to compute cross sections and scattering diagrams. The corresponding formulas are shown as

$$a_n = \frac{(\tilde{D}_n/m_2 + n/y)\psi_n(y) - \psi_{n-1}(y)}{(\tilde{D}_n/m_2 + n/y)\xi_n(y) - \xi_{n-1}(y)} \tag{4.17}$$

$$b_n = \frac{(m_2\tilde{G}_n + n/y)\psi_n(y) - \psi_{n-1}(y)}{(m_2\tilde{G}_n + n/y)\xi_n(y) - \xi_{n-1}(y)} \tag{4.18}$$

$$\tilde{D}_n = \frac{D_n(m_2y) - A_n\chi_n'(m_2y)/\psi_n(m_2y)}{1 - A_n\chi_n(m_2y)/\psi_n(m_2y)} \tag{4.19}$$

$$\tilde{G}_n = \frac{D_n(m_2y) - B_n\chi_n'(m_2y)/\psi_n(m_2y)}{1 - B_n\chi_n(m_2y)/\psi_n(m_2y)} \tag{4.20}$$

$$A_n = \psi_n(m_2x)\frac{mD_n(m_1x) - D_n(m_2x)}{mD_n(m_1x)\chi_n(m_2x) - \chi_n'(m_2x)} \tag{4.21}$$

$$B_n = \psi_n(m_2x)\frac{D_n(m_1x)/m - D_n(m_2x)}{D_n(m_1x)\chi_n(m_2x)/m - \chi_n'(m_2x)} \tag{4.22}$$

$$m = \frac{m_2}{m_1} \tag{4.23}$$

where a is the kernel radius and b is the outer radius, and m_1 and m_2 are the refractive index of the inner core and outer shell, separately. Size parameters of the model are $x = ka$ and $y = kb$. $\psi_n(z)$, $\chi_n(z)$ and $\xi_n(z)$ are called Riccati-Bessel functions and can be expressed as

$$\psi_n(z) = z j_n(z) \tag{4.24}$$

$$\chi_n(z) = -z y_n(z) \tag{4.25}$$

$$\xi_n(z) = z h_n^{(1)}(z) \tag{4.26}$$

The logarithmic derivative D_n is given by

$$D_n = \frac{\psi_n'(mx)}{\psi_n(mx)} = \frac{[mx \cdot j_n(mx)]'}{mx \cdot j_n(mx)} \tag{4.27}$$

The optical efficiencies Qi of the metallic shell – dielectric core structures can be derived from the same functions (4.14 - 4.16) metioned before.

2.2.3 Results and Discussions

The absorption and scattering efficiencies were calculated for Ag nanoparticle (d=10 nm), SiO_2 particle (d=320 nm), and Ag nanoshell with SiO_2 core (d=340 nm) and Ag film (thickness = 10 nm). In the calculation, the Mie scattering coefficients of the core-shell particles were calculated in two different ways. In the first case, it is assumed that the Ag film is a collection of individual Ag nanoparticles on a SiO_2 core and there is no interaction between Ag nanoparticles. In the

second case, the Ag layer was treated in a way similar to multilayer thin films.[96] Here, the dielectric function of Ag was calculated using the Drude critical point model, and the refractive index of the surrounding medium was approximated as 2.37 by considering the mixed phases in the TiO_2 - core-shell mixed films.[94]

Figure 2-1 shows two different results for the absorption efficiency (i.e., absorption cross section divided by cross sectional area) of the core-shell particles. The absorption efficiency of Ag nanoparticles (10 nm) dramatically increases by almost two orders of magnitude near the surface plasmon resonance wavelength of 556 nm. On the assumption that the Ag layer is a perfect film, the calculated absorption efficiency does not exhibit the plasmonic resonance in the visible range. The scattering efficiency (i.e., scattering cross section divided by the cross sectional area) of the core-shell particles is also plotted in Figure 2-1b. To examine the effect of SiO_2 cores, the scattering efficiency of SiO_2 particles with d = 320 nm was also calculated. In the case of Ag nanoparticles, the calculated scattering efficiency of Ag nanoparticles also displays a peak near the surface plasmon resonance. However, the assumption of the Ag film leads to monotonic increase in the calculated scattering efficiency with increasing wavelength of the incident light.

The tuning effect of the silica core – silver shell particles is shown in the simulated UV-vis spectra by changing the size of the silica cores. Here, the silver shell is set to be 10 nm, and two sizes of silica cores (d= 90 nm or 450 nm) are chosen to illustrate the size effect.

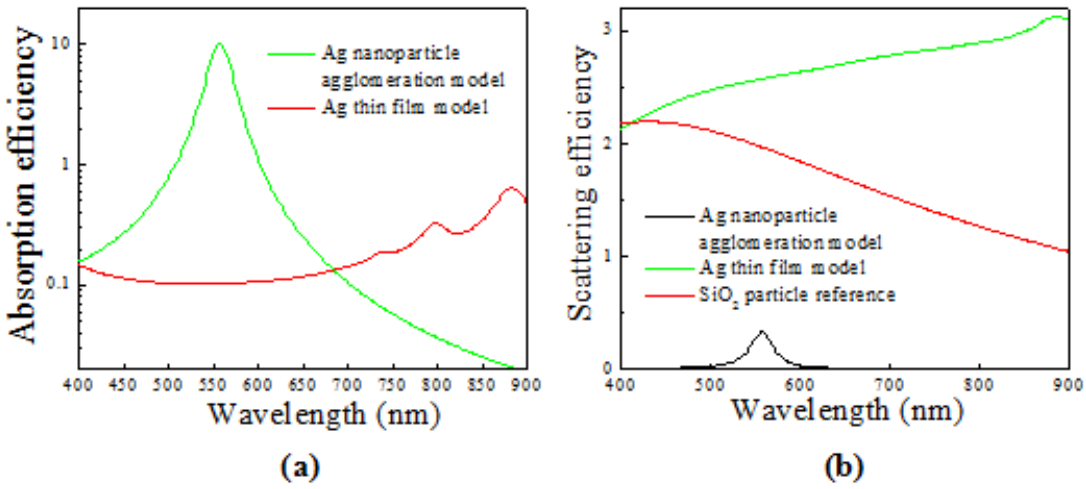

Figure 2-1. Calculated absorption efficiency (a) and scattering efficiency (b) of core-shell particles using two different models (agglomerated Ag nanoparticles and Ag thin film) showing the nature of Ag layer (the scattering efficiency of SiO_2 particles is also calculated as a reference)

Figure 2-2 shows the extinction (absorption + scattering) spectra of Ag nanoparticle (d=10 nm) and silica core – silver shell particles dispersed in water. Comparing with the strong plasmonic extinction peak at 410 nm for Ag nanoparticles, plasmon peak found near 650 nm corresponds to the Ag nanoshell with the core-shell diameter of 110 nm (Fig. 2-2a) and near 750 nm for the Ag nanoshell with the core-shell diameter of 470nm (Fig. 2-2b). The extinction of light at red and infrared regime results from the absorption and scattering by Ag nanoshells. Its dependence on the size clearly indicates that the wavelength of the coupled plasmon mode in core-shell particles can be controlled by simply changing the size of the core. An increase in the extinction in the longer wavelength is the unique plasmonic behavior of the core-shell particles, which is explained by a hybridization model.

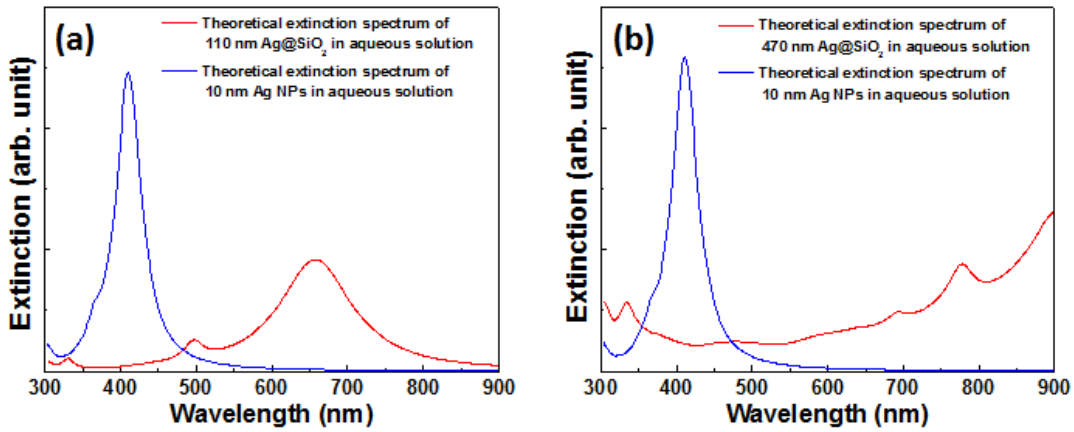

Figure 2-2. UV-vis extinction spectra of theoretical data calculated by Mie scattering approach. (a) 110 nm $Ag@SiO_2$ core-shell particles in aqueous solution. (b) 470 nm $Ag@SiO_2$ core-shell particles in aqueous solution

Simulated light absorption and scattering properties of the Ag nanoparticles and core-shell particles, which are dispersed in TiO_2 matrix, are shown in Figure 2-3. Since the refractive index of TiO_2 (n=2.37) surrounding the core-shell particles is larger than water, the peaks of the spectra shift to longer wavelength. It indicates that although the strength of absorption peak for core-shell particles is a little weaker than that of Ag nanoparticles, the scattering efficiency is much higher for core-shell particles.

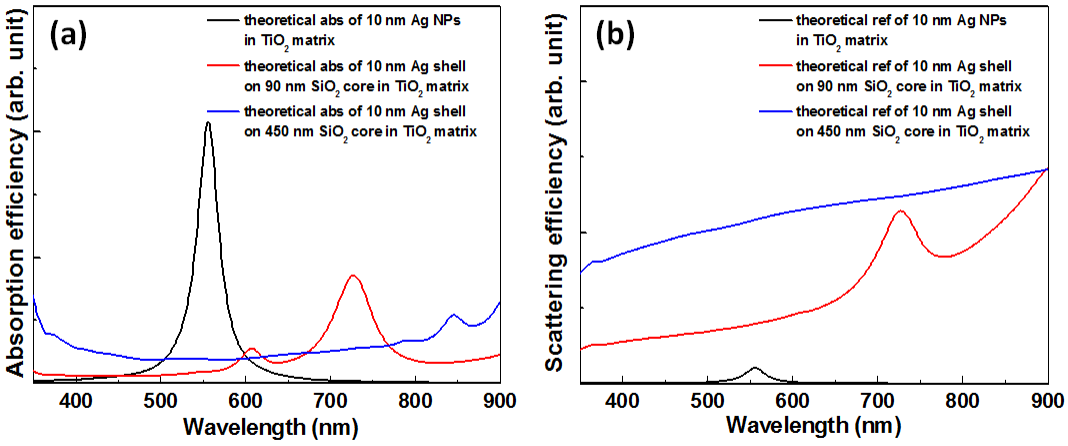

Figure 2-3. Theoretically calculated (a) UV-vis absorption efficiency and (b) reflection efficiency of Ag NPs with a diameter of 10 nm in TiO_2 matrix, 10 nm thick Ag shell of 110 nm Ag@SiO_2 in TiO_2 matrix, and 10 nm thick Ag shell of 470 nm Ag@SiO_2 in TiO_2 matrix

3.0 SURFACE-PLASMON ASSISTED ENERGY CONVERSION IN DSSC

3.1 BACKGROUND

3.1.1 Motivation

While DSSCs have several advantages that potentially offer an alternative to currently dominant Si-based photovoltaics, there are still problems that need to be solved to make DSSCs as efficient as other semiconductor-based photovoltaics. In particular, a single type of a dye material used in DSSCs cannot absorb a full range of the solar spectrum due to the mismatch between the solar spectrum and the light absorption spectrum of dyes.[97-99] Currently, the dyes of DSSCs absorb only part of the solar spectrum and the LHE of DSSCs is not uniformly high even in the visible range of the solar spectrum.

To address this issue, we incorporate plasmonic nanostructures in DSSCs to control the passage of photons. When both the energy and momentum of the incident light match those of the plasmons, the incident light can be coupled to the plasmons. This coupling amplifies local field intensity in the vicinity of nanostructures and enhances absorption and scattering cross-sections.[100] Recently, localized plasmons have attracted considerable attention as a promising tool that can enhance the energy conversion efficiency of PVs. Nakayama et al., demonstrated that high aspect-ratio Ag nanoparticles grown on the surface of optically thin GaAs solar cells

scattered the incident light and increased the short circuit current density of GaAs solar cells by 8 %.[101] The effect of the surface plasmons on enhanced light absorption was also proved in organic photovoltaics. Morfa et al., added a Ag nanoparticles layer into a photoactive layer in the herterojunction photovoltaics.[102] An improvement factor of 1.7 was achieved by increasing the optical absorption and output current at long wavelengths. Similarly, Kim et al., have systematically investigated the enhanced absorption of the organic layer due to the presence of Ag nanoparticles.[103] By incorporating plasmonic Ag nanoparticles on the surface of the ITO electrodes, the overall energy conversion efficiency of the organic photovoltaics was increased from 3.05% to 3.69%. The increase in the energy conversion efficiency is traced to surface plasmon coupled light absorption, which can increase the optical cross section of the thin organic layer. The surface plasmon effect of metal nanoparticles has been also studied in DSSCs. When flat TiO_2 films were sensitized by a combination of dye molecules and arrays of nanofabricated elliptical gold disks, the charge carrier generation rate of the dyes increased. Standridge, *et al*, used atomic layer deposition (ALD) to conformably coat arrays of silver nanoparticles with a very thin layer of TiO_2 and demonstrated plasmon enhanced photocurrent.[104] In addition, Ag nanoparticles were added to TiO_2 films to increase the efficiency of DSSCs through plasmon resonance.[105, 106] In these studies, Ag nanoparticles were employed to increase the scattering of the TiO_2 films or form a photonic band gap with the TiO_2 films.

In this study, we explore the influence of dielectric core - metallic nanoshell particles on solar energy conversion in DSSCs. Because the optical resonances and the near electro-magnetic field response can be tuned by changing the dimension of the core and shell components, the dielectric core - metallic nanoshell particles have great potential for optoelectronic and biomedical applications. Here, the structure of the core-shell particles is designed to arouse the

coupling of the surface plasmons with visible light. This coupling is expected to increase the absorption and scattering of the light in the photoelectrodes, which contributes to enhancing the energy conversion efficiency of the DSSCs. The new core-shell particles were distributed in TiO_2 films so that the entire photoelectrode was uniformly exposed to the plasmonic effect of the core-shell particles. The advantage of particulate nanostructures is that they excite localized surface plasmons regardless of the incidence geometry and polarization states of incoming light. In newly designed DSSCs, we systematically explore the role of localized surface plasmons on the light absorption, scattering, and energy conversion efficiency using spectroscopic and electrochemical characterization techniques.

3.1.2 Electron Lifetime Measurement

It is important to measure the photogenerated electron lifetime in the solar cell, since the electron-transfer kinetics play a main role in determining the conversion efficiency of the device. So far, two methods have been mainly used in electron lifetime characterization, including open circuit voltage decay (OCVD)[107, 108] and stepped light-induced transient measurements of photocurrent and photovoltage (SLIM-PCV).[109, 110]

OCVD is a powerful and simple tool to measure the electron lifetime of the DSSCs as a function of the photovoltage (V_{oc}). This method consists of turning off the illumination in a steady state and monitoring the subsequent photovoltage decay.[108] It provides a continuous reading of the lifetime change against the V_{oc}, and the data treatment based on the carrier recombination mechanisms is quite simple. Figure 3-1 shows the measurement setup. Monichromatic laser beam with an instant turning off at a steady state is generated from a laser diode (λ=660 nm) which is controlled by a function generator (Agilent 33220A). A voltage

decay from the steady state is monitored by a digital storage oscilloscope (Tektronix, TDS2024B) that is synchronized with the function generator.

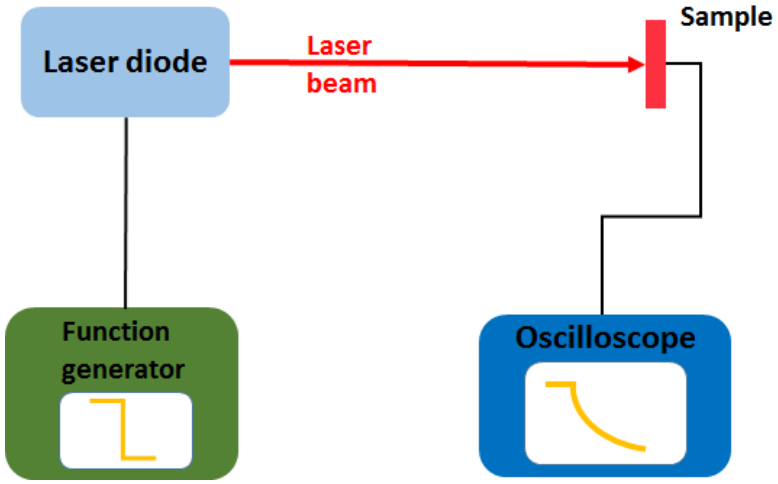

Figure 3-1. Setup of OCVD measurement

The electron lifetime is theoretically derived from a general recombination rate, which involves a higher reaction order electron transportation mediated by internal trapping and de-trapping processes. For a common nonlinear case, the electron lifetime is given by the reciprocal of the derivative of the decay curve normalized by the thermal voltage[107]:

$$\tau_n = -\frac{k_B T}{e}\left(\frac{dV_{OC}}{dt}\right)^{-1} \quad (3\text{-}1)$$

Typical results shown in Figure 3-2 consist of OCVD decay curves at different light intensities and relevant electron lifetime values obtained from eq. 3-1 as a function of V_{oc}.

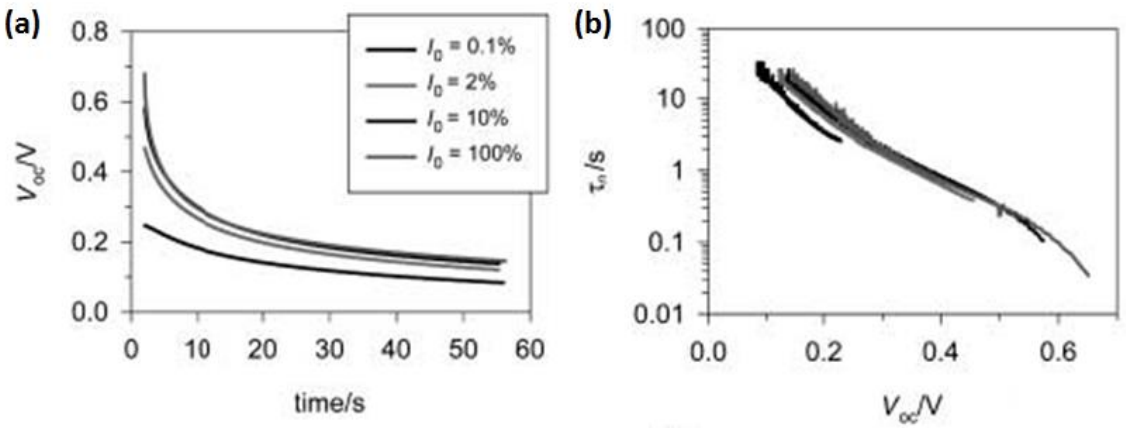

Figure 3-2. (a) Experimental V_{oc} decay at different light intensities. (b) The electron lifetime derived from eq. 3-1 as a function of V_{oc} [107]

SLIM-PCV can simplify the optical setup and reduce the measurement time in comparison to conventional time-of-flight and frequency-modulated measurement. It is a perturbation measurement applying a stepwise change in light intensity and monitor the change of photocurrent and voltage under this perturbation.[109] Both electron diffusion coefficient and lifetime can be obtained from the SLIM-PCV measurement. The experimental setup is shown in Figure 3-3. Monochromatic laser beam with a step change of intensity was generated from the laser diode (λ=660 nm) which is controlled by the function generator. A set of neutral density (ND) filter was used to change the laser intensity and placed in front of the sample. Voltage transient was monitored by the oscilloscope that is synchronized with the function generator. And current transient was obtained from the oscilloscope through a current amplifier (KEITHLEY 428), which can convert current signal into voltage signal.

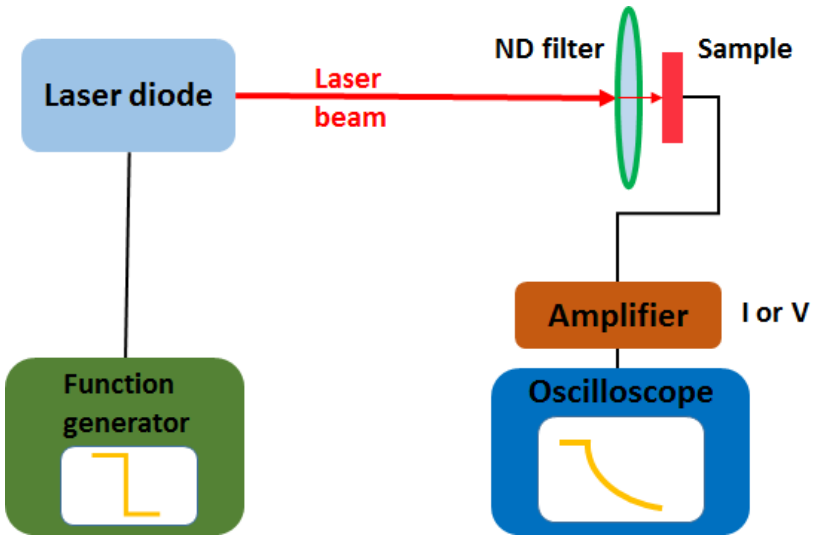

Figure 3-3. Configuration of SLIM-PCV measurement

At a short circuit condition of the DSSCs, initial light intensity, which corresponds to the short circuit current (J_{sc}), drops to a constant value instantly. This sudden reduction of partial light intensity induces the current transient. The time to reach the constant current value depends on the electron diffusion coefficient, which can be expressed as

$$D = L^2/(2.77\tau_C) \tag{3-2}$$

where L is the thickness of the electrode, and τ_C is the exponential decay time constant.[109]

The electron lifetime is measured from the photovoltage response of the DSSCs against the perturbation of light intensity at the open circuit condition. The electron density has the following relation

$$n(t) = Aexp(-t/\tau) \tag{3-3}$$

where A is Δn, the difference of electron densities before and after the light intensity change.[109] Under the small perturbation of light intensity, V_{oc} should be proportional to eq 3-3. Thus, the carrier lifetime can be derived from fitting of the relaxation time of the open circuit

voltage decay. Typical current responses and open circuit voltage transients as a function of time are shown in Figure 3-4.

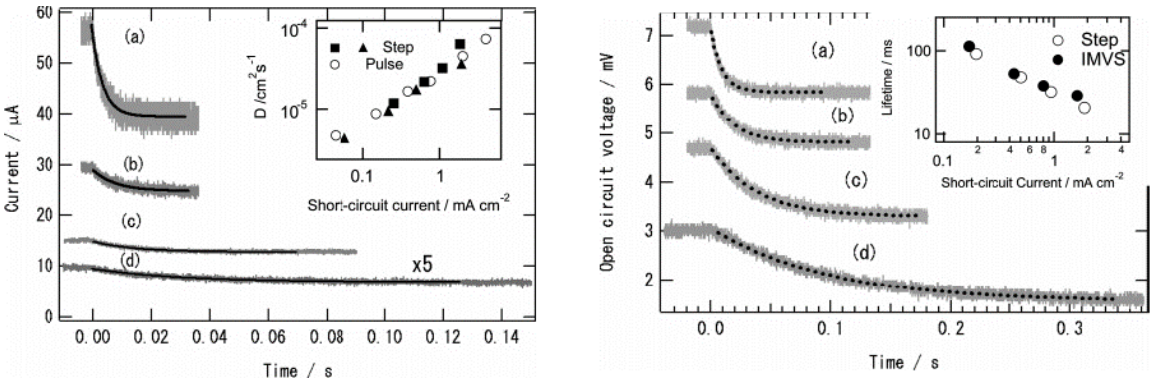

Figure 3-4. (left) Current responses and (right) voltage transients induced by different stepped laser intensities [109]

3.1.3 Electrochemical Impedance Spectroscopy

Electrochemical impedance spectroscopy (EIS) is a steady state method in measuring the current response to the applied ac voltage as a function of the frequency.[111] The parameters obtained in EIS are differential resistance and differential capacitance, which are strongly related to the frequency. The complex impedance Z(ω) is measured by scanning the frequency (f=ω/2π) at multitude of values over several decades, typically from mHz to 10 MHz, and is defined as

$$Z(\omega) = \frac{\hat{V}(\omega)}{\hat{I}(\omega)} \tag{3-4}$$

where ω is a certain angular frequency, $\hat{I}(\omega)$ an ac electrical current and $\hat{V}(\omega)$ a certain ac voltage applied to the system.[112] In the frequency domain, capacitance can be deduced via a simple conversion from impedance:

$$C^*(\omega) = \frac{\hat{I}(\omega)}{i\omega\hat{V}(\omega)} = \frac{1}{i\omega Z(\omega)} \tag{3-5}$$

An important example of an equivalent circuit is the RC parallel combination with addition of a series resistance (Figure 3-5a). The impedance is described as:

$$Z(\omega) = R_2 + \frac{R_1}{1+i\omega\tau_1} \tag{3-6}$$

The complex impedance plot, which also known as Nyquist plot, is shown in Figure 3-5b. It indicates that the parallel *RC* forms an arc in the complex plane which shifts positively along the real impedance axis by a series resistance R_2. As the parallel resistance decreases, the arc shrinks. The plot shown in Figure 3-5c, also termed as Bode phase plot, expresses the frequency response phase shift. The peak of the phase angle moves to lower frequencies as τ_1 decreases.

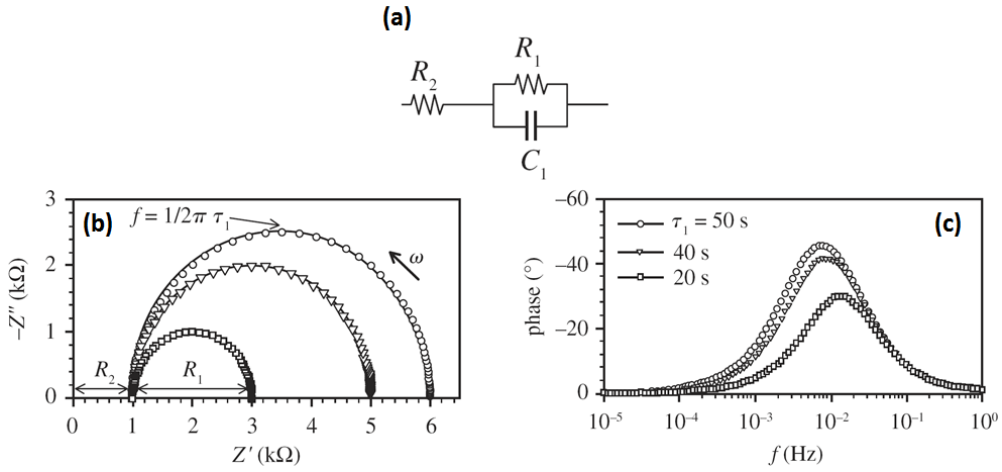

Figure 3-5. Representations of the impedance of an equivalent circuit. R_1 takes on values 5, 4, 2 kΩ, C_1 = 10mF, τ_1 = 50, 40, 20 s, R_2 = 1 kΩ. (a) The equivalent circuit, (b) Nyquist plot and (c) Bode plot[112]

When employing EIS to study the photoelectrochemical process in the DSSCs, typically three semicircles is found in the Nyquist plot or three characteristic frequency peaks in a Bode phase plot (Figure 3-6c,d). These three semicircles are attributed to the Nernst diffusion within the electrolyte, the electron transfer at the oxide/electrolyte interface and the redox reaction at the

Pt counter electrode in the order of increasing frequency.[111] The equivalent circuit of the DSSC is shown in Figure 3-6a,b, in which two conditions are considered and distinguished by the impedance response at the TiO_2/electrolyte interface, *Z*. This impedance is proportional to the square root of the production of R_d and R_r, which correspond to diffusion and dark reaction impedance, respectively. In the condition of $R_r \gg R_d$, simple diffusion process happens within the restricted boundaries. And the equivalent circuit for the mesoporous TiO_2 film contains an impedance element, comprising series connected diffusion element Z_{w1} and charge-transfer element R_{REC}, in parallel with a capacitive (constant phase angle) element CPE3. In the other case of $R_d \gg R_r$, when only partial of the photogenerated charge carriers are collected, a major part of the electron reacts with the triiodine (I_3^-) in the electrolyte, leading to a single Gerischer impedance, Z_G. In addition, R_{FTO/TiO_2} is the resistance at the FTO/TiO_2 contact and CPE1 is the capacitance of this interface. Z_{W2} stands for the Warburg impedance describing I_3^- diffusion in the electrolyte. CPE2 means a double layer capacitance at the electrolyte/Pt/FTO interface, and R_{CE} corresponds to the charge transfer impedance at the counter electrode.[111]

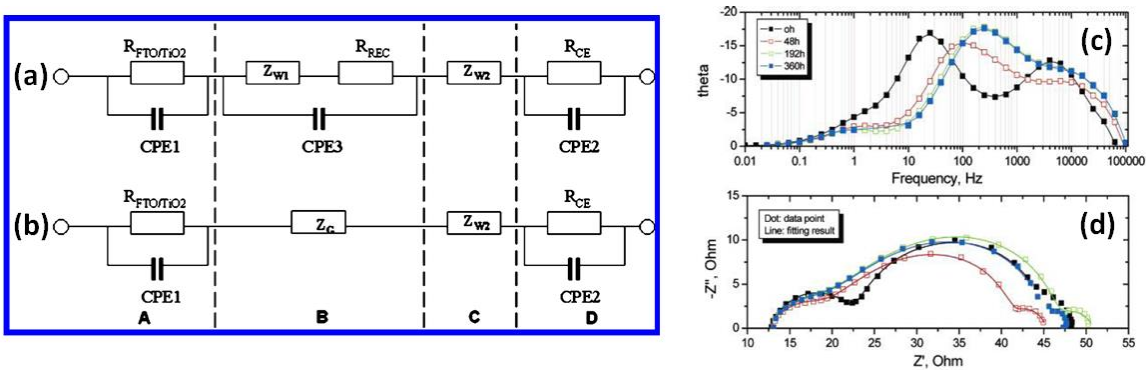

Figure 3-6. Equivalent circuits of DSSC, including (a) quantitative collection of photoinjected electron and (b) incomplete electron collection. (c) Bode plot and (d) Nyquist plot of DSSC using N719 dye [111]

3.2 PERFORMANCE ENHANCEMENT BY CORE-SHELL PARTICLES[113]

3.2.1 Sample Preparation and Characterization

Synthesis of SiO_2 spheres and SiO_2 core - Ag shell composites. The uniform SiO_2 spheres were prepared via Stöber method.[114] Ammonium hydroxide (J. K. Baker, 28%) and tetra ethoxy silane (TEOS, Sigma-Aldrich, 98%) were used as raw materials. The average diameter of silica particles was controlled to be 400 nm.

The SiO_2 core – Ag shell composites were synthesized by a seed mediated two-step method (Figure 3-7). Ag nanoparticles were first formed on the surface of SiO_2 particles, which was followed by the subsequent deposition of the Ag thin layer. Ag nanoshell seeds were synthesized by modifying the sonochemical reaction.[81] Silica particles were added into deionized water. Then, silver nitrate (Sigma-Aldrich, 99.8%) was dissolved in ammonium hydroxide solution that was subsequently poured into the aqueous slurry of the SiO_2 particles. After Ag source and SiO_2 particles were mixed, the slurry was sonicated for 3 hrs by using the high-intensity ultrasound radiation. During the sonochemical reaction, temperature of the slurry was maintained at 20 ^oC. Resulting particles were centrifuged and washed to remove residual reagents. Purified particles were heated at a temperature of 100 ^oC under nitrogen gas flow for 3 hrs to crystallize silver nanoparticles on the surface of SiO_2 particles. After thermal annealing, the particles turned to be dark brown, indicating that Ag nanoparticles were nucleated on the surface of the SiO_2 particles.

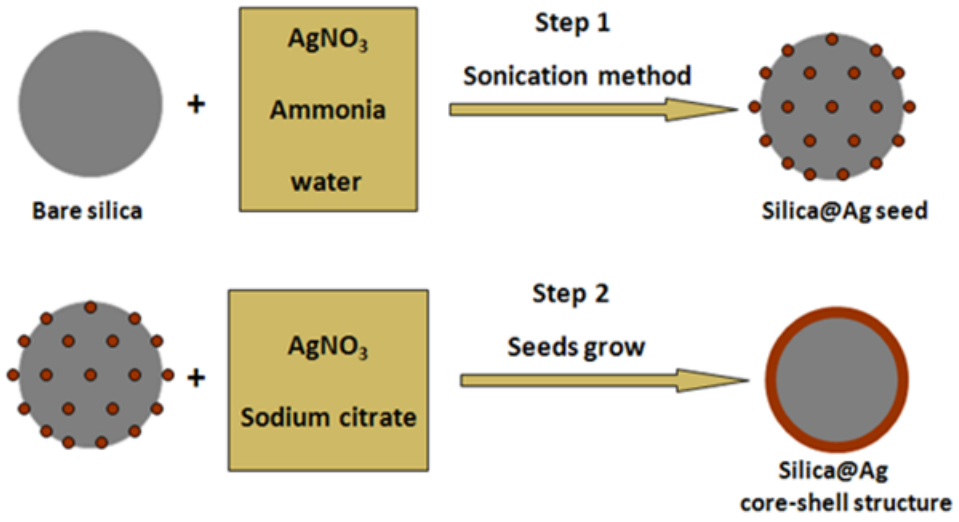

Figure 3-7. Schematic procedure of preparation Ag@SiO_2 core-shell particles by a seed mediated two-step method

These Ag nanoparticles were used as seeds to grow the thin silver layer in the next reaction step. Dark brown powder (Ag seeds - SiO_2 core), silver nitrate, and deionized water were sequentially added into a 250 ml three-neck bottle and mixed well. At 85 ^oC, sodium citrate was added into the aqueous mixture and was maintained at 85 ^oC for 1 - 3 hrs under vigorous stirring. After the second reaction was finished, the SiO_2 core – Ag shell composite particles were obtained.

Preparation and characterization of TiO_2 nanoparticle - composite mixture films. Anatase TiO_2 nanoparticles were prepared using a hydrothermal reaction.[115] A mixture of titanium (IV) isopropoxide (TTIP, Sigma-Aldrich, 97 %) and 2-propanol (J. K. Baker) was slowly dripped into a mixture of acetic acid (Glacial, J. K. Baker) and deionized water at 0 ^oC. Then, the solution was preheated at 80 ^oC for 8 hrs and was reacted at 220 ^oC for 6 hrs in a microwave accelerated reaction system (MARS, CEM Co.). The phase of TiO_2 nanoparticles is anatase and the other phases (rutile and brookite) are not found in XRD patterns. A

microstructure of the hydrothermally grown nanoparticles is shown in a TEM micrograph of Figure 3-8.

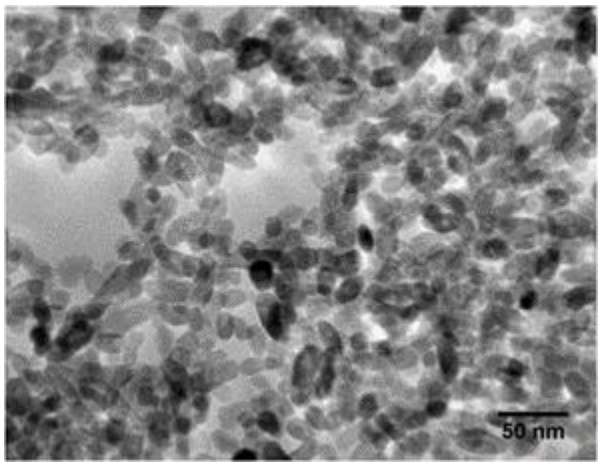

Figure 3-8. TEM image of TiO_2 nanoparticles that are prepared by a hydrothermal route

Pure TiO_2 nanoparticle films and TiO_2 – composite mixture films were fabricated by a recently reported chemical sintering method.[116] A mixture of TiO_2 slurry and core-shell composite slurry were added with a small amount of ammonium hydroxide to increase the viscosity of the mixed slurry. As a reference sample, a viscous paste of TiO_2 nanoparticle - uncoated SiO_2 particle mixture was also prepared using a same method. The paste was spreaded on a transparent conducting glass substrate (FTO) by the doctor-blade technique and annealed at 400 ^oC for 2 hrs under the flow of nitrogen gas.

The microstructure of the core-shell composite particles and the mixture films was examined using scanning electron microscopy (SEM) (Model Philips XL 30) and transmission electron microscopy (TEM) (Model JEM-200 CX, JEOL). The crystal structure of the core-shell composite particles was determined using an X-ray diffractometer (XRD) (Model Philips Analytical X-Ray). Absorption, transmission, and scattering of the core-shell particles and

mixture films were analyzed by UV/Vis spectrometer (Perkin Elmer, Lambda 35 UV/vis Spectrometer) attached with an integrating sphere in the range from 300 nm to 900 nm.

Fabrication of DSSCs and characterization of their photovoltaic properties. The TiO_2 mixture films were sensitized in the solution of N719 dye [ruthenium (2,2'-bipyridy-4, 4'-dicarboxylate)$_2$(NCS)$_2$, Solaronix SA, dissolved in ethanol] at room temperature for 24 hrs, and then sandwiched with thermally platinized FTO counter electrode. Two substrates were separated by 25 μm thick hot melt sealing tape (SX-1170-25, Solaronix SA) and the internal space of the cell was filled with liquid electrolyte (Iodolyte AN-50, Solaronix SA) (Figure 3-9).

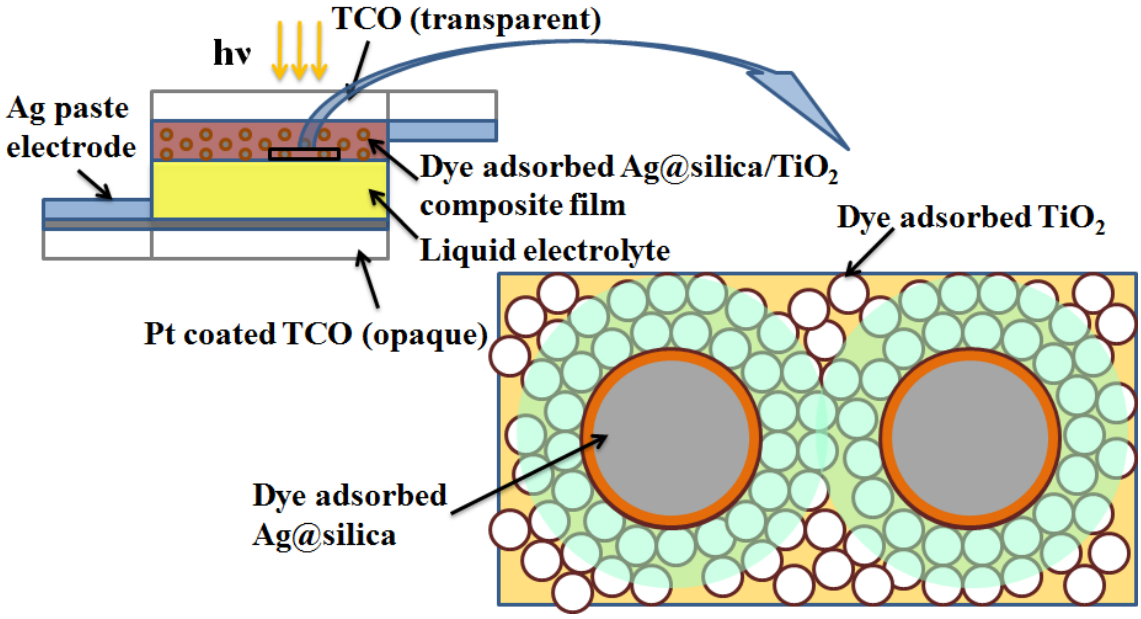

Figure 3-9. Schematic structure of the device which contains the core-shell particles embedded composite film

A part of sensitized thick films were immersed in NaOH solution to desorb the dyes. The amounts of dyes desorbed from different photoelectrodes were examined by measuring UV/Vis absorption spectra. The photovoltaic properties of the DSSCs were tested under AM 1.5 G simulated sunlight (PV Measurements, Inc) with the aid of the electrochemical workstation (CHI 660 C). Incident photon to current efficiency curves (IPCE) of DSSCs was also measured by

illuminating the sample with a monochromatic beam in the visible range. IPCE was calculated by IPCE (λ) = 1240 ($J_{SC}/\lambda\varphi$) where λ is the wavelength of the incident beam, J_{sc} is short-circuit current density, and φ is the incident radiative flux which was measured by using a silicon reference photodiode.

3.2.2 Results and Discussions

Transmission electron micrographs in Figure 3-10 present the evolution of Ag nanoshells with increasing Ag deposition time. In Figure 3-10b, Ag nanoparticles with a diameter of 5 - 6 nm were found on the surface of silica particles, which confirms the formation of the nucleation seeds for Ag nanoshells. After the first step of the Ag layer coating process, Ag nanoparticles were formed on the surface of the silica particles. These nanoparticles induced the growth of Ag films in the second step of the Ag layer coating process. As the deposition of the Ag nanolayer continued in the second step, the surface of the core-shell particles became rough. After the Ag layer was deposited for 1 hr, continuous polycrystalline films consisting of small Ag nanoparticles were formed on the surface of the silica cores and the surface of the silica particles were uniformly coated with the Ag nanoshell. As the deposition reaction was prolonged, the size of the grains and the surface roughness in the polycrystalline Ag layer increased (refer to Figures 3-10c and 3-10d). The corresponding scanning electron micrographs (SEM) are shown in Figure 3-11.

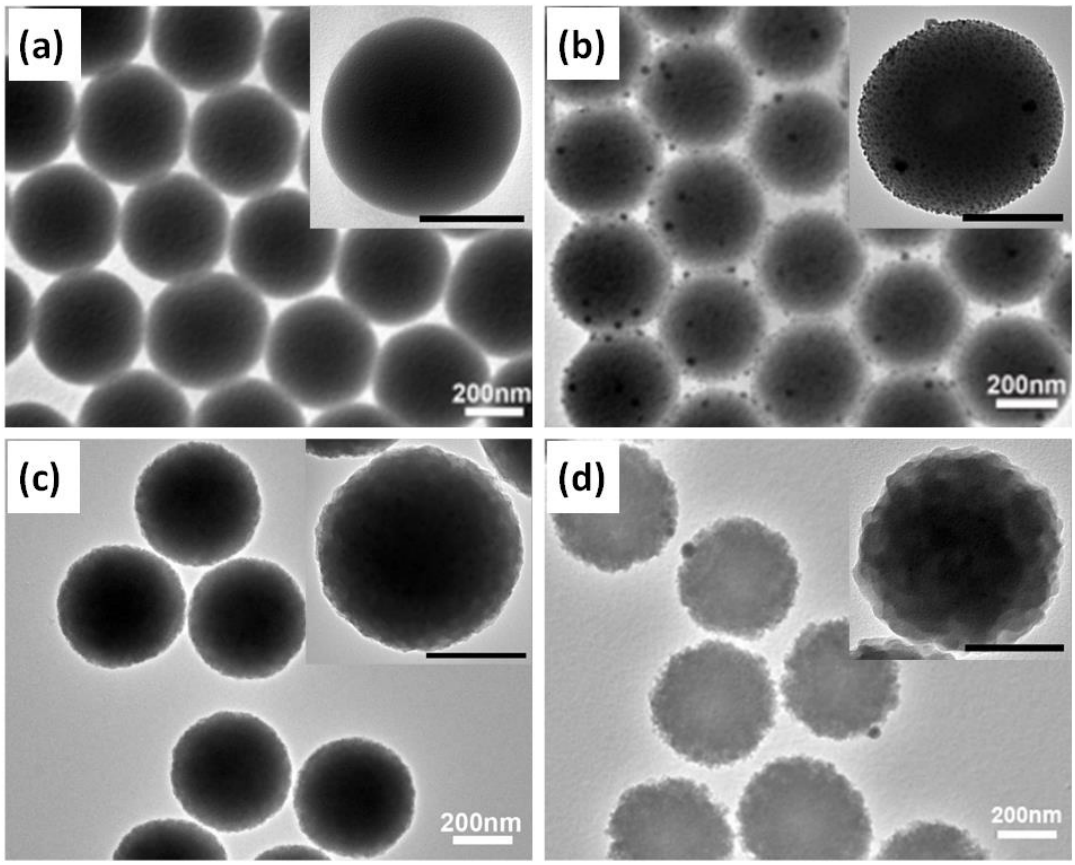

Figure 3-10. TEM micrographs of (a) bare silica spheres, (b) silica particles coated with Ag seeds, (c) two-step grown silica@Ag core-shell particles with the Ag layer being deposited for 1 hr, and (d) two-step grown silica@Ag core-shell particles with the Ag layer being deposited for 3 hrs (black scale bar in insets = 200 nm)

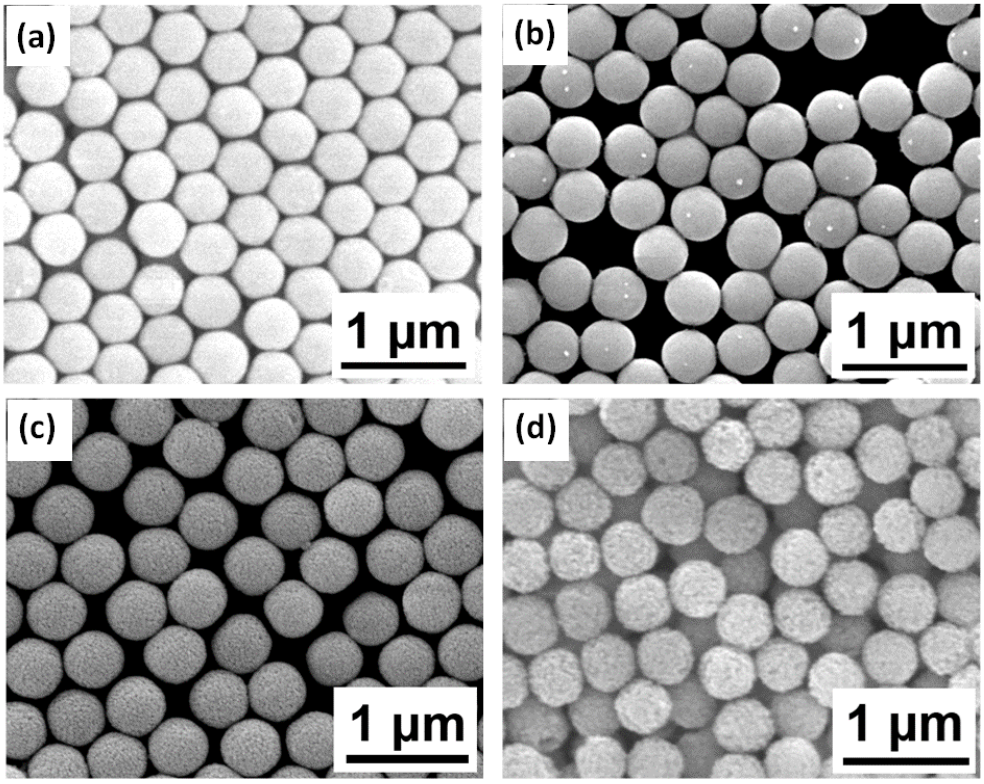

Figure 3-11. SEM micrographs of (a) bare silica spheres, (b) silica particles coated with Ag seeds, (c) two-step grown silica@Ag core-shell particles with the Ag layer being deposited for 1 hr, and (d) two-step grown silica@Ag core-shell particles with the Ag layer being deposited for 3 hrs

X-ray diffraction (XRD) patterns of bare silica particles and core-shell particles are shown in Figure 3-12. Based on the JCPDS card, diffraction peak (Figure 3-12a) that locate at 38.12^{o}, 44.23 ^{o}, 64.43 ^{o} and 77.47 ^{o} correspond to the (111), (200), (220) and (311) planes of silver separately. And no diffraction peak of silver oxide has been detected in the XRD spectra. This indicates that the Ag nanoshell of the core-shell particles can endure the thermal treatment which is essential in fabricating photoanodes of DSSCs. UV/Vis absorption spectra of core-shell particles in Figure 3-13 exhibit an absorption peak in the blue range when the core-shell particles are dispersed in de-ionized water. As the thickness of Ag nanolayer increases, the core-shell

particles absorb more light due to the evolution of the surface plasmons which are centered at 410 nm.

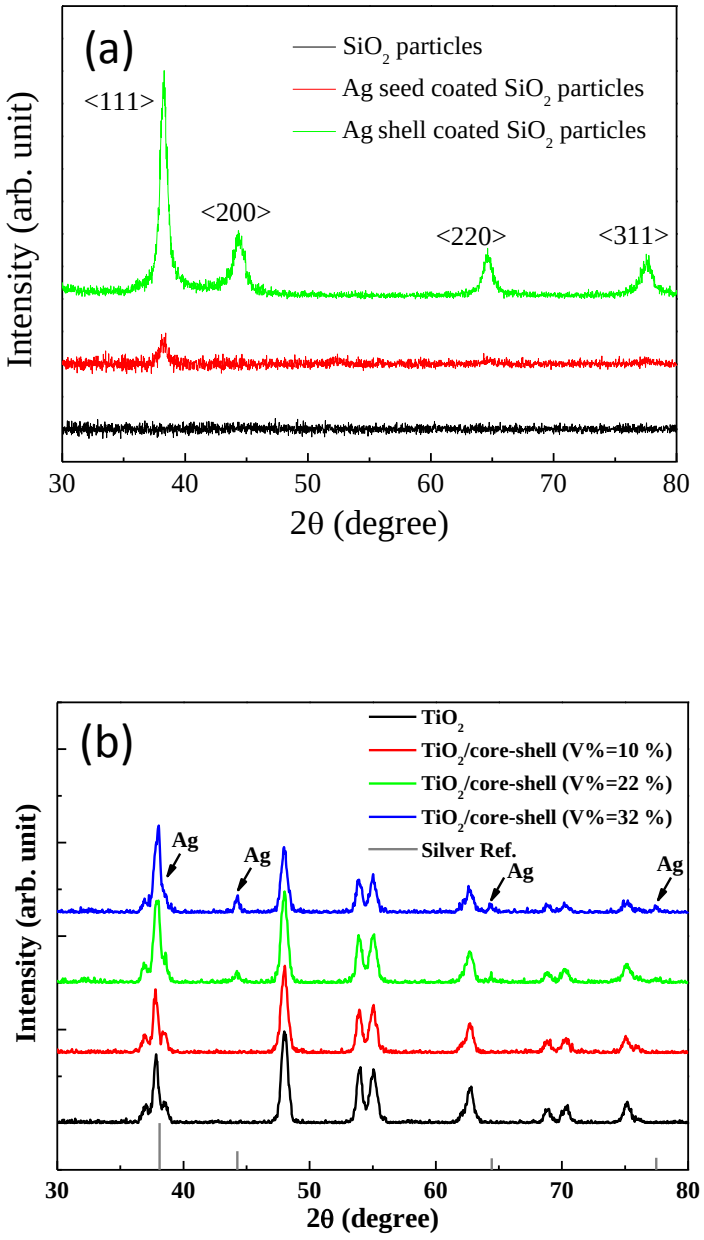

Figure 3-12. XRD patterns of (a) bare silica, silica particles coated with Ag seeds, and silica particles deposited with Ag layer for 1 hr, and (b) TiO_2 nanoparticle and silica@Ag core-shell particle mixture films that are annealed in N_2 atmosphere at 400 ^oC for 1 hr

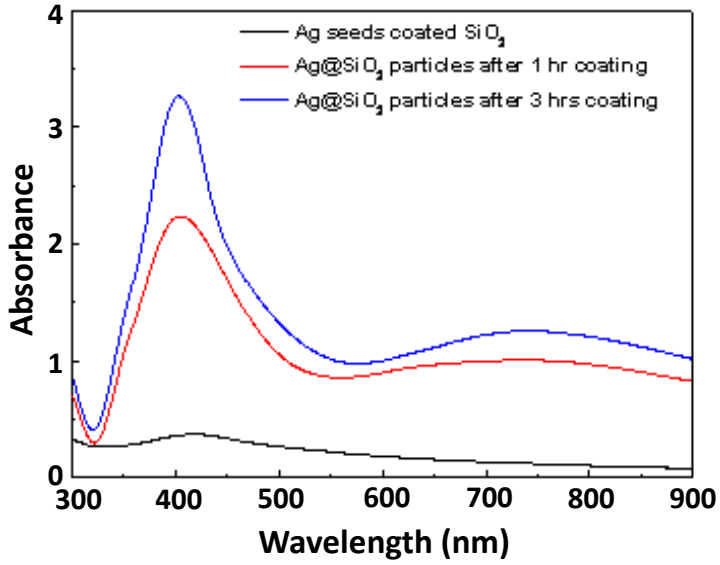

Figure 3-13. UV/Vis absorption curves of silica particles coated with Ag seeds and SiO_2 core – Ag shell particles with Ag layer being coated for 1 and 3 hrs

Structural and optical analyses of the core-shell particles show that 1 hr deposition provides a uniform, smooth, and highly-crystalline Ag layer that can absorb enough light to excite the surface plasmons. Therefore, 1 hr reaction was selected as the coating time of Ag shells onto SiO_2 cores in examining the effect of the surface plasmons on the light absorption and photon-electron conversion of DSSCs. The 1 hr reacted core-shell particles were mixed with TiO_2 nanoparticles and chemically agglomerated to yield several μm thick composite films. Figure 3-14 shows SEM micrographs of the composite films in both plane-view and cross-section. Large particles in the micrographs are core-shell particles that are uniformly dispersed within the composite films. The distance between core-shell particles decreases as the volume fraction of core-shell particles increases. For 22 vol% core-shell particles the mean distance between the surfaces of core-shell particles was about 300 nm. To confirm the uniform

distribution of core-shell particles in the composite films, the expected interparticle distance of the core-shell particles in the composite films was calculated and the results of this geometric calculation were compared with the SEM analysis. The expected distance between the outer surfaces of the core-shell particles is about 470 nm for the films containing 10 vol% core-shell particles, 260 nm for the films containing 22 vol% core-shell particles, and 170 nm for the films containing 32 vol% core-shell particles. These calculated values agree quantitatively with experiment.

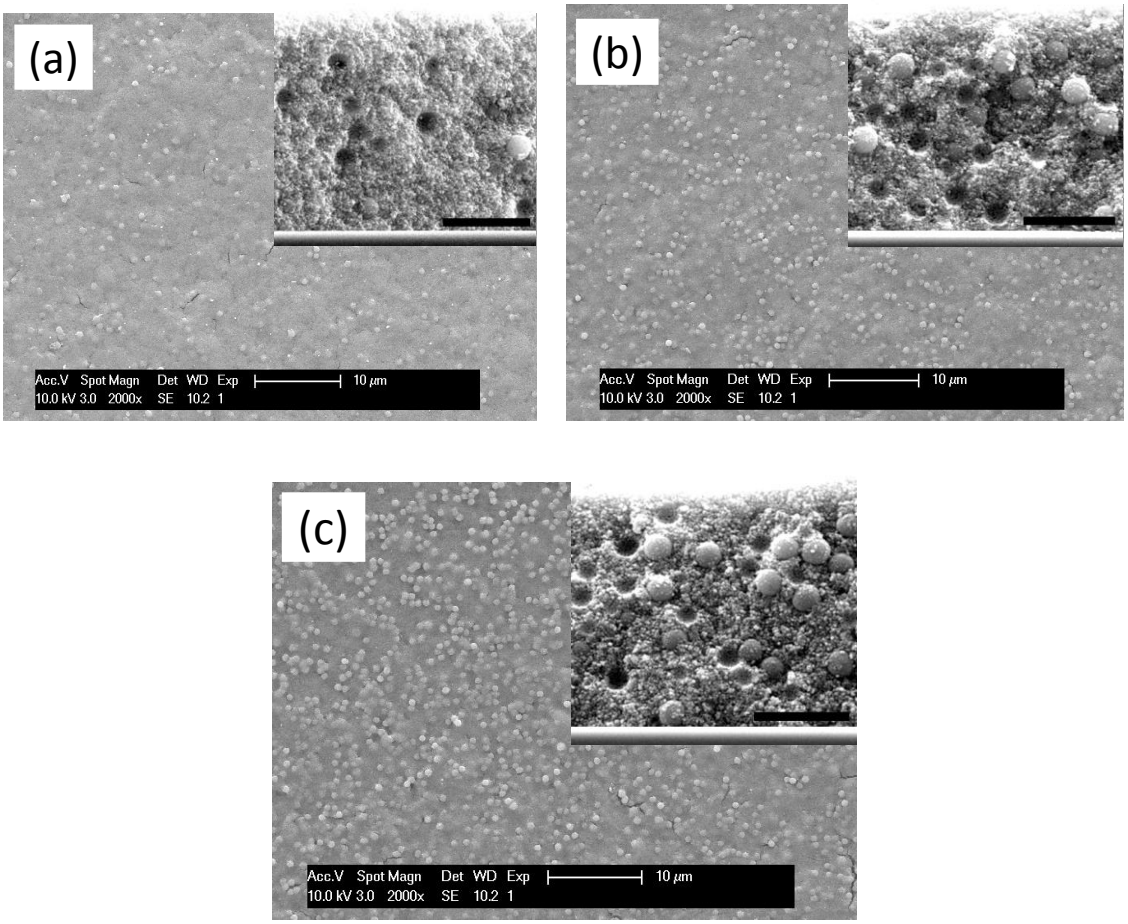

Figure 3-14. Plane-view and cross-section mode (insets) scanning electron micrographs of TiO_2 nanoparticle – core-shell particle mixture films containing: (a) 10 vol% of the core-shell particles, (b) 22 vol% of the core-shell particles, and (c) 32 vol% of the core-shell particles (black scale bar in insets = 2 μm)

UV/Vis absorption spectra of 5 μm thick composite films are presented in Figure 3-15a. For the precise measurement of thick films, UV/Vis spectroscopy analysis was performed in air using an integrating sphere. Since there is a tradeoff between the plasmonic effect and the decreased surface area in the core-shell particle added TiO_2 film, the change in the optical properties of the composite films with different core-shell loadings was systematically investigated. A composite film of bare SiO_2 particles and TiO_2 nanoparticles was also prepared as a control sample to qualitatively separate the surface plasmonic effect of the Ag shell from the geometrical scattering effect of SiO_2 cores. When the content of core-shell particles reaches 22 vol%, the mixed films show a dramatic increase in the absorption spectrum in visible range with the appearance of a broad peak ranging from 450 nm to 700 nm. Compared with the absorption spectra of core-shell particles dispersed in water, the absorption peak of the composite films exhibits red-shift to 550 nm, which is due to the change in the refractive index of the medium surrounding the core-shell particles. Since the porosity of the mixture films is larger than 50%, the space near the core-shell particles is occupied by anatase TiO_2 and air. Given that the refractive index is ~2.49 in anatase TiO_2, ~1.33 in water and ~1 in air, the refractive index of the composite films increases and the absorption of the peak moves to longer wavelength. This broad absorption peak is also observed in the transmittance spectra of core-shell particle added TiO_2 films in Figure 3-15b. In a bare SiO_2 particle added composite film, the decrease in the transmittance is less than that of the film containing the same amount of the core-shell particles and a specific peak is not found. In Figure 3-15c, the reflectance of the core-shell particle added mixture films is increased in the red range, which is not found in TiO_2 films and TiO_2-SiO_2 composite films. The increase in the reflectance of the core-shell particle added films is traced to the large scattering cross-section and multiple scattering of the core-shell particles.

In contrast to the core-shell particles, a bare SiO_2 particle added film exhibits a reflectance spectrum whose shape is very similar to the pure TiO_2 film. A difference in the level of absolute reflectance between these two films is attributed to the scattering of large SiO_2 particles in the visible range. This clearly indicates that the core-shell particles change the passage of the photons in the composite films and simple geometrical scattering of SiO_2 cores is not mainly responsible for the optical properties of the composite films. UV/Vis spectra shown in Figure 3-15 suggest that localized surface plasmons in the core-shell type composites increase the scattering and absorption of incoming light. A comparison of the experimental results with the theoretical calculations (Fig. 2-1) shows that the reflectance of TiO_2/core-shell mixture films is well explained when the Ag nanoshell is assumed to be a perfect film. Contradictory conclusions from the absorption and scattering efficiencies indicate that the Ag shells used in our study have characteristics of both particles and films and those two different mechanisms contribute to enhancing the optical field near the core-shell particles.

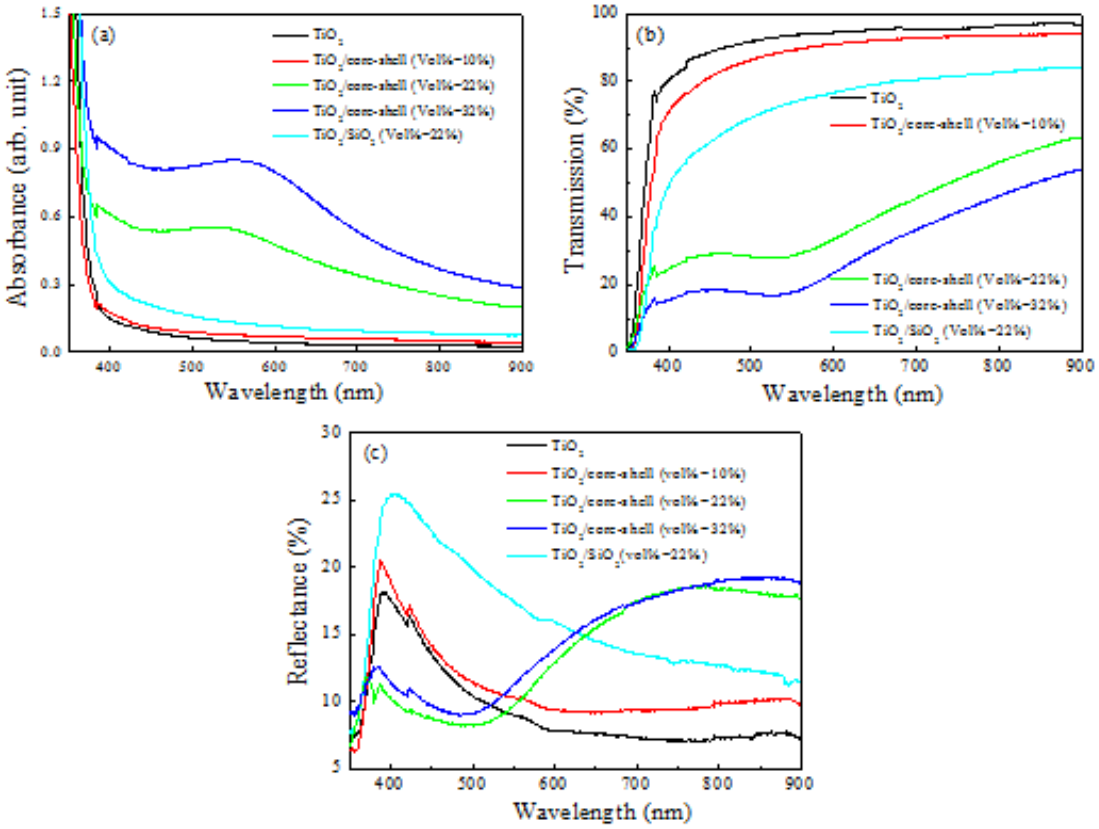

Figure 3-15. UV/Vis absorption spectra (a), transmittance spectra (b), and scattering spectra (c) of TiO_2 film and mixture films containing different amount of SiO_2 core – Ag shell particles (as a reference sample, a mixture of bare SiO_2 particles and TiO_2 nanoparticles was also tested); UV/Vis measurements are performed using an integrating sphere

The evanescent waves associated with surface plasmons generate strong field intensity in the near field. To examine the effect of the surface plasmons on the optical cross section of ruthenium dyes, the composite films were coated with N719 dyes and the absorption of dye adsorbed films was measured. Figure 3-16 shows the light absorption of dye coated TiO_2 and TiO_2/core-shell particle (22 vol%) films and their difference in air. In Figure 3-16, the difference curve between UV/Vis absorption spectra of TiO_2 and TiO_2/core-shell particle films exhibits two small humps with peaks of 480 nm and 610 nm, respectively. These features in the difference curve suggest that the core-shell particles help the dyes to absorb more photons, which is

pronounced in the regimes of blue light and red light. This can compensate well for the weakness of currently dominant polypyridyl ruthenium dyes whose optical cross-section is not uniform in the visible range. The role of the core-shell type particles is explained as follows. First, the plasmon excitation increases the optical density of incoming light near the surface of metal nanostructures. Therefore, if the dye materials coated on the TiO_2 nanoparticles are placed near the outer surface of core-shell particles, the dye materials within the near-field range are exposed to the light, which is intensified by the surface plasmons. This, in turn, causes the dye materials to harvest more photons. Second, the enhanced multiple scattering of the core-shell particles in the far-visible range will prevent transmission of incoming light and increase the chance for dye materials to convert the photons to the electronic carriers. In other words, more photons are trapped in the composite films for longer period due to the light scattering effect of the core-shell particles.

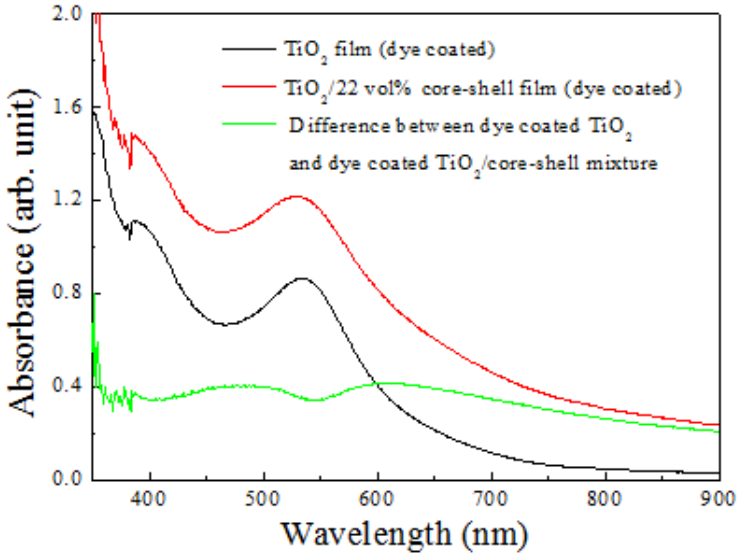

Figure 3-16. UV/Vis absorption spectra of dye coated TiO_2 and TiO_2/core-shell particle (22 vol%) films and their difference in air. UV/vis measurements are performed using an integrating sphere

Prior to photovoltaic performance characterization, we also examined the effect of core-shell particles on the dye adsorption and the stability of the Ag nanoshells in the electrolyte. After dyes were desorbed from pure TiO_2 films and composite films, their UV/Vis absorption spectra were measured (Figure 3-17). The amount of desorbed dye is about 33% larger in pure TiO_2 films than in mixture films. This difference in the dye adsorption is qualitatively explained by the decrease in the surface area in mixed films. When 22 vol% of 400 nm core-shell particles are added to 25 nm TiO_2 nanoparticles, the total surface area of the core-shell particles is only 0.7% of that of TiO_2 nanoparticles. Since the contribution of core-shell particles to the surface area of the mixture is negligible, 22 vol% core-shell particle added films have ~21 % less surface area than pure TiO_2 films. This, in turn, decreases the maximum amount of dye that can be adsorbed by ~21 %, which is qualitatively consistent with the UV/Vis absorption spectra in Figure 3-17.

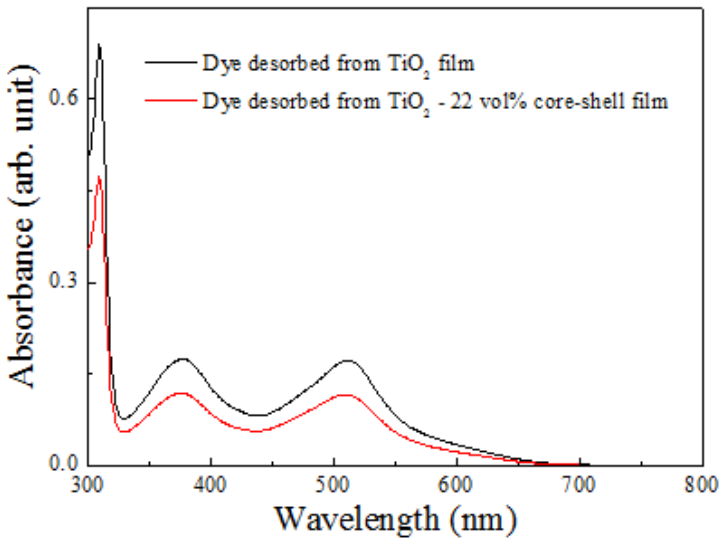

Figure 3-17. UV/Vis absorption spectra of dyes that are desorbed from TiO_2 film and the mixture films containing 22 vol% of core-shell particles

Since one of the important parameters in using the plasmonic particles in DSSCs is the chemical stability of the nanostructured metals in the electrolyte, the corrosion behavior of the silver coated-silica spheres was also examined. The results are presented in Figure 3-18. It was found that the corrosion of the silver layer is significantly prevented by N-719 dye. When the bare thick mixture film was immersed in the dye, the plasmonic absorption peak of the core-shell particles was easily reduced in the UV-Vis absorption. However, once the dye was coated on the surface of the Ag layer, the stability of the Ag layer in the electrolyte was significantly increased. This indicates that the iodide ions in the electrolyte exchange electrons with the dye rather than with the high crystalline Ag layer.

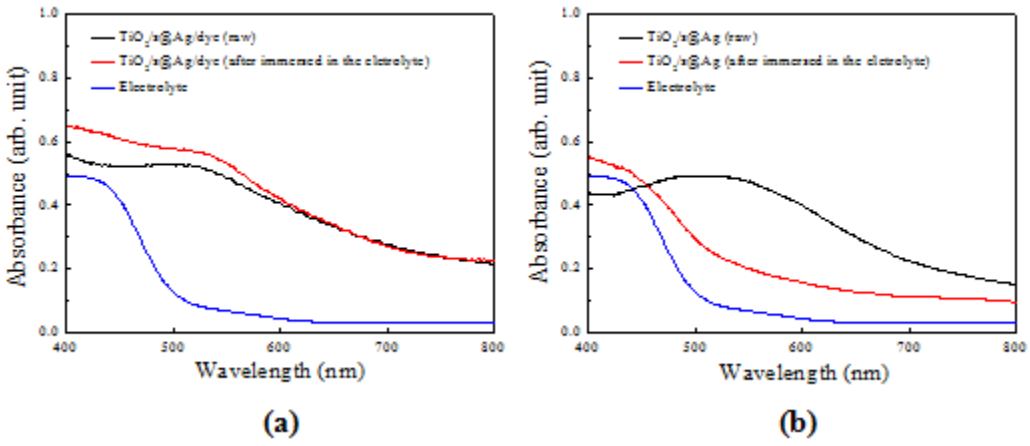

Figure 3-18. UV/Vis absorption spectra of (a) the dye coated TiO_2 - 22vol% core-shell composite film before and after being immersed in the electrolyte for 1 day, and (b) the bare TiO_2 - 22vol% core-shell composite film before and after being immersed in the electrolyte for 1 day

DSSCs were fabricated using N719 adsorbed films. Figure 3-19 shows *J-V* curves of DSSCs of simple TiO_2 films and composite films containing different amount of core-shell particles. The thickness of all films is 5 μm. The overall conversion efficiency of DSSC is improved when the core-shell particles are added. Compared with pure TiO_2 films, the mixed

films containing 22 vol% core-shell particles increase the efficiency from 2.7 % to 4.0 %. Given that 22% decrease in the surface area of the composite film reduces the amount of the adsorbed dye, this increase in the efficiency indicates that the well-arranged core-shell particles can enhance the energy conversion capability of the dye molecule in the near-field by up to 80%. The higher energy conversion efficiency of core-shell particle embedded DSSC is due to the increase in both short circuit current (J_{sc}) and open circuit voltage (V_{oc}). J_{sc} of DSSCs containing 22 vol% core-shell particles is 7.8 mA cm^{-2}, which is higher than the J_{sc} of pure TiO_2 film based DSSCs (5.9 mA cm^{-2}). The addition of core-shell particles also slightly increases V_{oc} from 0.63 V to 0.76 V. Given that the amount of dye adsorbed on TiO_2 films is 33% larger than the mixed films and the same TiO_2 nanoparticles are used in both films, this difference cannot be attributed to dye content or transport kinetics of electrons in the films. The energy conversion efficiency of DSSCs is moderately improved to 3.0 % and 3.4 % for core-shell particle fractions of 10 vol% and 32 vol%. The effect of the core-shell particles on J_{sc} is attributed to the combined effect of the increased light intensity and the decreased surface area (see next section for explanation). In addition, it is noted that DSSCs using 32 vol% core-shell particles possess higher open circuit voltage and slightly lower short circuit current than DSSCs using only TiO_2. This increase in V_{oc} may be attributed to the reduced recombination of photogenerated carriers, with the large core-shell particles impeding back-reaction with tri-iodide ions in the electrolyte.

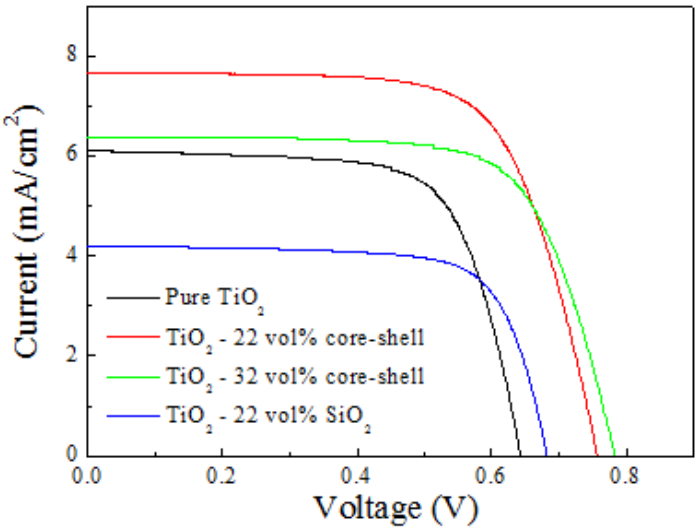

Figure 3-19. *J-V* curves of DSSCs using TiO_2 film or mixture films containing different amount of core shell particles, as photoanodes (as a reference sample, the TiO_2 - SiO_2 mixture film was also tested)

Figure 3-20 shows the lifetime of electrons in DSSCs using pure TiO_2 and TiO_2 – 22vol% core-shell particle composite films to examine the correlation between the core-shell particles and the retarded back electron transfer. The transient of V_{oc} was measured as a function of time by using a 633nm photodiode laser as the light source. Then, the carrier lifetime in different DSSCs were calculated from the decay curves of V_{oc} (inset of Figure 3-20).[107] The addition of the core-shell particles significantly increases the carrier lifetime, indicating the suppressed recombination of the photogenerated carriers and the backward transfer of electrons from the TiO_2 films to the electrolyte in the presence of the core-shell particles. Additional information on the backward electron transfer and carrier life time that is consistent with the transient of V_{oc}, are presented in Figure 3-21.

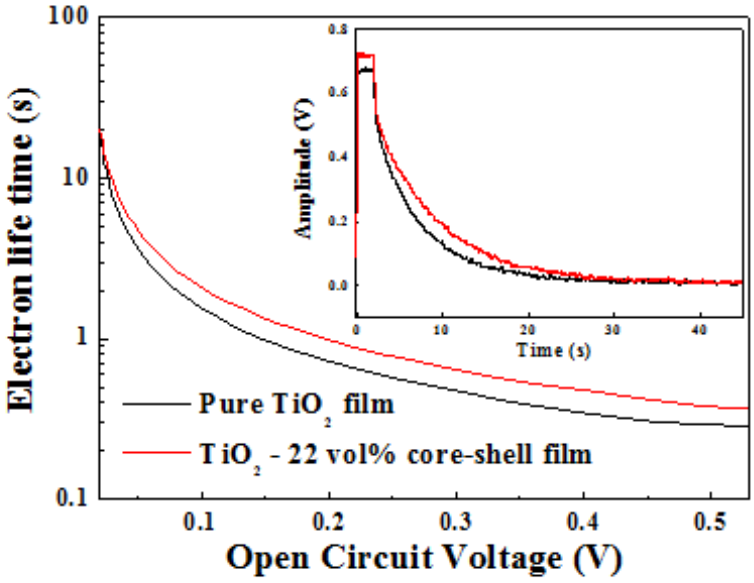

Figure 3-20. Electron life time for DSSCs using pure TiO_2 and TiO_2 – 22vol% core-shell particle composite films as a function of V_{oc} (The inset shows open circuit voltage decays for each solar cell)

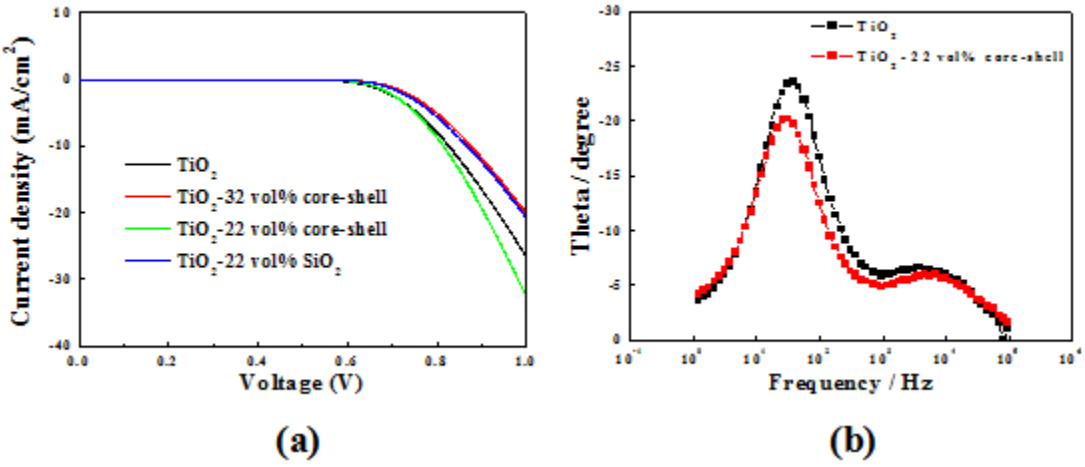

Figure 3-21. (a) Dark current curves, (b) Nyquist plots in DSSCs using TiO_2 film, TiO_2/core-shell composite film, and TiO_2/SiO_2 composite film as the photoelectrode

IPCE spectra in Figure 3-22 indicate that the core-shell particles promote the photon-electron conversion of DSSCs when incoming light excites the surface plasmons of core-shell particles. IPCE increases where core-shell particles increase the light absorption of TiO_2 films. In addition, it is noted that a small hump is observed in the IPCE spectrum of the mixed films in the range from 600 nm to 650 nm where the core-shell particles manifest the scattering, as shown in Figure 3-15c. One-to-one correspondence in IPCE and UV/Vis absorption spectra of TiO_2 – core-shell composite films suggests that photons which are absorbed or scattered by the core-shell particles are successfully converted to electrons in DSSCs.

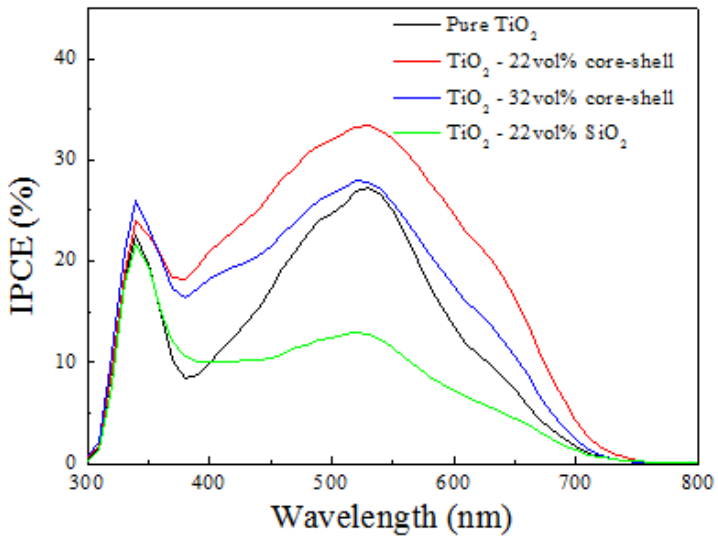

Figure 3-22. Incident photon-to-current efficiency (IPCE) curves of DSSCs using TiO_2 film or mixture films containing different amount of core shell particles, as photoanodes (as a reference sample, the TiO_2 - SiO_2 mixture film was also tested)

Thus, the optical cross section of the dye sensitizers can be significantly enhanced in the visible range by using more core-shell particles, leading to higher energy conversion efficiency of DSSCs. However, when the amount of the core-shell particles reaches a critical point, the

trade-off between the smaller surface area and the increase in the optical cross section of the dye restricts the effect of the surface plasmons on the photon-electron conversion, as demonstrated in DSSCs containing 32 vol% core-shell particles.

4.0 PLASMONIC TUNING EFFECT IN DSSC

4.1 BACKGROUND

Metallic nanostructures, a new class of photonic components, have rapidly developed during the past decade. This is due to their ability to control and manipulate light at the nanoscale level, which is related on localized surface plasmons (SPs).[1, 2] SPs are a result of optically induced oscillations of the free electrons,[64] which can be coupled to the optical wave as propagating surface waves or localized excitations. SPs are strongly depended on the topology and geometry of the metallic nanostructures.[117-119] In particular, plasmonic core-shell particles, which consist of a spherical dielectric core coated with a concentric layer of metallic nanoshell, are versatile subwavelength optical components, the surface plasmon resonance of which can be tuned by simply varying the thickness of the metallic nanoshell and the diameter of the inner core.[30, 31] This unique adjustable nature of the plasmonic core-shell particles facilitates their applications in surface-enhanced Raman spectroscopy,[120, 121] high-resolusion bioimaging,[122, 123] thermal therapy,[124] and drug delivery.[125]

Recently, SPs have been extensively studied to determine their ability to enhance the light absorption of solar cells.[65] Specifically, analysis has focused on the extent to which the excitation of localized SPs traps incoming photons and is coupled to light absorption capability of surrounding semiconductor. Furthermore, studies show that the effective optical path length

can be dramatically increased by multiple and high-angle light scattering from the metallic nanostructures in the cell.

TiO_2 nanoparticle-based dye sensitized solar cells (DSSCs) have attracted a vast amount of scientific and technological interest for their potential cost effectiveness.[40] However, DSSCs suffer from a relatively small optical cross section of dye molecules and a mismatch between the dye absorption spectrum and the solar spectrum.[41-43] One possible way to improve the light absorption of DSSCs is to increase the thickness of the photoelectrode. However, as the photoelectrode gets thicker, carrier diffusion length becomes comparable to the thickness of the photoelectrode and carrier collection efficiency starts to decrease.[65] Hence, when the photoelectrode is thicker than 20 μm, the effect of the photoelectrode thickness on the efficiency of DSSCs is saturated.[126] In addition, the increase in the thickness of TiO_2 film deteriorates open circuit voltage (V_{oc}) and fill factor, because of the increased back electron transfer between I_3^- ions and conduction band electrons in TiO_2 film.[127]

SPs have been found to be an effective way to improve the energy conversion efficiency in DSSCs without increasing the thickness of the photoelectrode, since its generated plasmonic near-field can increase the absorption and/or scattering of incoming light. Both bare[128] and surface coated metallic nanoparticles[85, 86, 104] were successfully explored in DSSCs for light harvesting. However, their plasmonic frequency is pre-determined by the type of metals and less influenced by the size of the nanoparticles. Therefore, the metal nanoparticles may have difficulty in matching the frequency of the surface plasmons with the dye absorption spectrum, which depend on the unique molecular structure of dyes.[129-132] To address this problem, several groups have changed the shape of the nanostructure metals and shifted the surface plasmon frequency within the absorption spectrum of DSSCs. Chang et al. investigated the role of Au

nanorods and demonstrate that the light absorption spectrum of the dye and the plasmonic frequency can be matched by changing the shape of nanostructured metal.[133] Recently, we have also shown that the surface plasmons of a metal nanoshell can improve the energy conversion efficiency of DSSCs.[113] The metal nanoshell couples with incoming light in wavelengths longer than the characteristic wavelength of the metal nanosparticles. Through this coupling, the core-shell structure offers us the capability to design unique plasmonic particles for different dyes, due to its optical tunablity.[134]

In this study, we tuned the surface plasmon frequency of the core-shell particles and examined effect on the performance of DSSCs. The absorption and scattering peaks of the core-shell particles are controlled by changing the size of the silica core. Then, the effect of surface plasmon frequency on light harvesting efficiency in DSSCs was examined using N719 dye and black dye, two commonly used photo-sensitizers in DSSCs.[135] Compared with N719, the light absorption spectrum of black dye extends to a longer wavelength. Hence, the two dyes require plasmonic particles with different surface plasmon frequency to enhance light absorption. In order to match the absorption spectra of the N719 dye and black dye, smaller (110 nm) or larger (470 nm) Ag@SiO_2 core-shell plasmonic particles were added to the TiO_2 photoelectrode. Our research has demonstrated that different core-shell particles increase the optical cross section of N719 and black dyes over red and green light via different mechanisms.

4.2 TUNING EFFECT OF SILVER NANOSHELL – SILICA CORE PARTICLES IN DSSC[136]

4.2.1 Sample Preparation and Characterization

SiO_2 spheres with uniform diameters were synthesized by Stöber method. By varying the volume ratio of these chemicals, the diameters of the silica spheres could be controlled as 90 nm and 450 nm separately. Ag@SiO_2 core – shell particles were fabricated following a two-step method.[113] Typically, to prepare core-shell particles with an average diameter of 110 nm, 15 ml of freshly prepared $[Ag(NH_3)_2]^+$ ion solution was added into 100 ml aqueous solution containing 225 mg silica nanospheres whose average diameter was 90 nm. The mixture was then sonicated for 3 hrs at 20 ^oC by using the high-intensity ultrasound radiation. Resulting particles were centrifuged and washed to remove residual reagents. Purified particles were heated at 100 ^oC under nitrogen gas flow for 3 hrs to crystallize silver nanoparticles on the surface of SiO_2 particles. After thermal annealing, the fine powder turned to be dark brown, indicating that Ag nanoparticles were nucleated on the surface of the SiO_2 particles. These attached Ag nanoparticles were used as seeds to grow the thin silver layer on the silica cores in the future. During the second step, 27 mg dark brown powder (Ag seeds - SiO_2 core) and 100 ml aqueous solution containing 2.4 mM silver nitrate were sequentially added into a 250 ml three-neck bottle and mixed well. At 85 ^oC, 55 mg sodium citrate was added into the aqueous mixture and was maintained at 85 ^oC for 1 hr under vigorous stirring. After purification, Ag@SiO_2 core – shell particles with an average

diameter of 110 nm were obtained. Similarly, using different amount of chemicals, 470 nm $Ag@SiO_2$ core – shell particles were prepared following the same route.

Anatase TiO_2 nanoparticles were synthesized via the hydrothermal reaction, and pure TiO_2 nanoparticle films and TiO_2-$Ag@SiO_2$ mixture films were prepared by the novel chemical sintering method. Subsequently, the TiO_2 film or composite film covered FTO was merged in N719 ethanol solution at room temperature for 24 hrs. After drying it by nitrogen gas, the dye sensitized photoelectrode was sandwiched with thermally platinized FTO counter electrode. Between the two substrates, liquid electrolyte was filled and sealed by hot melt sealing tape.

The microstructure of the $Ag@SiO_2$ core-shell particles and the composite films were tested by scanning electron microscopy (SEM) (Philips XL 30) and transmission electron microscopy (TEM) (JEOL JEM-200 CX,). The crystal structure of the core-shell composite particles was detected using an X-ray diffractometer (XRD) (Philips Analytical X-Ray). Optical absorption and scattering spectra of the core-shell particles and the composite films were collected by UV/Vis spectrometer (Perkin Elmer, Lambda 35 UV/Vis Spectrometer) attached with an integrating sphere in the range from 300 nm to 900 nm. Photovoltaic properties of the DSSCs were measured under AM 1.5 G simulated sunlight with the aid of the electrochemical workstation (CHI 660C). The incident photon to current efficiency (IPCE) spectra of DSSCs was tested by illuminating the prototype device with a monochromatic beam in the visible range.

4.2.2 Results and Discussions

Figure 4-1 shows the transmission electron microscopy (TEM) images of $Ag@SiO_2$ core-shell particles that were grown via a two-step method. The average diameter of SiO_2 core is 450 nm (Fig. 4-1a) or 90 nm (Fig. 4-1d). In both cases, the successful deposition of the Ag nanoshell was

observed. In the first step of the coating, Ag nanoparticles with a diameter of 3 – 5 nm were attached to the surface of SiO_2 particles (Fig. 4-1b, 4-1e), which would become the nucleus for further growth of Ag shell. After the second step, a uniform Ag shell was formed. The average shell thickness of the bigger and smaller ones was both around 10 nm.

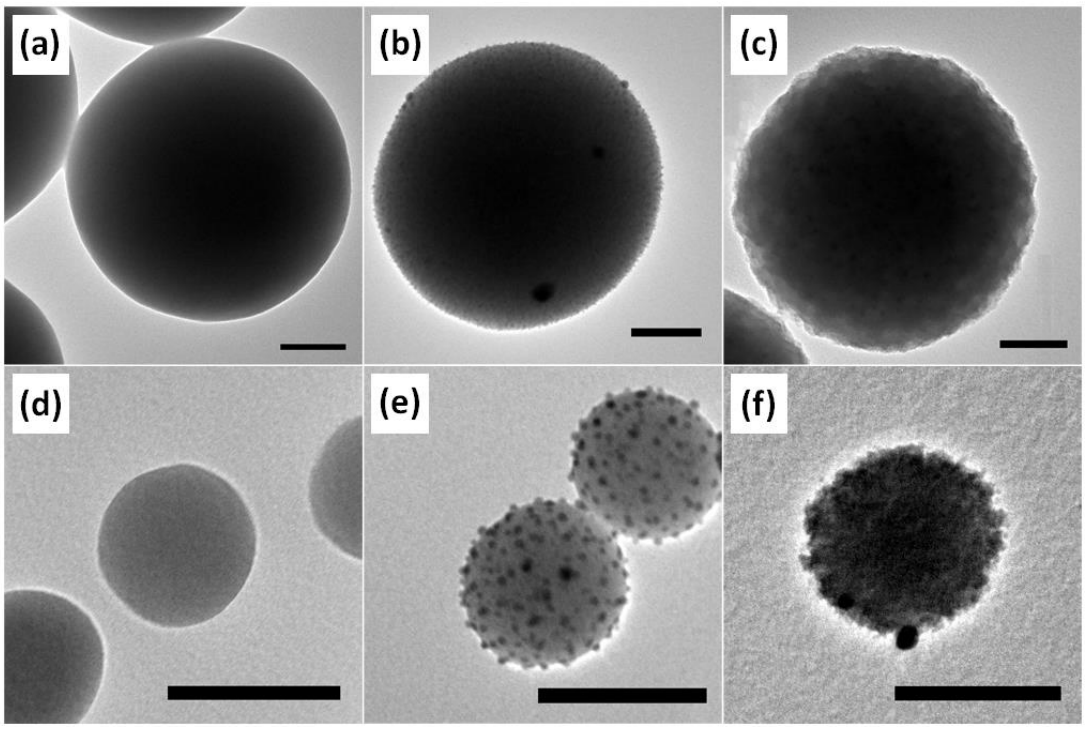

Figure 4-1. TEM images of the evolution procedure of the Ag@SiO_2 core-shell particles. (a) bare SiO_2 sphere with a diameter of ~ 450 nm, (b) Ag seeds deposited SiO_2 sphere with a diameter of ~ 450 nm, (c) 470 nm Ag@SiO_2 core-shell particle with a shell thickness of ~ 10 nm, (d) bare SiO_2 sphere with a diameter of ~ 90 nm, (e) Ag seeds deposited SiO_2 sphere with a diameter of ~ 90 nm, (f) 110 nm Ag@SiO_2 core-shell particle with a shell thickness of ~ 10 nm

Figure 4-2 shows the extinction spectra of silica core – silver shell particles dispersed in water. In addition to the UV/vis spectra (Fig. 4-2a), the results of theoretical calculations are presented for comparison (Fig. 4-2b). In UV-vis spectra, two peaks are found. A broad plasmon peak is found near 650 nm for the core-shell particles with a diameter of 110nm and near 800 nm for the core-shell particles with a diameter of 470 nm. The extinction of light at red and infrared

regime is the result of absorption and scattering by Ag nanoshells. The correlation with size clearly indicates that the wavelength of the coupled plasmon mode in core-shell particles can be controlled by simply changing the size of the core. An increase in the extinction in the longer wavelength is due to the size of the core-shell particles, and an appearance of the multiple peals is attributed to a hybridization of charge oscillations at the outer and inner surfaces of the shell.[31] In addition, both samples have a peak at 410 nm that corresponds to the plasmon resonance frequency of silver nanoparticles. The shorter wavelength peak implies that Ag nanoshells also interact with incoming light as nanoparticles that are physically attached to the outer surface of the shell. The extinction coefficieny of the metal nanoshells or metal nanoparticles was calculated via a generalized Mie scattering approach. Fig. 4-2b shows that the increase in the core size shifts the peak of the extinction spectrum to a longer wavelength. Similarities in the general trend between the experimental and theoretical results confirm our analysis of the experimentally measured extinction spectra of the core-shell particles.[94, 96] It is noted that the width of the experimentally observed plasmon peaks is broader than the width of the calculated plasmon peaks. Several factors contribute to this broadening effect of the plasmon peaks of the silver nanoshell. One is the size distribution of the silica core diameter and the silver shell thickness and the other is surface roughness of the silver nanoshells.[31] In addition, if the mean free path of the electrons is larger than the dimension of the nanoparticle, an extra broadening of the surface plasmon peaks occurs.[17]

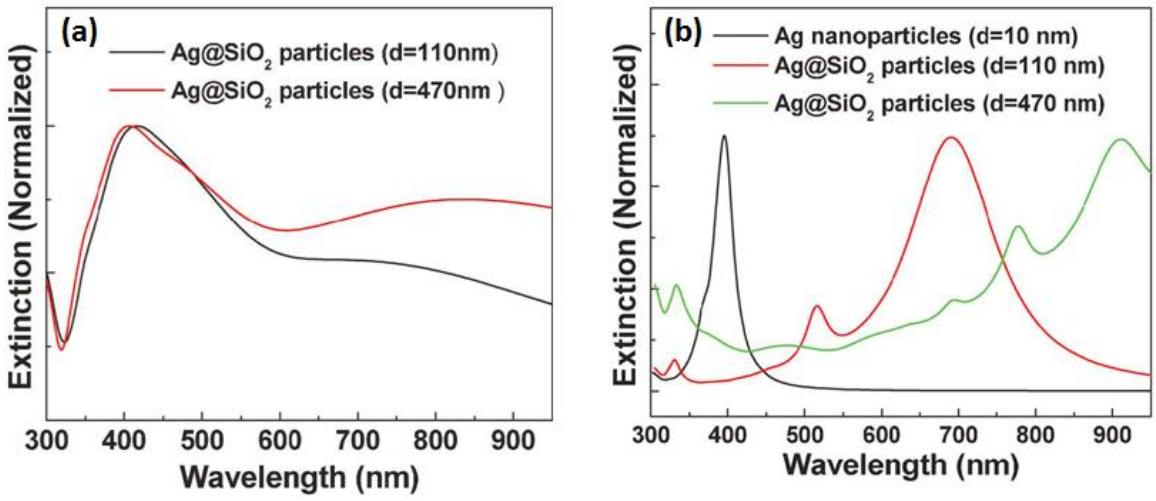

Figure 4-2. UV-vis extinction spectra of 110 nm $Ag@SiO_2$ core-shell particles and 470 nm $Ag@SiO_2$ core-shell particles in aqueous solution (a) experimental data, (b) calculated data (a calculated spectrum of Ag nanoparticles is also added for comparison)

In order to fabricate the photoelectrode of DSSCs, the aqueous solution of the core-shell particles was mixed with the slurry of TiO_2 nanoparticles which were prepared using the hydrothermal method. The mixture slurry was pasted on fluorine doped tin oxide (FTO) coated glass and thermally annealed. Figure 4-3 presents SEM micrographs of TiO_2 mesoporous films embedded with the core – shell particles. It clearly shows that large core – shell particles with an average diameter of 110 nm or 470 nm are uniformly dispersed in TiO_2 nanoparticle matrix. Furthermore, the distance between the outer surfaces of the core-shell particles in Fig. 4-3 quantitatively fits well with the calculated one, which is about 42 nm for 20 vol% 110 nm core-shell particle added film, and 178 nm for 20 vol% 470 nm core-shell particle added film. Figure 4-3E shows the optical micrograph of pure TiO_2 film and composite films coated FTO substrates. From top to bottom, the film is composed of pure TiO_2, TiO_2/20 vol% 110 nm core-shell particles, and TiO_2/20 vol% 470 nm core-shell particles. A change in the color of the film proves that the addition of the plasmonic particles influences the optical property of the mesoporous

films. The silver phase in the mixture film is well crystallized during a thermal annealing procedure. In addition, a stronger intensity of silver XRD peaks for the 110 nm core-shell particle added film, is due to the higher surface area of smaller core-shell particles (Fig. 4-4).

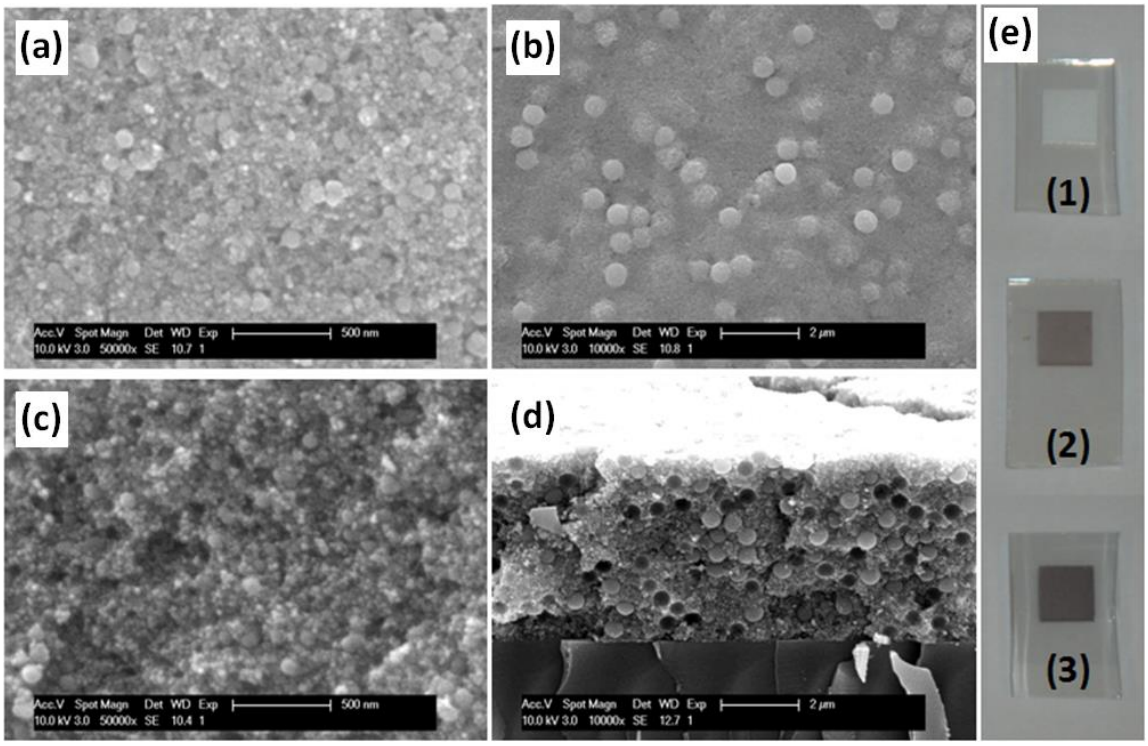

Figure 4-3. SEM plan-view image of 20 vol% (a) 110 nm and (b) 470 nm Ag@SiO_2 core-shell particles embedded TiO_2 mesoporous film. SEM cross-section image of 20 vol% (c) 110 nm and (d) 470 nm Ag@SiO_2 core-shell particles embedded TiO_2 mesoporous film. (e) an optical micrograph of photoanode coated FTO substrate. From top to bottom, the photoanode is pure TiO_2 film, 20 vol% 110 nm Ag@SiO_2 embedded TiO_2 mesoporous film, and 20 vol% 470 nm Ag@SiO_2 embedded TiO_2 mesoporous film, separately. The area of the film is 5×5 mm^2

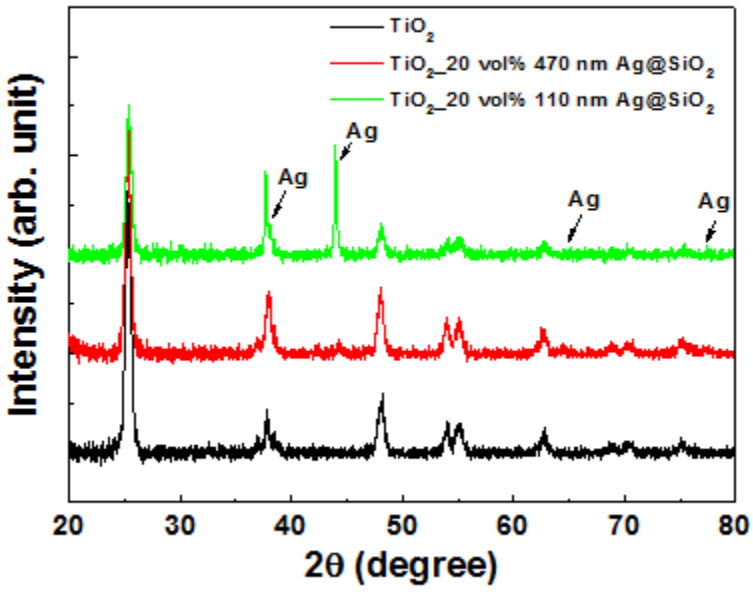

Figure 4-4. XRD spectra of pure TiO_2 film, TiO_2/470 nm Ag@SiO_2 composite film and TiO_2/110 nm Ag@SiO_2 composite film after thermal annealing at 450 ^oC for 30 min under the flow of N_2 gas

The light absorption and scattering properties of the TiO_2 based composite films with 110 nm or 470 nm diameter Ag@SiO_2 core-shell particles are shown in Figure 4-5. Since the refractive index of TiO_2 ($n \approx 2.3$) surrounding the core-shell particles is larger than that of water, the peaks of the spectra shift to a longer wavelength. A long tail of the absorbance spectra of the composite films results from the overlapping of the elementary plasmon peaks of the core-shell particles. In addition to the absorption, the scattering behavior of the composite films is also measured. Larger core-shell particles display a stronger scattering effect over red and IR light and smaller core-shell particles causes a higher absorption over green and orange light. A change in the relative magnitude of absorption and scattering by different core-shell particles qualitatively agrees with the theoretical predictions in Fig. 4-2b. As the core size increases from

90 nm to 450 nm, the surface plasmons peak of the nanoshell shifts to a longer wavelength and the scattering efficiency of the plasmonic particles in the near IR regime increases.

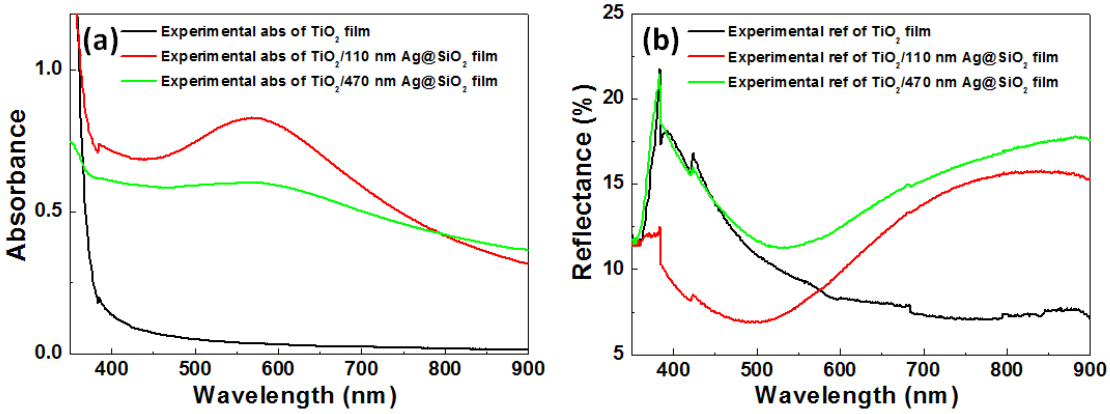

Figure 4-5. Experimental data of (a) UV-vis absorbance spectra and (b) reflectance spectra of TiO_2 film, TiO_2 / 110 nm $Ag@SiO_2$ composite film, and TiO_2 / 470 nm $Ag@SiO_2$ composite film

The mixture films were dipped in the solution of dye molecules (N719 or black dye). The absorption spectrum of adsorbed dye molecules are shown in Figure 4-6. For this measurement, sensitized thick films were immersed in NaOH solution to separate the dyes from the photoelectrode. The amount of adsorbed dye molecules in Figure 4-6 is consistent with the ideal surface area ratio of the photoelectrode, which suggests that the dye molecules are uniformly coated on both TiO_2 and core-shell particles of the photoelectrode. This surface passivation of the core-shell particles by dye molecules plays the role of a capping layer and improves the chemical stability of the silver shell.[113] Figure 4-7 shows the effect of the dye coating on the corrosion resistance of the core-shell particles. UV/Vis absorbance spectra of the N719 dye or black dye coated TiO_2-core-shell composite films did not show a change after they were immersed in the electrolyte for 1 day. Some increase in the blue region in the electrolyte-dipped

sample is due to a small amount of the residual electrolyte attached to the films. This result supports the chemical stability of the dye coated Ag nansohell in the electrolyte.

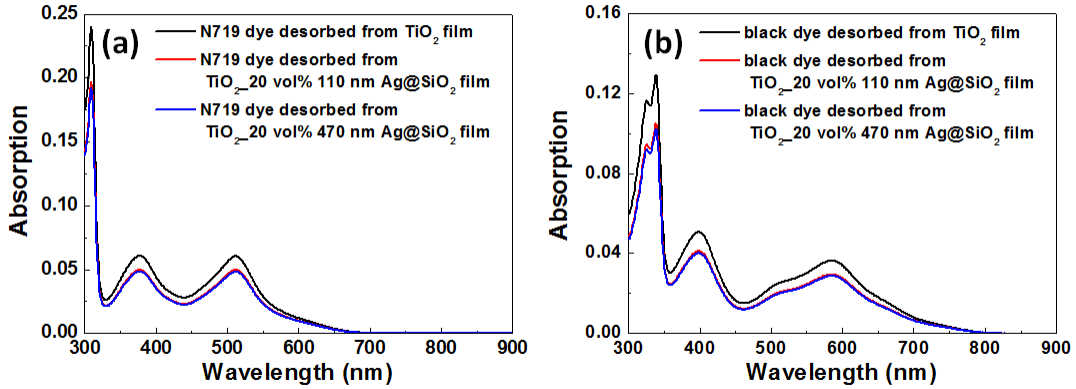

Figure 4-6. Comparison of UV-vis absorption spectra of desorbed dye from pure TiO_2 film, 110 nm $Ag@SiO_2$ embedded composite film and 470 nm $Ag@SiO_2$ added composite film with (a) N719 dye or (b) black dye

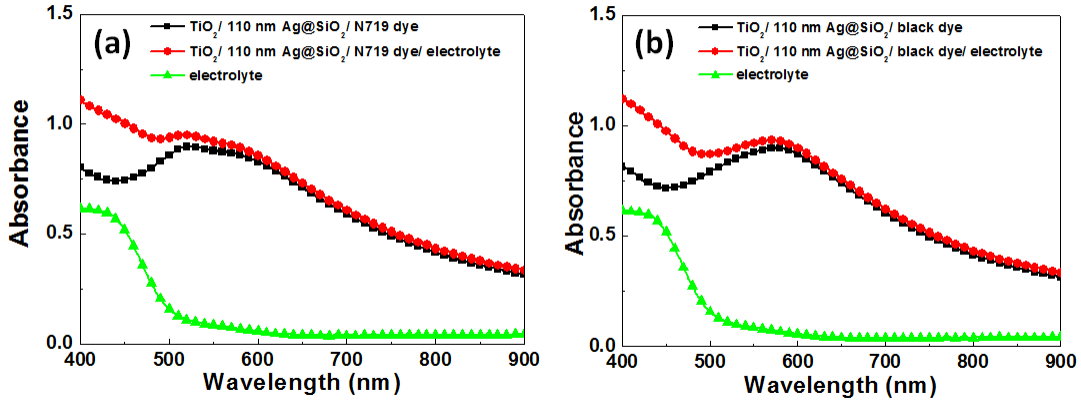

Figure 4-7. UV/Vis spectra of dye coated photoelectrodes containing 110 nm core-shell particles before and after immersed in electrolyte (Iodolyte AN-50) for 1 day; (a) N719 dye and (b) black dye

DSSCs were built upon the dye coated composite films with the thickness of 7 μm. N719 dye is a widely used dye. Compared with N719, the absorption spectrum of black dye is larger toward the red and infrared regime, but the optical cross section of black dye over green light is

smaller.[137, 138] Therefore, N719 and black dye are expected to respond differently to 110 nm and 470 nm core-shell particles. Figures 4-8a and 4-8b show *J-V* curve and incident photon to current efficiency (IPCE) spectra of DSSCs employing N719 dye. They clearly indicate that the addition of $Ag@SiO_2$ particles enhances the energy conversion efficiency of DSSCs, although the amount of adsorbed dye molecules is decreased in $Ag@SiO_2$ particle added photoelectrodes. 470 nm core-shell particles into TiO_2 films increase short circuit current (J_{sc}) from 14.6 mA cm^{-2} to 15.7 mA cm^{-2} (Table 4-1). This enhancement was more pronounced when 110 nm core-shell particles were added.

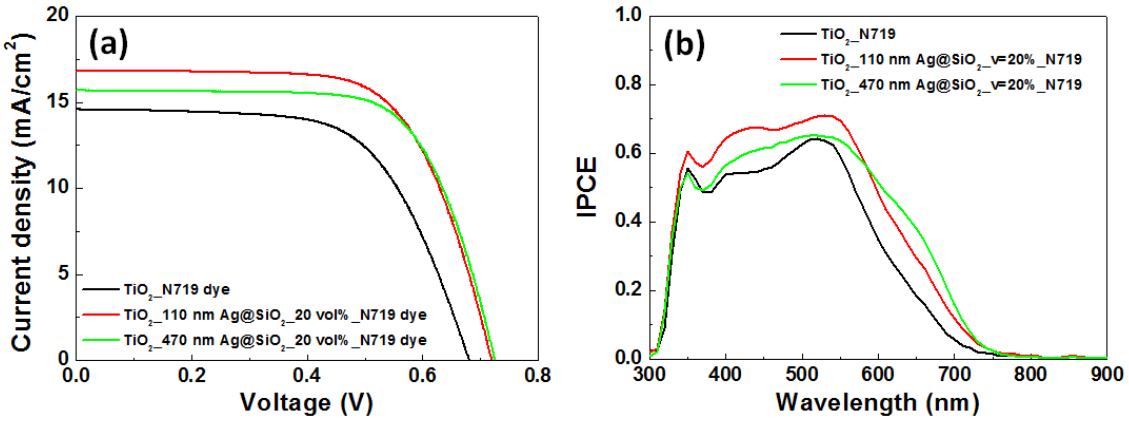

Figure 4-8. Comparison of the (a) *J-V* curves and (b) IPCE spectra of N719 dye sensitized solar cells containing TiO_2 film, 20 vol% 110 nm $Ag@SiO_2$ core-shell particles embedded TiO_2 mesoporous film, and 20 vol% 470 nm $Ag@SiO_2$ core-shell particles embedded TiO_2 mesoporous film

IPCE spectra of DSSCs in Figure 4-8b show that $Ag@SiO_2$ particles increase photon-electron conversion efficiency in two ways. Increases in absorption for shorter wavelength regime and scattering for longer wavelength regime enlarge effective light intensity near dye molecules and enhances photocurrent generation. It is noted that 110 nm core-shell particles improve the photocurrent generation more effectively in the shorter wavelength range and that

470 nm ones work better in longer wavelength range. At the wavelength of 650 nm, the normalized IPCE is very dependent on the size of the Ag nanoshell. A difference in the improvement of IPCE spectra by two kinds of core-shell particles agrees well with their different spectral response shown in Figure 4-2. This indicates that a change in the geometric factor of the core-shell particles can be used to tune the photon-electron conversion process of the solar cells.

Table 4-1. Photovoltaic performance of DSSCs based on different films with different dyes

Film	**Dye**	V_{oc} **(V)**	J_{sc} **(mA/cm^2)**	**FF (%)**	**PCE (%)**
TiO_2	N719 dye	0.68	14.6	63	6.2
TiO_2/110 nm Ag@SiO_2	N719 dye	0.72	16.8	67	8.1
TiO_2/470 nm Ag@SiO_2	N719 dye	0.73	15.7	69	7.9
TiO_2/90 nm SiO_2	N719 dye	0.72	11.6	70	5.9
TiO_2/450 nm SiO_2	N719 dye	0.70	12.3	71	6.1
TiO_2	Black dye	0.63	7.4	72	3.4
TiO_2/110 nm Ag@SiO_2	Black dye	0.70	9.0	70	4.4
TiO_2/470 nm Ag@SiO_2	Black dye	0.70	11.7	72	5.9

Since 20 vol % of the composite film was occupied by large core-shell particles, the surface area of the mixture film for dye absorption also almost 20% decreased. In order to show the real improvement of the cell performance after employing core-shell particles, a control experiment was conducted using composite films containing the same amount of bare silica particles without silver layer coating. Both the *J-V* curve and IPCE show a dramatic decrease in the cell performance (Figure 4-9), due to the decreased total surface area for dye absorption. This indicates that it is mainly the plasmonic Ag nanoshell enhances the performance of DSSCs.

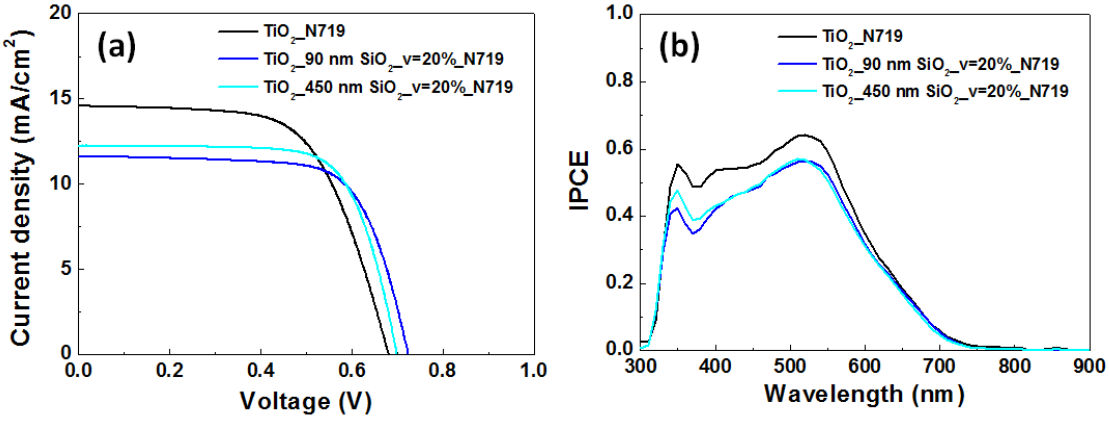

Figure 4-9. (a) *J-V* curves and (b) IPCE spectra of N719 dye sensitized solar cells of reference TiO_2 film, 20 vol% 90 nm SiO_2 embedded TiO_2 film, and 20 vol% 450 nm SiO_2 embedded TiO_2 film

It is noted that the core-shell particles in the photoelectrode also increase open circuit voltage (V_{oc}) of DSSCs. Electrochemical impedance spectrum (EIS) analysis and SLIM-PCV method were performed to understand the difference in charge recombination rate and electron lifetime for core-shell particle embedded DSSCs and reference cell. Figure 4-10a shows the Nyquist plots of the DSSCs. The core-shell particles decrease an impedance circle in the frequency regime of 10^0-10^3 Hz (ω_3) which corresponds to the impedance at the TiO_2/dye/electrolyte interface of DSSCs.[139] This is because plasmon can enhance the injected electron density of the conduction band of TiO_2 nanoparticles. In addition, in Figure 4-10b, Bode plots show that a frequency of maximum impedance in the ω_3 region shifts to lower frequency region when the core-shell particles are added to DSSCs. This indicates that the carrier lifetime (τ) is increased by addition of the core-shell particles. A plot of lifetime vs. J_{sc} in Figure 4-10c also supports the role of the core-shell particles in the increased carrier lifetime, which is attributed to suppressed carrier recombination by insulating silica cores and Schottky barrier at TiO_2/Ag shell interface.[105, 140, 141] This Schottky barrier prohibits the photo-generated electron

transferring from TiO_2 to Ag nanoshell, so it can suppress the carrier trapping and recombination by the silver nanoshell.

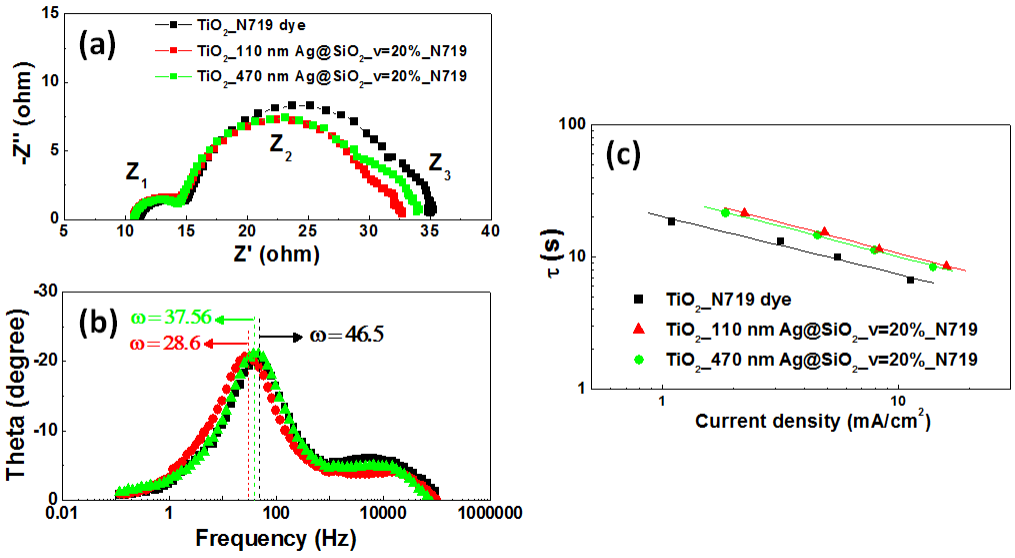

Figure 4-10. (a) Nyquist plots and (b) Bode plots of DSSCs with N719 dye. (c) Lifetime vs. J_{sc} plots of DSSCs with N719 dye

The enhanced photon-electron conversion by the core-shell particles is more clearly observed in black dye DSSCs. The light absorption ability of black dye molecules is smaller than that of N719 dye, due to the low extinction coefficient and surface coverage of black dye.[138] Therefore, the role of core-shell particles in light management is more critical in the light harvesting of black dye DSSCs than N719 DSSCs. As shown in Figure 4-11a, J_{sc} of typical black dye DSSCs increases from 7.4 mA cm^{-2} to 9.0 mA cm^{-2} when 110 nm core-shell particles are added into TiO_2 mesoporous films. The increase in J_{sc} is more dramatic when the same amount of 470 nm core-shell particles is added. J_{sc} reaches 11.7 mA cm^{-2} in the core-shell particle added black dye DSSCs (Table 4-1). Better performance of 470 nm core-shell particles in black dye DSSCs is traced to the fact that the absorption and scattering spectra of larger core-shell particles

are pushed to longer wavelength range where black dye works better than N719 dye. V_{oc} of the core-shell particle embedded DSSCs is slightly larger than that of a control sample of pure TiO_2 nanoparticle based DSSCs, which is similar to the core-shell particle added N719 dye. Given that the addition of 20 vol% core-shell particles decreases the amount of adsorbed dye almost by 20%, an increase in J_{sc} from 7.4 mA cm^{-2} to 11.7 mA cm^{-2} indicates that the core-shell particles of 470 nm can improve the cross section of black dye in DSSCs by a factor of two. In this high efficiency DSSCs consisting of black dye and core-shell particles, aging or corrosion is negligibly observed.

Figure 4-11b shows the IPCE spectra of black dye DSSCs. Both 110 nm and 470 nm core-shell particles increase the photon-electron energy conversion efficiency. Compared with 110 nm particles, a uniform increase in IPCE is observed in the range of 500 nm to 800 nm where larger core-shell particles cause higher scattering and absorption of incoming light. It reveals that the enhanced photocurrent generation of black dye DSSCs is correlated to the enhanced scattering and absorption by the core-shell particles. The performance of DSSCs using black dye as the sensitizer exemplifies the benefit of the tuning capability of the Ag nanoshell. Compared with N719, which is widely used in dye sensitized solar cells, the black dye has an advantage of a broad light absorption spectrum. Black dye can collect more photons in red and infrared light than N719 dye, which can increase the theoretical energy conversion efficiency of the DSSCs. However, black dye has the critical problem of a small optical cross section and weak surface coverage. Hence, DSSCs with black dye should employ a very thick photoelectrode to absorb a large enough amount of solar light. The thick photoelectrode is likely to prevent the electron transport, which, in turn, reduces the energy conversion efficiency of DSSCs greatly below the theoretical limit. Results in Fig. 4-11 attest that the Ag nanoshell can

solve the problem of the small optical cross section of black dye and increase the theoretical limit of DSSCs.

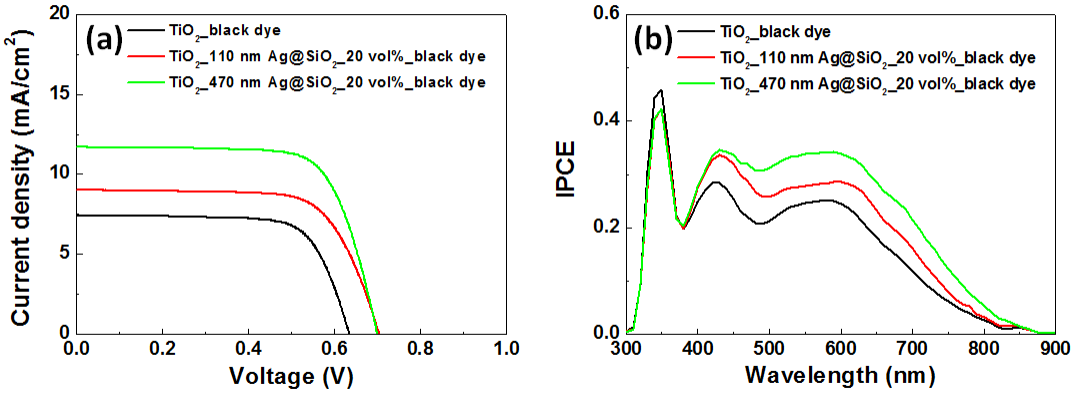

Figure 4-11. Comparison of the (a) *J-V* curves and (b) IPCE spectra of black dye sensitized solar cells containing TiO_2 film, 20 vol% 110 nm $Ag@SiO_2$ core-shell particles embedded TiO_2 mesoporous film, and 20 vol% 470 nm $Ag@SiO_2$ core-shell particles embedded TiO_2 mesoporous film

5.0 DUAL PLASMON ASSISTED HIGH PERFORMANCE IN LEAD SULFIDE SOLAR CELLS

5.1 BACKGROUND

Quantum Dots (QDs) have attracted a great deal of research interest over the past few decades due to their unique optical and electronic properties.[142] Their large optical cross section, tunable band gap and slow phonon relaxation are valuable physical properties that are driving their use in solar energy conversion devices, i.e., solar cells. In addition, QDs can be made through inexpensive solution-based synthesis, and they are proving amenable to facile and large-scale device fabrication methods. Hence, QDs have been used recently for different types of photovoltaic devices.[143] However, better device structures are needed for QD-based photovoltaics to compete with the conventional technologies which are already commercialized.

QDs of lead chalcogenide , such as PbS and PbSe, have large Bohr exciton radius, low exciton binding energy, and are considered excellent absorbers of visible and near IR light.[144] Because of this promise, several groups have performed exploratory research to pave the way toward creation of hybrid solar cells using *p*-type lead chalcogenide QDs as the photoactive component of the solar cells.[145] Moreover, QD solar cells have the potential of generating multiple excitons from a single hot carrier, which is an inverse Auger type process.[146, 147]

Recently, the concept of multiple exciton generation (MEG) has been experimentally proven in a thin-film type solar cell.[148-151] The configuration of a so called thin-film type colloidal quantum dots (CQDs) solar cell, as proposed by Sargent[152-154] and Nozik,[155, 156] contains a Schottky barrier between a QDs semiconductor film and a metal thin film, where the photogenerated carriers are collected.. From the standpoint of processing, this QD layer has the strength of easy deposition using a spin coating process[154, 157] or a layer-by-layer dip coating process.[158] One main drawback of the QD/metal structure is a low open circuit voltage (V_{oc}), which is determined by the separation of the quasi-Fermi levels at the contacts to the photoactive layer.[159] To solve the problem of low V_{oc}, a layer of an *n*-type wide bandgap semiconductor such as TiO_2[159, 160] or ZnO has been inserted between the QD layer and transparent conducting layer to form a depleted heterojunction structure.[161] This heterojunction changes the electron transport direction and increases the quasi-Fermi level difference, leading to a higher V_{oc}.[159]

In the thin-film type solar cells with Schottky junction and p-n junction, a tradeoff between light absorption and carrier extraction is an important issue.[162, 163] As the thickness of the QD film increases to several hundreds of nanometer, the QD film can absorb more incoming photons. However, since diffusion length of minority carrier becomes comparable to the QD film thickness in a thick QD film, a probability for the carrier recombination increases and a charge collection efficiency decreases.[156] This shows an importance of increasing light absorption without changing the QD layer thickness in heterojunction-type chalcogenide QD solar cells.

To date, many groups have worked on improving the energy conversion efficiency of CQDs solar cells. For this purpose, the effect of the QD size on the injection and potential energy of electrons has been investigated. One such group achieved optimum efficiency of the CQDs solar cell by employing medium size PbS QDs with a band gap of 1.53 eV. Smaller QD

diameters led to decreased light absorption and strengthened the Schottky barrier while larger QD diameters caused lower carrier extraction and higher carrier recombination.[164] In addition, the rate of charge transport between QDs is influenced by the length of surface ligands. Compared with long oleic chains, shorter thiol ligands, such as 1,2-ethanedithiol (EDT),[158] mercaptocarboxylic acids (MPA),[160] and benzenedithiol (BDT),[165] have been reported to shorten the inter-distance between adjacent QDs and facilitate carrier transport between QDs.

Thermal annealing has also been considered an effective way to enhance the conductivity and carrier mobility of the thiol-capped CQDs film. Thermal treatment of QDs reduces the inter-CQDs separation or facilitates particle aggregation along preferential crystallographic axes.[166-168] Zhao *et al.*[169] reported that mild thermal annealing of the PbS QDs film in air greatly enhances the fill factor (ff) and V_{oc} of the PbS/organic bilayer solar cell. Formation of an inert interfacial layer such as $PbSO_3$ or PbO after annealing was shown to limit current leakage and suppress charge recombination. Very recently, Gao *et al.*[170] found that electronic coupling between the QDs and carrier transport in QD film of ZnO/PbS QDs/MoO_x/Al solar cells are improved during thermal annealing in an inert atmosphere.

Recently, surface plasmons of metallic nanostructures have attracted great attention, in part because they can improve the light harvesting efficiency of solar cells. Metallic nanostructures can increase both the near-field intensity and the light scattering efficiency.[65] If a light absorbing semiconductor is located near a plasmonic structures, the increase in the local field intensity allows the semiconductor to absorb more light. Therefore, plasmonic nanostructures have been employed in both traditional silicon based solar cells[171-173] and emerging types of solar cells, such as dye sensitized solar cells and organic solar cells, to improve their light harvesting efficiency.[86, 174-177] It is important to match the surface plasmon

frequency with the light absorption spectrum of the photoactive materials. Thus different metallic nanostructures have been studied, for example, nanoshells,[30, 35, 178] nanocages,[179, 180] nanoeggs[181-183] and nanorods,[184-186] because they provide tunable surface plasmons which are exploited to improve the light absorption capability of photovoltaic devices.[113, 133, 187, 188] Particularly, the plasmonic core-shell nanostructures, consisting of a silica sphere as the dielectric core and a metal as the nanoshell, have been successfully utilized in PV devices such as dye sensitized solar cells and QD solar cells.[113, 136] Their unique surface plasmonic behavior arises from the symmetric or anti-symmetric coupling of plasmons produced on the inner surface and outer surface of the metal shell.[39]

Here, we employed plasmonic SiO_2@Au@SiO_2 (SGS) core-shell-shell particles to enhance the photon-electron conversion efficiency in PbS QD thin film solar cells. The outer silica layer, which overcoats the intermediate Au shell, enhances its chemical stability and inhibits carrier trapping by the metal shell. In the plasmonic PbS QD solar cells, we systematically studied the effect of the location of the plasmonic particles on the performance of PbS QD heterojunction-type thin film solar cells (fluorine doped SnO_2 (FTO) /TiO_2/PbS/Au) from the standpoint of light absorption enhancement. For this purpose, we chose two different designs with the SGSs placed either at the PbS-Au interface or the PbS-TiO_2 interface. We found that a dual enhancement was achieved for the devices with the SGSs at the PbS-TiO_2 interface because it causes nanodome structures to form on the top Au electrode.

5.1.1 PbS QDs and Surface Ligands

Comparing with the first excitonic transition peak at λ = 3200 nm for bulk PbS (E_g = 0.41 eV), the first excitonic transition of the PbS QDs, whose average diameter is less than 10 nm, can

reach to near IR or visible regime. Then a strong quantum confinement will be realized due to a large Bohr radius (18 nm) of the PbS. The PbS QDs can be prepared by a classical procedure developed by Hines and Scholes,[144] in which the long oleic chain is used as the passivation layer for size and stability control. Typical morphology of the PbS QDs with an average diameter of 6.5 nm is shown in Figure 5-1a. The first excitonic absorption of the PbS QDs can be readily tuned from 800 nm to 1700 nm as the diameter of the particle increases from 3 nm to 7 nm (Fig. 5-1b).[144, 164]

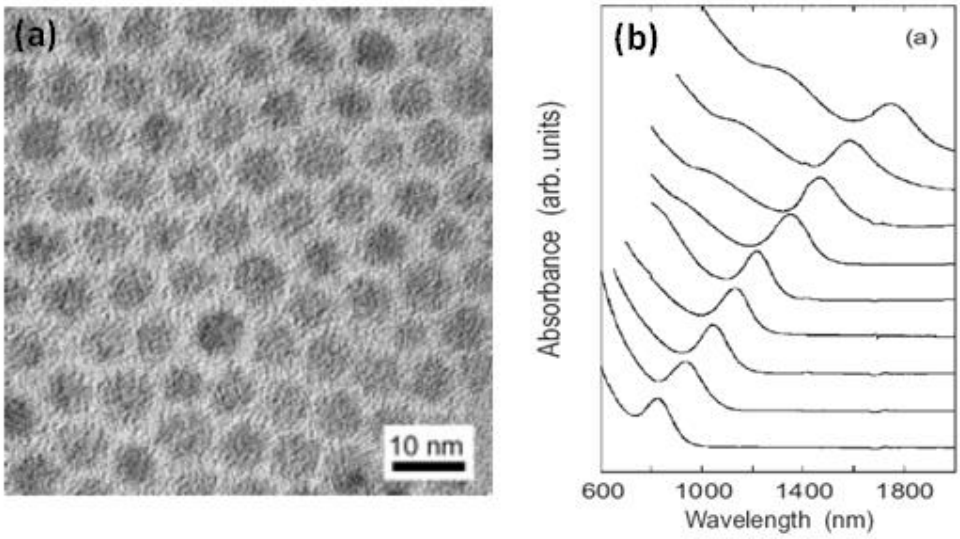

Figure 5-1. (a) HRTEM images of colloidal PbS QDs with an average diameter of 6.5 nm. (b) Optical characterization of toluene solutions of oleic acid capped PbS QDs [144]

Surface ligands play an important role in colloidal QDs synthesis, since they control the nanoparticle nucleation, growth and surface passivation. In addition, surface ligand is a key factor for assembling individual particles into ordered NC solid and film. So far, four types of ligands have been widely utilized in nanocrystal preparation, such as molecules with single head group and a long hydrocarbon chain, short-chain molecules with single head group, cross-linking molecules with two end groups and metal chalcogenide complexes (Figure 5-2).[142]

Ligand type	Molecular structure	Interparticle spacing	Functions, characteristics, typical examples
Molecules with single head group and a long hydrocarbon chain	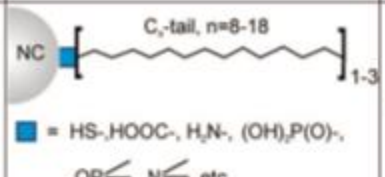	>1.5 nm	• Most common ligands used for NC synthesis • Form stable colloidal solutions • Hydrophobic surface • Form highly insulating NC solids, $\sigma \sim 10^{-12}$-10^{-9} S cm^{-1}
Short-chain molecules with single head group	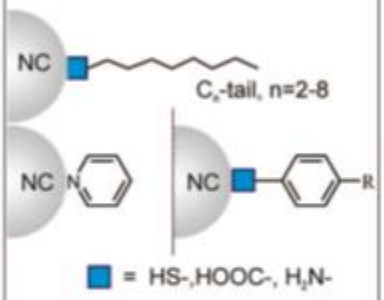	0.3-1 nm	• Treatment of NC solids or ligand-exchange in solutions • Decreased colloidal stability • Improved electronic transport compared to long-chain ligands • Reported detectivity of ~10^{12}-10^{13} Jones in photodetectors on PbS NCs caped with butylamine • Conductivities of up to 10^{-1} S cm^{-1} in arrays of metallic NCs
Cross-linking molecules with two end groups	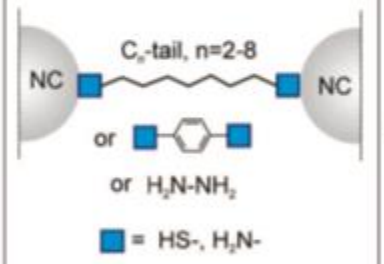	0.3-1 nm	• Mainly prepared by treating NC solids • μ up to 2 cm^2 V^{-1} s^{-1} in arrays of PbSe NCs treated with N_2H_4 • μ~10^{-2} cm^2 V^{-1} s^{-1} in arrays of CdSe NCs treated with 1,4-phenylenediame • Solar cells based on PbS and PbSe NC solids showed power conversion efficiencies of up to 2.1%
Metal chalcogenide complexes	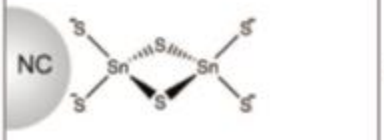	≥ 0.5 nm	• Prepared via solution phase ligand-exchange • Complete removal of original organic ligands • Hydrophilic surface • High conductivities of ~200 S cm^{-1} in Au-$Sn_2S_6^{4-}$NC solids

Figure 5-2. Different Types of Surface Ligands Used in Nanocrystals and Nanocrystal Solids [142]

Surface ligand with a long organic chain can passivate the charged surface of the nanoparticles and prohibit particle agglomeration and precipitation in the solution. However, it acts as bulky insulating barrier and hinders the inter-particle charge transportation. On the other

hand, the charge transportation between the nanoparticles will be facilitated by using short or cross-linking ligand. Furthermore, the cross-linking molecules enable the preparation of conductive and close packed nanocrystal film. In particular as shown in Figure 5-3, 1,2-ethanedithiol (EDT), who contains two strong SH^- functional groups, can substitute the long oleic acid (OA) chain on the pristine PbS QDs and binds to the Pb^{2+} rich surface.[189] By doing so, the interparticle spacing will be dramatically reduced, and nearest-neighbor hopping becomes the dominate mechanism in charge transportation.

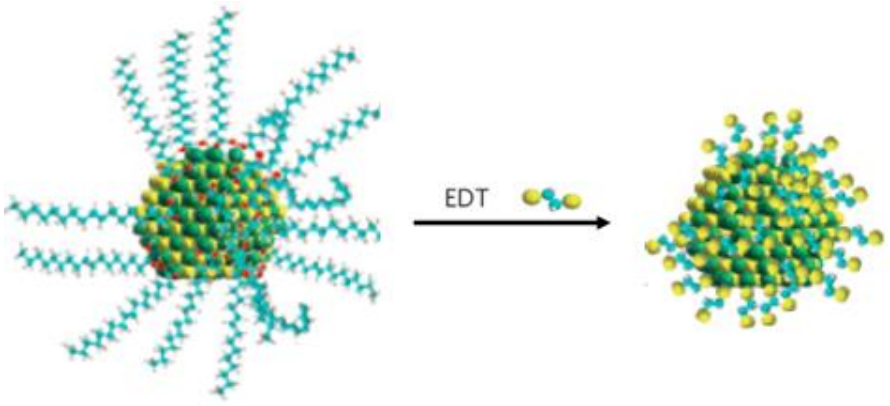

Figure 5-3. In the organic passivation route for PbS QDs, EDT substitutes the long OA ligands and binds to Pb^{2+} on the surface [189]

5.1.2 Schottky Solar Cells Based on Lead Chalcogenide Film

Sargent and Nozik reported a Schottky type colloidal quantum dots (CQDs) solar cell recently.[152-156] The device contains a Schottky barrier at the interface between lead chalcogenide (PbS or PbSe) film and low work function metal electrode (Mg, Al, Ca). Typically, the PbS film was deposited via a layer-by-layer dip coating or spin coating of PbS QDs/hexane solution, and then submerged into the EDT/acetonitrile solution for surface ligand exchange.

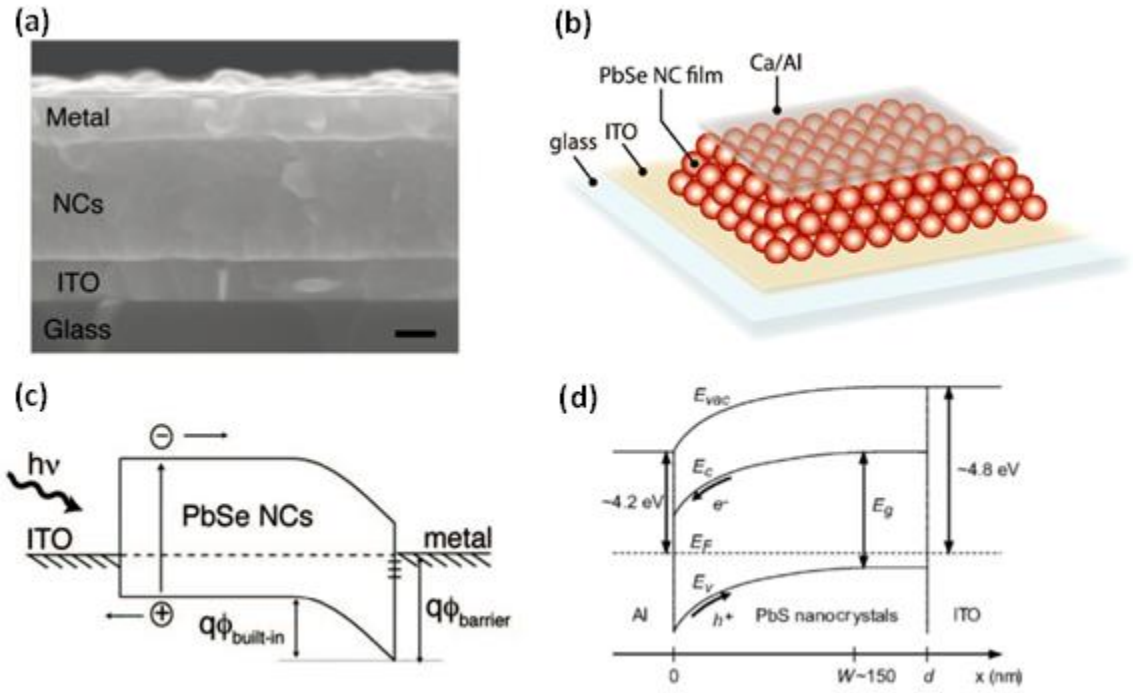

Figure 5-4. (a) Scanning electron microscopy cross-section of the ITO/PbSe_QDs/metal device stack. The metal is 20 nm Ca/100 nm Al. The scale bar represents 100 nm. (b) A cartoon of the PbSe QDs Schottky solar device.[155] (c) Proposed equilibrium band diagram. Showing the presence of a Schottky barrier and bending in the conduction band and valence band near the metal/PbSe QDs interface. The built-in electric field within the depletion region of electrons and holes.[156] (d) Similar band diagram of Schottky barrier near the Al/PbS QDs interface [163]

Device structure and proposed equilibrium band diagram are shown in Figure 5-4. For an ideal Schottky contact, $q\phi_B = Eg - q(\phi_m - \chi)$, where $q\phi_B$ is the barrier height, ϕ_m the work function of the metal and χ the electron affinity of the semiconductor. It indicates that Schottky barrier creates a built-in potential for fast electron-hole separation at the evaporated metal contact. Photogenerated electron will transfer into the metal electrode following the bended conduction band. And in the meanwhile, holes move backward to the ITO substrate along the valence band. The open circuit voltage (V_{oc}) of the device increases as the bandgap of the QDs film enlarges or the work function of the metal electrode decreases.

Mott-Schottky analysis permits a determination of depletion width, built-in potential and carrier concentration in the semiconductor film. The depletion width (W) of the Schottky junction is equal to

$$W = \sqrt{\frac{2\varepsilon\varepsilon_0(\phi_{bi}-V)}{qN}} \tag{5-1}$$

where ε is the static dielectric constant of the QDs film, ε_0 the permittivity of the free space, ϕ_{bi} the built-in potential, V the applied bias, and N the carrier concentration at the edge of the depletion layer. In addition, N can be calculated from the equation

$$N = \frac{1}{A^2}\frac{2}{\varepsilon\varepsilon_0\frac{d}{dV}(\frac{1}{C^2})} \tag{5-2}$$

where C is the capacitance of the depletion region and can be measured from the Mott-Schottky plots ($1/C^2$ vs. Voltage).

Time-of-flight technique (Figure 5-5a,b) can be applied to obtain the electron mobility and transient open circuit voltage decay (OCVD) to measure the recombination-limited lifetime of carriers (Figure 5-5c,d).

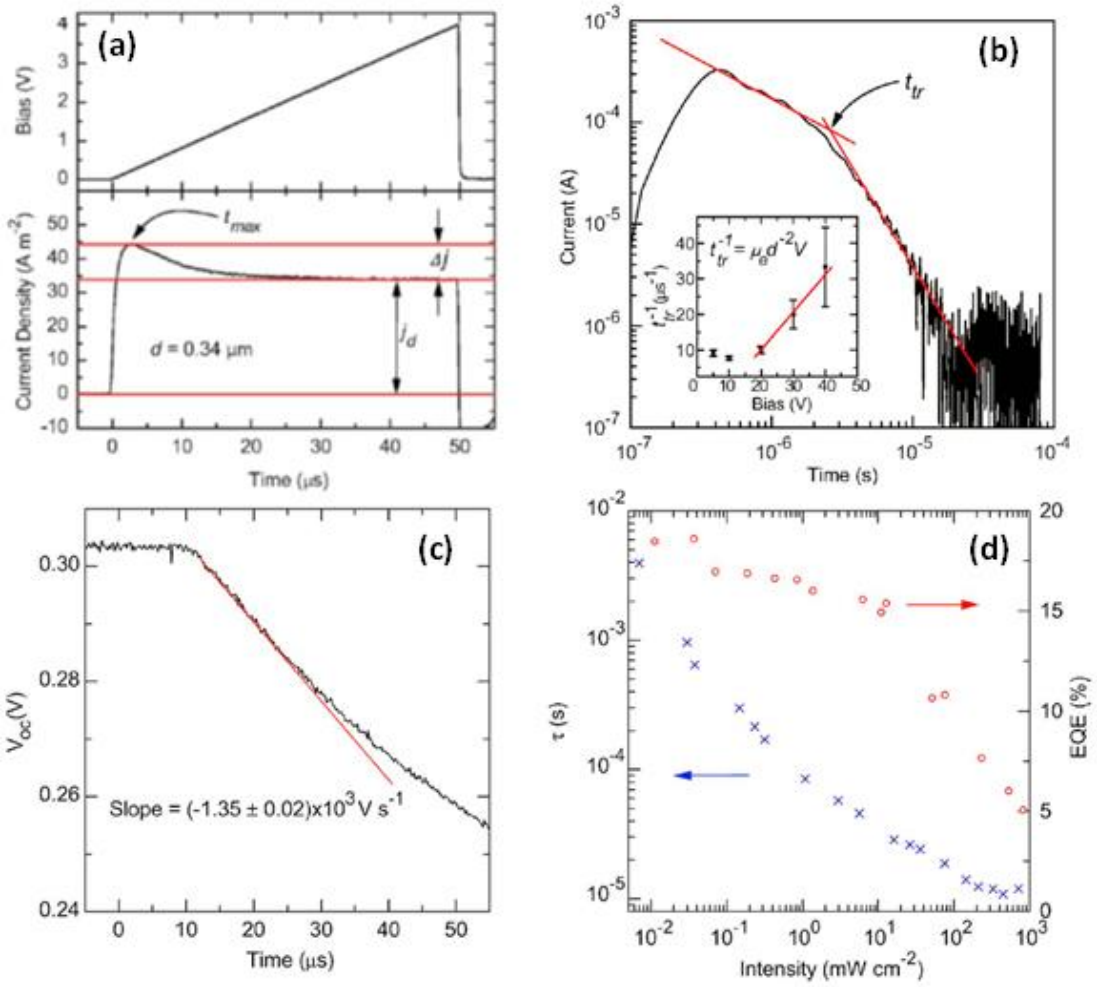

Figure 5-5. Current transient signals used to extract (a) the hole mobility (CELIV, 80000 V s^{-1} ramp rate) and (b) the electron mobility (time-of-flight, under 40 V bias). (c) V_{oc} decay signal (after 975 nm, 16 mW cm^{-2} illumination turn off) and a linear best fit (dashed red line) used to determine the recombination-llimited lifetime. (d) Lifetime (blue crosses, left axis) and EQE (red circles, right axis) and as a function of illumination intensity at 975 nm [163]

The time-of-flight transients were obtained by illuminating the ITO/PbS QD film/Al device with a 10 ns pulse at 532 nm using an yttrium aluminum garnet laser. To isolate the electron transport dynamics, devices were reverse biased. The obtained electron mobility in the fully depleted region was $(2 \pm 1) \times 10^{-4}$ cm^2 V^{-1} s^{-1}.[163] For the OCVD measurement, the ITO/PbS QD film/Al device was illuminated by a 975 nm diode laser, modulated using a digital pulse

generator, at room temperature. Immediately after turn off the laser, an initial slope of the decay (dV_{oc}/dt) is related to the lifetime (τ) by

$$\tau = -\frac{kT}{q}\frac{F_1}{\frac{dV_{oc}}{dt}} \quad (5\text{-}3)$$

where k is the Boltzman constant, T the temperature, q the elementary charge and F_1 ranges between 1 at low injection and 2 at high injection. Measured lifetime of PbS and PbSe QDs reveals that the lifetime increases steadily from ~ 10 μs at high light intensities to 1 ms at low light intensities.[163] The drift length of the carriers is given by $l_{diff} = \sqrt{\mu\tau kT/q}$. By calculation, at 12 mW cm^{-2}, the hole and electron drift length in ITO/PbS QD film/Al device is of 10 and 1 μm,[163] which are far longer than the depletion width (~ 150 nm).

Thus, the efficiency of the Schottky device depends on the balance between light absorption and carrier extraction. In the device with a thick photosensitizer layer, efficiency is limited by the rate of the carrier diffusion through the neutral region. Although thicker PbS QDs layer can absorb more photons for carrier generation, however, carriers have a higher recombination chance when transporting to the opposite contact. As a result, ~ 230 nm is the optimized thickness of PbS QDs film in the Schottky-type solar device.

5.1.3 Heterojunction Solar Cells Based on PbS QDs Film

By inserting another *n*-type semiconductor film with wide bandgap, such as TiO_2 and ZnO, between the PbS QDs and metal electrode, another planar heterojunction will be introduced into the Shottky solar device, if the metal electrode is substituted by high work function metal, like Au or Ag. This planar heterojunction will change the carrier transportation directions and a so-

called invert solar cell is established. In detail, electrons will transfer from the junction to TiO_2 nanocrystals along the conduction band and drill into the FTO substrate, and hole carriers will travel from the PbS layer to Au electrode following the valence band. To address the working mechanism of the QDs based solar cell, a comparison of the photovoltaic structures is shown in Figure 5-6.

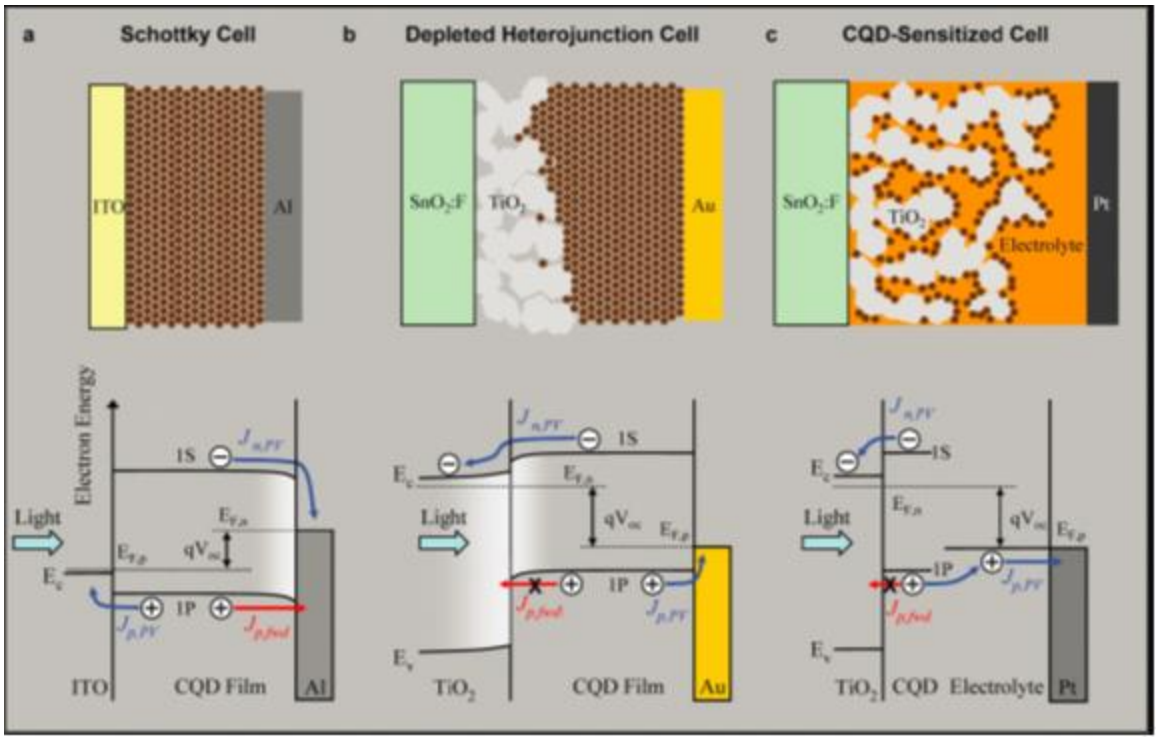

Figure 5-6. Comparison of three QDs based photovoltaic architectures under photovoltaic operation close to maximum V_{oc}. $E_{f,n}$ and $E_{f,p}$ are the electron and hole quasi-Fermi levels; E_c and E_v are the conduction and valence band edges; $J_{p,PV}$ and $J_{n,PV}$ are the hole and electron photocurrents (and are equal at steady state); $J_{p,fwd}$ is the hole current in the forward bias direction [159]

In the Schottky device (Fig. 5-6a), Schottky junction is the driving force for carrier separation, but leads to lower FF and V_{oc} for a given J_{sc}, due to the poor barrier for hole injection into the electron-extracting contact. For the inorganic QDs sensitized solar cell (Fig. 5-6c), which is very similar to the above mentioned dye sensitized solar cell, a thin layer of QDs

photosensitizer anchors on the surface of TiO_2 nanoparticles as the light absorber. The light absorbing capacity of this structure is low, resulting in a poor J_{sc}, but it provides good FF and V_{oc}. To combine the merits of these two devices, a depleted-heterojucntion (DH) structure is designed, leading to maximized FF, V_{oc}, as well as J_{sc} (Fig. 5-6b).

The DH structure is actually a kind of *p*-*n* junction. A depletion layer arises from the electron-accepting contact to the *p*-type PbS QDs film.[159] Under illumination, the photogenerated carriers in the depletion region will be swept by the built-in field to the edges of the depletion region in the junction. As shown in Fig. 5-7, photogenerated carriers and those produced in the quasi-neutral region, are required to diffuse across the quasi-neutral region to the collecting electrodes. Mid-gap state, which is known as recombination centers in the junction, provides undesired nonradiative pathways for the loss of charge carriers before their extraction. The shallow trap plays a much less harmful role and can extend the excited state lifetime by sacrificing the carrier mobility, in order to keep the product of carrier mobility and lifetime unchanged as compared to the trap-free case.[143] Considering that the metal contact in Schottky junction can also be seen as a heavily doped semiconductor, where a negligible depletion region on the metal side but the entire depletion region falls on the semiconductor side, Schottky contact is sometimes referred to as a single-sided *p*-*n* junction.

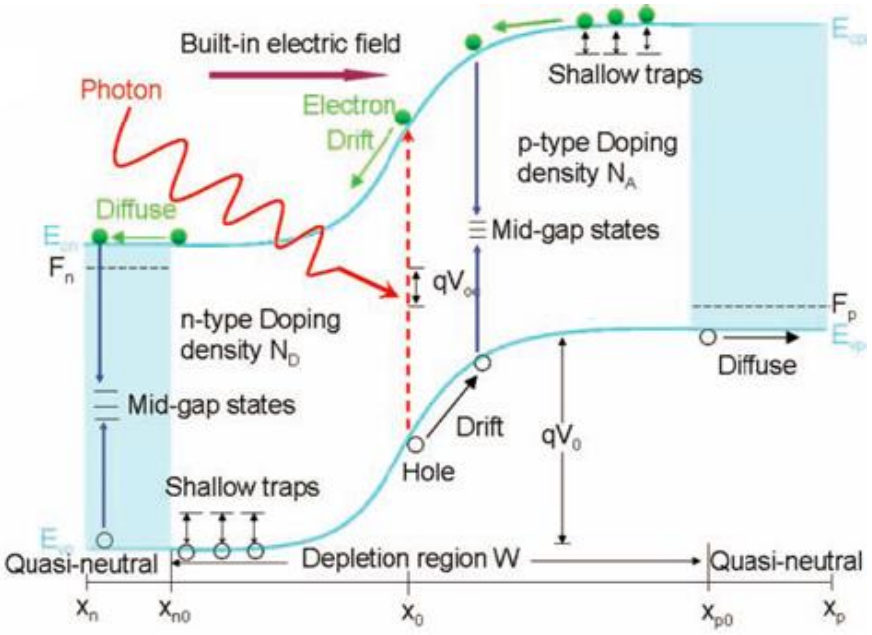

Figure 5-7. Schematic diagram of a *p*-*n* junction. qV_{oc} is the difference between the quasi-Fermi level F_n of electrons in the *n*-type material and quasi-Fermi level F_p of holes in the *p*-type material under illumination. Mid-gap states and shallow traps are present in both the *p*- and *n*-type materials [143]

Figure 5-8 shows the energy level of the TiO_2 and PbS QDs with various sizes. It indicates that as the QDs size grows, the first excitonic absorption shifts red and a wider solar spectrum will be covered, leading to an expected higher J_{sc}. But the as-narrowed bandgap of the QDs will cause continuous decrease of V_{oc}. A clear cross-section view of the device is shown in a TEM image (Fig. 5-8c) and each layer was characterized by the energy dispersive X-ray analysis.

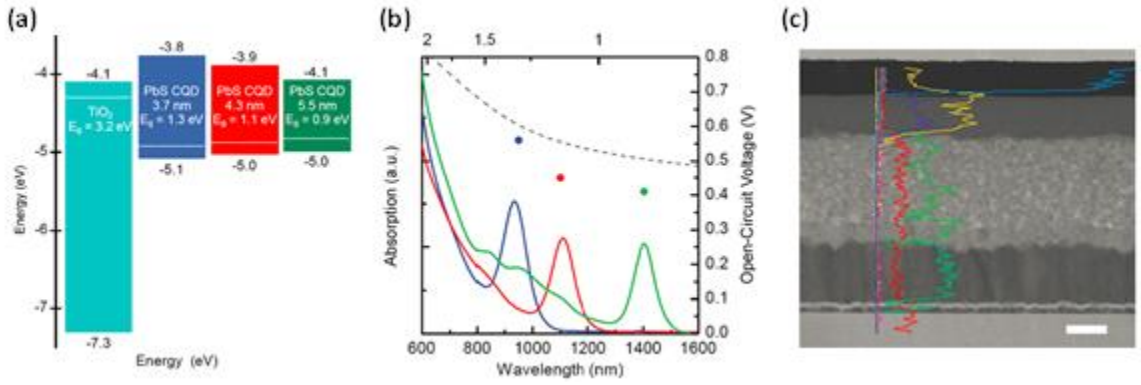

Figure 5-8. (a) Energy level alignment of TiO_2 and PbS QDs of different sizes. The Fermi level is shown as a dashed line. (b) Solution absorption spectra in toluene of the three different PbS QDs used in device fabrication. The experimental values of V_{oc} are shown above each excitonic peak, and the upper limit to V_{oc}, calculated from the difference in Fermi levels shown in panel (a) is drawn as a dashed line. (c) Cross-section TEM of a photovoltaic device. The sample was prepared by focused-ion-beam milling. The line plot shows the elemental distribution as determined by energy-dispersive X-ray analysis (yellow, S; blue, Pb; green, Ti; cyan, Sn; red, O; light blue, Au). Scale bar is 200 nm[159]

5.1.4 X-ray Photoelectron Spectroscopy

X-ray photoelectron spectroscopy (XPS) is a quantitative surface chemical analysis technique, which requires an ultra-high vacuum condition. The XPS spectra are collected by irradiating the target material with monochromatic Al-Kα X-rays (1000 ~ 2000 eV) while probing the kinetic energy and number of electrons escaped from the outer surface (1 ~ 10 nm) of the material. Thus, ion beam etching is needed sometimes to clean off the surface contamination or oxidation of the sample. Schematics of the XPS process is shown in Figure 5-9. Since the energy of an X-ray with a certain wavelength is known, the electron binding energy of the emitted electron is expressed as:

$$E_{binding} = E_{photon} - (E_{kinetic} + \emptyset) \quad (5\text{-}4)$$

where ϕ is the work function of the spectrometer. A typical XPS spectrum usually includes several peaks at characteristic binding energy values. Each peak is a fingerprint of a particular electron configuration in the atom. The number of electrons of a specific chemical specie is proportional to the area under an individual peak. Thus, the chemical species and atomic percentages can be determined by fitting the XPS spectrum. For example, O 1s singlet is used for peak fitting of air annealed PbS film (Fig. 5-9b). From the oxygen percentage of each oxide species, the molar ratio of the oxides ($n_{PbO} : n_{PbSO3} : n_{PbSO4}$) is 1.0:0.84:1.06.

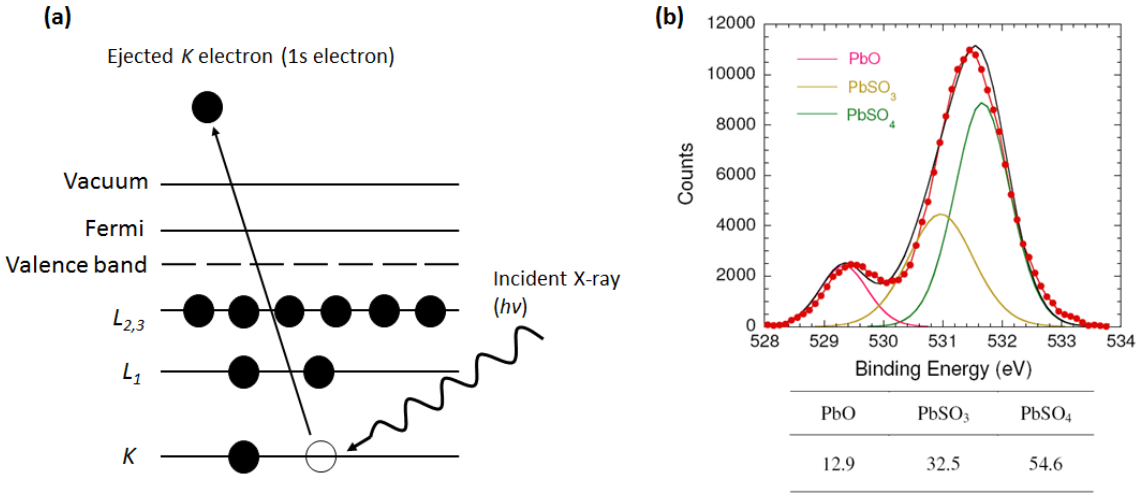

Figure 5-9. (a) Schematics of XPS process of 1s signal.[190] (b) Fitting of O 1s spectra for air annealed PbS film with chemical species and corresponding atomic percentages [169]

5.2 Dual Effects of Surface Plasmonic Particles in PbS/TiO_2 Heterojunction Solar Cells

5.2.1 Experiment

Materials. Tetra ethoxy silane (TEOS, 98%), ammonium hydroxide (28%~30%), (3-aminopropyl)trimethoxysilane (APTMS, 97%), tetrachloroauric acid ($HAuCl_4 \cdot 3H_2O$), tetrakis

hydroxymethyl phosphonium chloride (THPC), sodium hydroxide (NaOH), potassium carbonate (K_2CO_3), polyvinylpyridine (PVP, MW = 40,000), Lead oxide (PbO), oleic acid (OA), octadecene (ODE), hexamethyldisilathiane (TMS), 1,2-ethanedithiol (EDT), hexane (anhydrous), and acetonitrile (anhydrous) were all purchased form Aldrich and used as received. Ethanol (200 proof, anhydrous) was bought from Decon Laboratories Inc. and formaldehyde (36.5%~38%) from EMD Millipore and methanol (99.8%) from J. T. Baker. Ultrapure water (18.2 MΩ resistivity) was deionized from MIlli-Q purification system (Millipore, MA)

Synthesis of PbS Colloidal Quantum Dots. PbS QDs with excitonic peak at 740 nm were prepared via a similar procedure as Hines and Scholes[144] demonstrated. All the reactions were carried out using standard Schlenk line system. Typically, the lead oleate precursor was formed by heating and firmly stirring the mixture, containing 90 mg of PbO, 0.25 ml of OA and 3.75 ml of ODE, in a 50 ml three-necked flask at 150 ^oC for 30 min under Ar gas protection. When cool down this precursor solution to 120 ^oC, 42 μL of TMS in 2 ml ODE was swiftly injected into it with a sudden drop of the reaction temperature to 100 ^oC. Keep the reaction temperature at 100 ^oC for 30 sec, and then remove the heating mantle to let the solution cool down to room temperature. PbS QDs were purified by repeated precipitation with acetone and dispersion with toluene and finally dispersed in hexane.

Synthesis of SiO_2@Au@SiO_2 core-shell-shell spheres (SGSs). As shown in Figure 5-10, the SGSs were synthesized following a developed procedure similar to those recorded in the literatures.[33, 34, 191] Typically, initial uniform SiO_2 spheres with an average diameter of 90 nm were prepared via Stöber method.[114] A mixture of 50 ml silica/ethanol solution (c = 1g/L) and 20 μL APTMS was stirred firmly at room temperature for 12 hrs and then refluxed for 1 hr, in order to functionalize the surface of silica spheres with organosilane molecules (APTMS). The

functionalized silica spheres were centrifuged and redispersed in pure ethanol several times to remove the excess APTMS. Aqueous solution of tiny gold nanoparticles with a diameter of ~2 nm were prepared via Duff's method,[192] and further diluted to 100 ml. The as formed silica/ethanol solution was concentrated to 25 ml, and drop by drop added to this rapidly stirred gold aqueous solution. After stirring for 12 hrs at room temperature, non-attached gold nanoparticles were removed by centrifugation, leaving behind silica spheres decorated with gold nanoparticles through the gold-amine interactions. These attached gold seeds played the role of nucleation sites for further gold shell growth.

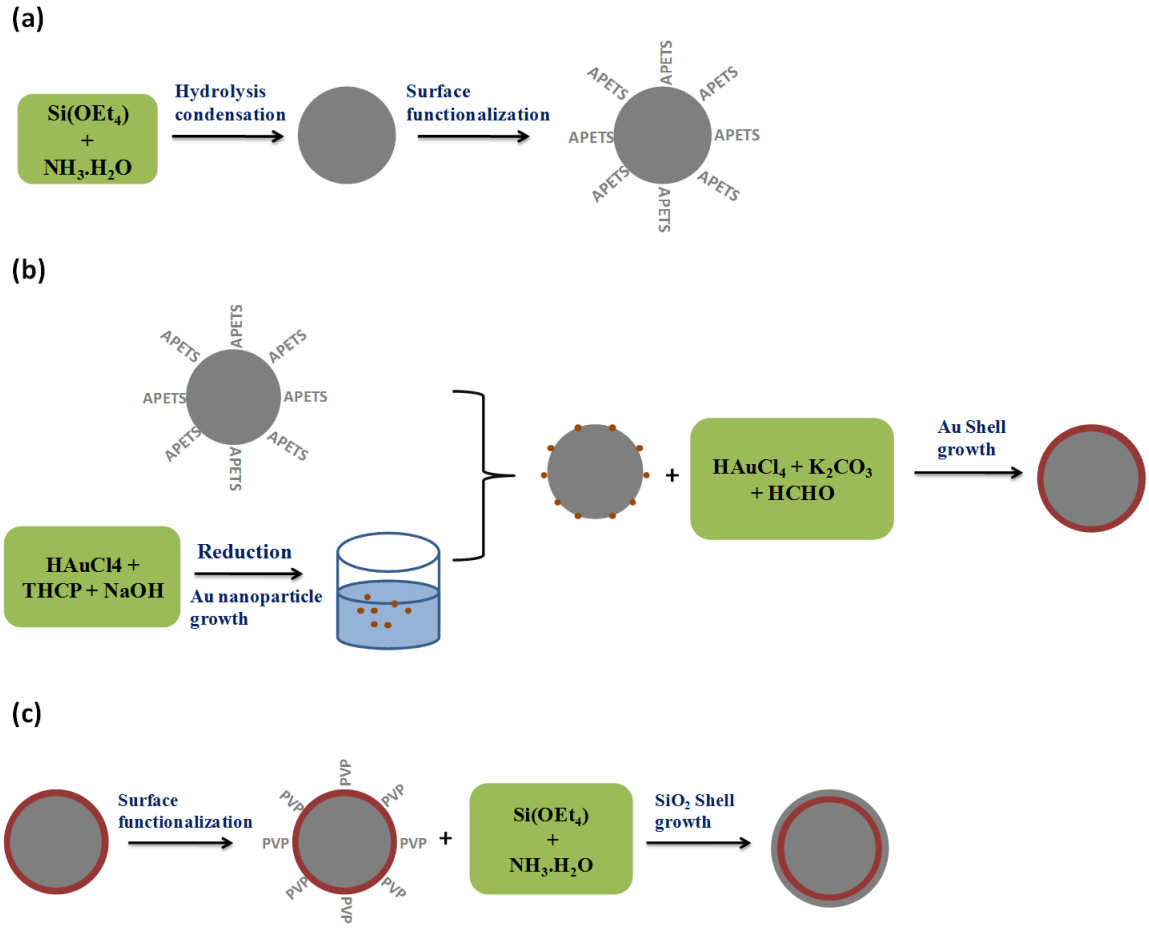

Figure 5-10. Seed mediated procedure of SiO_2@Au@SiO_2 particle fabrication, which includes three steps of (a) SiO_2 core, (b) Au@SiO_2 and (c) SiO_2@Au@SiO_2 preparation

Au plating solution was prepared by adding 17.1 mg (25 mM) $HAuCl_4 \cdot 3H_2O$ and 124.5 mg (1.8 mM) of K_2CO_3 into 100 ml deionized water, and after aging 2 days, seeded silica aqueous solution was dropped in it with vigorous stirring at room temperature. The $AuCl^-$ ions reduction started after 200 μL of formaldehyde was added to the mixture, and complete gold nanoshell with a thickness of 20 nm was formed within 20 min. In order to coat another silica shell out of the $Au@SiO_2$ particles (GSs), no purification was needed to the pristine GSs aqueous solution, and 10 ml of 0.5 mM PVP aqueous solution was immediately added once the GSs were formed. After stirring for another 24 hrs, the PVP stabilized GSs were centrifuged and purified in deionized water and ethanol several times. Resulting particles were redispersed in 194 ml of pure ethanol, with subsequently adding 8.5 ml of ammonium hydroxide and 0.9 ml of TEOS solution (10 vol% in pure ethanol). This mixture was then stirred for 12 hrs at room temperature to form SGSs. Final product was washed by pure ethanol and restored in methol.

Device Fabrication. Patterned fluorine-doped tin oxide (FTO) (Pilington TEC 8) coated glass substrates were cleaned by merging in ethanol/acetone (1:1) mixture under sonication for 10 min. TiO_2 sol made of TTIP acidic solution was spin coated on the precleaned FTO and subsequently annealed in O_2 at 500 ^oC for 2 hrs, resulting in a 80 nm hole blocking layer. Then TiO_2 paste, composed of TiO_2 nanoparticles with a diameter of ~ 20 nm and prepared via a hydrothermal reaction, was printed on the blocking layer by a doctor blading method. After annealing at 450 ^oC for 30 min under N_2 gas protection, a second TiO_2 film formed with a thickness of ~ 1 μm. In order to build a planar heterojunction for carrier separation, on top of this TiO_2 mesoporous film, PbS QD film was prepared by a layer-by-layer dip coating method in an Ar gas filled glove box. Typically, the substrate with TiO_2 film was merged into PbS QDs/hexane solution (20 mg/ml) by hand, and after 5 sec, slowly dragged out of the solution at a

velocity of ~0.2 cm s^{-1}. Subsequently, it was re-dipped into 0.1 M EDT/acetonitrile for 10 sec and quickly removed. This dipping procedure was repeated 14 times, resulting in a 150 nm close packed PbS film. In order to locate the SGSs on top of the PbS film or inside of the film, a monolayer of SGSs, which covers ~ 20 % area of the substrate, was drop coated in the device after and before the PbS deposition separately from a diluted SGSs/methanol solution, and loosely attached particles were then washed away by methanol after solvent evaporated naturally. Similarly, SiO_2 spheres, whose average diameter is of 150 nm and prepared by the Stöber method as well, were drop coated on the TiO_2 film as a control sample. Finally, 20 nm thick gold layer was deposited onto the PbS film by electron beam evaporation as the top electrode. Each device has an active area of 0.04 cm^2.

PbS QDs, PbS film, GSs and SGSs Characterization. The morphologies of the GSs, SGSs, PbS QDs and cross-section view of the Au/PbS/TiO_2 films were tested by high-resolution electron microscopy (HRTEM, JEOL JEM-2100F). The Z-contrast high angle annular dark field (HADDF) cross-section images of the films were tested in STEM mode. And the element distribution was studied with EDS mapping. The PbS QD sample was prepared on a Cu grid, with a post ligand exchange in 0.1 M EDT/acetonitrile solution for 10 sec. The film sample was deposited on silicon substrate and prepared by mechanical polishing and ion milling. The optical properties of the GSs, SGSs, PbS QDs and PbS film were investigated with the UV-vis spectrophotometer (Lambda 35, Perkin Elmer) attached to an integrating sphere ranging from 300 nm to 1100 nm. X-ray photoelectron spectra (XPS) were collected with monochromatic Al-Kα X-rays (1487 eV) at 150W power on a custom built multi-technique surface analysis instrument. In order to increase the accuracy and sensitivity of the analysis, surface contamination or oxidation of the PbS films were cleaned off by ion beam etching before signal

collection. Data analysis was carried out using an open source XPSPEAK41 for background subtraction and peak fitting. Large scale morphologies of GSs and SGSs, as well as a monolayer of SGSs that covers ~ 20 % area of the substrate were examined using scanning electron microscopy (SEM, Philips XL 30). In particular, energy dispersive X-ray spectroscopy was applied with SEM for elemental analysis.

Device characterization. *J-V* curves were measured under AM 1.5 G simulated sunlight (PV Measurements, Inc) with the aid of the electrochemical workstation (CH Instruments, CHI 660C). The electrochemical impedance spectroscopy (EIS) measurement was performed ranging from 0.1 Hz to 1 kHz with the maximum electric potential of 0.05 V, and the external bias with a magnitude of open circuit voltage was applied. Incident photon to current efficiency curves (IPCE) of the solar cell was measured by illuminating the sample with a monochromatic beam (Newport Corp.). Electron lifetime was checked by an open-circuit voltage decay (OCVD) technique,[107] in which the light source was a laser diode (λ= 660 nm) driven by a function generator (Agilent 33220A) to provide square wave modulated illumination, and the changes in the photovoltage was monitored by a digital oscilloscope (Tektronix, TDS2024B).

5.2.2 Results and Discussions

The output voltage of the QD solar cells depends on the band gap of the PbS QDs which is a function of a nanoparticle size.[159] In this study, we chose PbS QDs with a diameter of 3.0 ± 0.4 nm and a band gap of 1.67 eV to achieve an open circuit voltage of ~0.65V in the device.

PbS QDs capped with an oleic ligand were synthesized using the well-known procedures developed by Hines and Scholes[144]. Figure 5-11a shows the absorbance spectra of the PbS QDs dispersed in hexane, in which the first excitonic absorption peak was located at 740 nm. The low

absorption position corresponds to a wide band gap of 1.67 eV. Figure 5-11b,c show the transmission electron microscopy (TEM) and high-resolution transmission electron microscope (HRTEM) images of the PbS QDs. From the TEM image, the diameter of the QDs was counted as 3.0 ± 0.4 nm with a narrow size distribution.

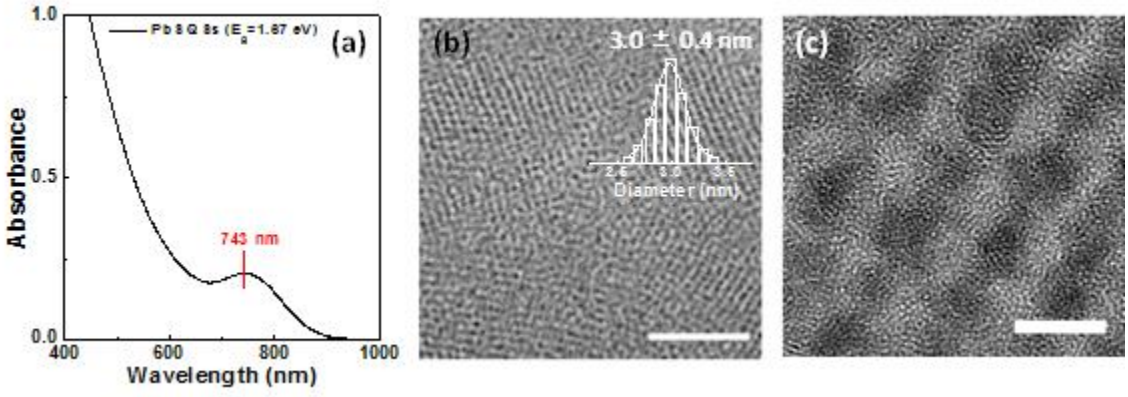

Figure 5-11. (a) Absorbance spectra of PbS QDs with two different sizes in hexane. (b) Large scale TEM image of PbS QDs on a Cu grid. The size distribution of the PbS QDs was counted as 3.0 ± 0.4 nm. Insert scale is 50 nm. (c) HRTEM image of the PbS QDs. Insert scale is 5 nm.

The energy band level of the PbS QDs can be calculated from the Cyclic Voltage scan with the aid of the electrochemical workstation. Figure 5-12a shows the voltammetry result for the PbS QDs whose optical band gap is 1.67 eV. The slope of the CV curve reveals the oxidation onset of the QDs is 0.5 eV. Considering the absolute energy for the reference electrode ($Ag/AgNO_3$) is 4.7 eV, the valence band edge of the QDs is of -5.2 eV. The corresponded conduction band edge of the QDs is then calculated to be -3.5 eV. Thus, energy band structures of the TiO_2 nanoparticles and PbS QDs are shown in Figure 5-12b.

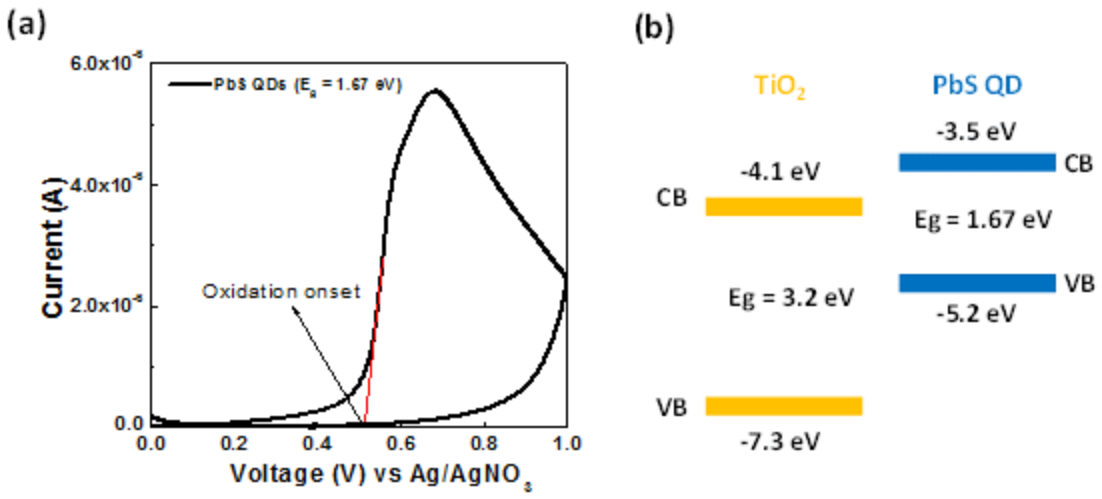

Figure 5-12. (a) Cyclic voltammogram results for PbS QDs with an optical band gap of 1.67 eV. The oxidation onset of the QDs is 0.5 eV. (b) The band gap structures of TiO_2 NPs and PbS QDs

Figure 5-13a shows the PbS film deposited on silicon substrate via a layer-by-layer dipping method. During each dipping cycle, a long oleic capping chain on the QDs is exchanged with a short thiol ligand 1,2-ethanedithiol (EDT) to reduce a distance between adjacent QDs and increase the electric conductivity of the PbS film. Typically, after a 12 cycle deposition, the thickness of the PbS film is around 150 nm. In order to verify the appearance of EDT molecules after ligand exchange, the chemical composition of the PbS film (QD E_g = 1.67 eV) was investigated using X-ray photoelectron spectroscopy (XPS) (Fig. 5-13b). Once loaded in the XPS chamber, the surface of the PbS film was cleaned by ion beam etching. The chemical species and corresponding atomic percentages of S 2p doublets applied for peak fitting can be derived from the literature[169]

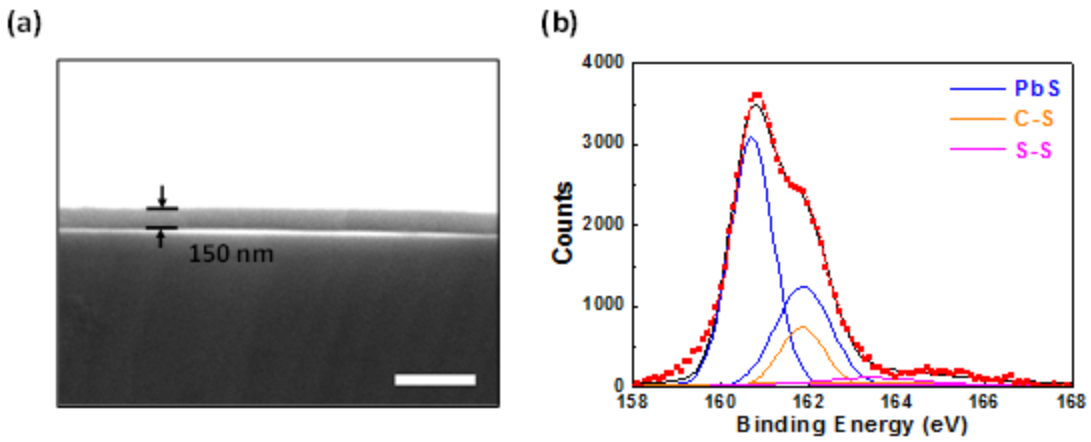

Figure 5-13. (a) PbS QDs film deposited on silicon substrate via a layer-by-layer dipping method. The thickness of the film is around 150 nm. Insert scale bar is 500 nm. (b) XPS spectra of S 2p peaks in PbS film. S 2p doublet with an intensity ratio of 2:1 and splitting of 1.18 eV is applied for sulfur species fitting. The binding energies are 160.7 eV and 161.88 eV for PbS, 161.85 eV and 163.03 eV for C-S, 163.43 eV and 164.61 eV for S-S

High-resolution transmission electron microscopy (HRTEM) was employed to examine the microstructure of the solar cell film (QD E_g = 1.67 eV). In the bright field cross-section images (Figure 5-14a) and dark field cross-section images (Figure 5-14b), a boundary between the TiO_2 and PbS films locates at 150 nm from the PbS/Au interface, and a plain heterojunction is formed with little interpenetration. X-ray photoelectron spectroscopy (EDS) mapping of the film cross-section is shown in Fig. 5-14c, in which a rectangular area in the HADDF cross section image was chosen for elemental distribution scanning. Elements S and Ti are traced in the selected area. The element mapping verifies the presence of TiO_2 and PbS layers, and a clear boundary at the interface indicates nearly no PbS diffusion is detected in the TiO_2 film.

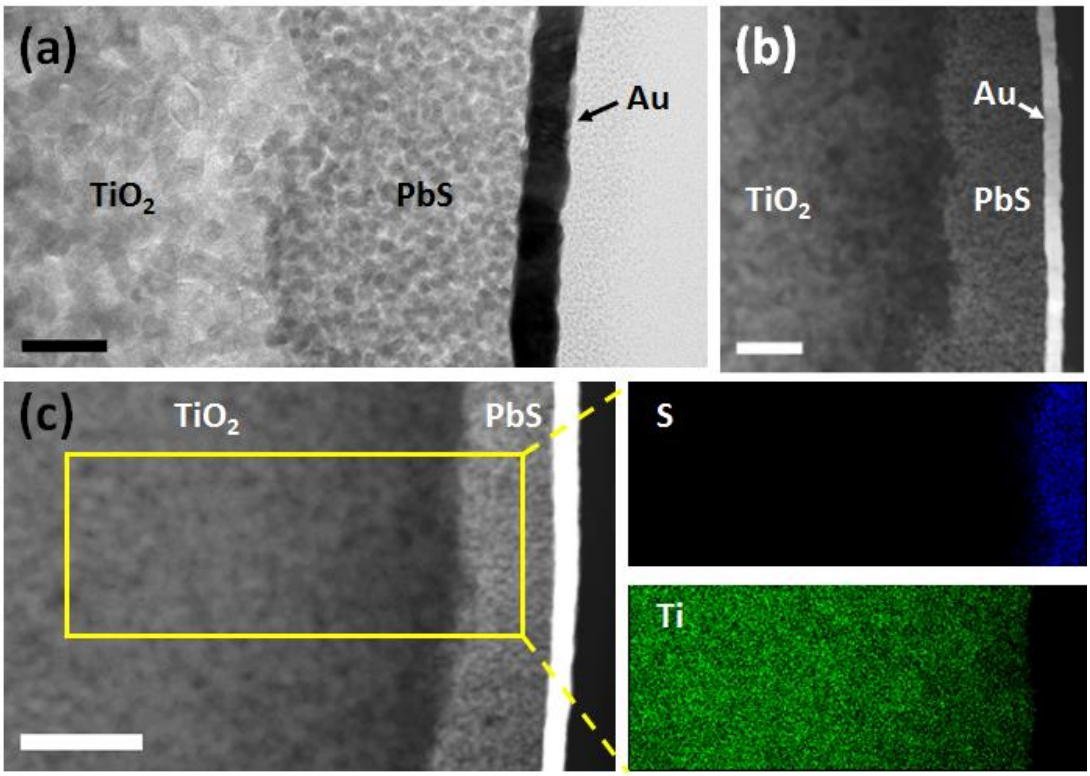

Figure 5-14. (a) A bright field HRTEM cross-section image of the device. The scale bar is 50 nm. (b) Z-contrast high angle annular dark field (HADDF) cross-section image of the sample. The scale bar is 100 nm. The insert red bar shows the width of the overlapped TiO_2 nanoparticles and PbS QDs at the interface. (c) HADDF image and EDS mapping of the film cross-section. The scale bar is 200 nm

SGS spheres were prepared using the seeded metallization of silica spheres.[34, 193] Au seeds (~2 nm in diameter), which work as nucleation sites, are decorated on the surface of (3-aminopropyl) trimethoxysilane (APTMS) functionalized silica cores. Then $AuCl^-$ ions are gradually reduced from an electroless plating solution to form a complete Au shell on the silica sphere. After the polyvinylpyridine (PVP) stabilized $Au@SiO_2$ (GS) particles are prepared, a continuous silica passivation shell is formed on top of the Au shell.[191] A top silica capping layer enhances the chemical stability of the plasmonic spheres and prohibits carrier trapping by the Au shell.

Based on preliminary results, SGSs which consist of a silica core with 90 nm diameter, 20 nm gold intermediate layer, and 7 nm outer silica shell were chosen as the plasmon contributor, since they exhibit increased light absorption and scattering at 600 nm ~ 1000 nm where PbS QDs with a bandgap of 1.67 eV need field-enhancement effect for better light harvesting. The outer silica shell was thinner than 10 nm to minimize a change in the near-field intensity at the outer silica shell.[194] The large scale morphologies of the GSs and SGSs were tested by SEM (Figure 5-15a,b). It indicates that the GSs and SGSs are uniform sub-microspheres with a diameter of 130 ± 10 nm and 144 ± 10 nm, respectively. In order to investigate the component of the spheres, EDS test was applied to detect the elemental information on the whole area as that shown in the SEM image. In particular, Figure 5-15c shows the element analysis of GSs, where strong Au peak corresponds to the Au nanoshells, and Si and O peaks are related to the inner silica cores. Otherwise, Figure 5-16d shows the result for SGSs, in which the signals of Si and O are enhanced comparatively, due to another outer silica shell coating.

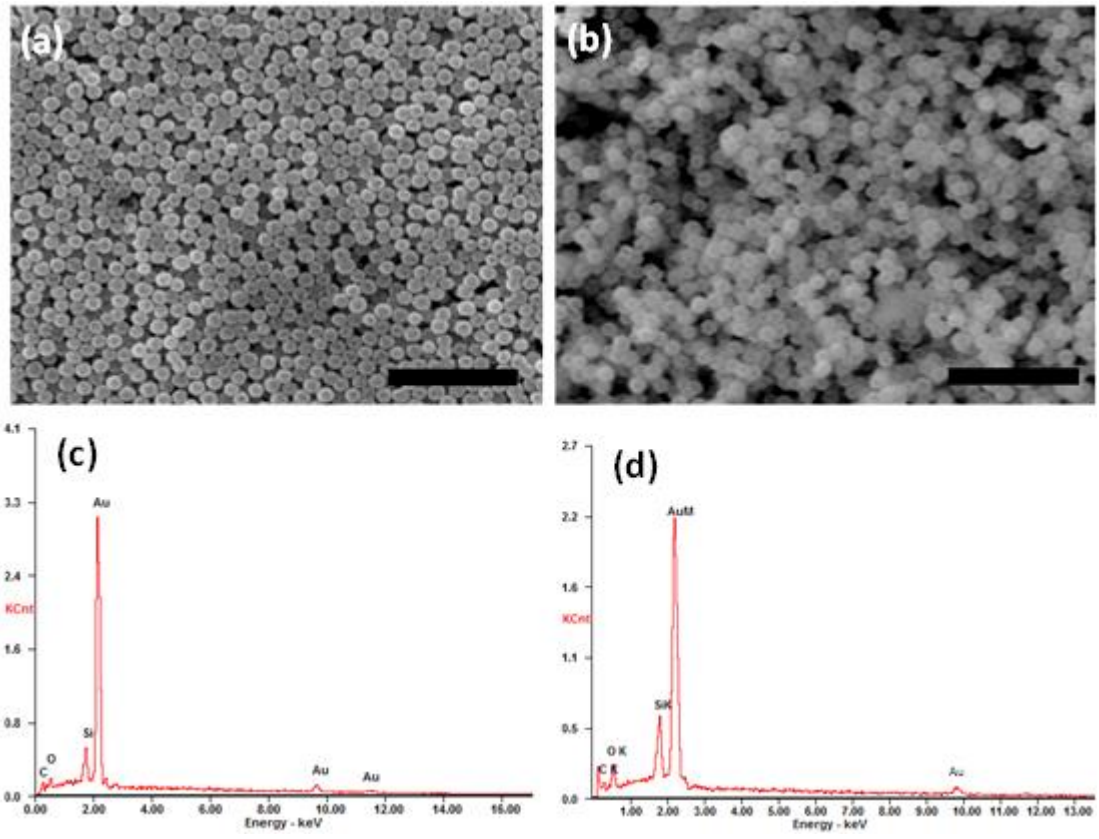

Figure 5-15. (a) Large scale SEM images of GSs, with (c) elemental analysis on the same whole area by EDS. (b) Large scale SEM images of SGSs, with (b) relevant EDS test on the same whole area. Inset scale bar is 1 μm

Figure 5-16a-c shows transmission electron microscopy (TEM) images of the morphology evolution of these SGSs from bare silica spheres (~90 nm in diameter) to final core-shell-shell particles. Typically, the Au shell is ~ 20 nm thick and outer silica shell is ~7 nm. The high resolution TEM (HRTEM) image in Figure 1d shows a d-spacing between atomic layers of 2.35Å which corresponds to the (111) plane of Au. The thin outer silica shell is designed to separate direct contact between Au shell and PbS QDs in the device, in order to prohibit carrier trapping and recombination at the Au shell. The optical properties of GSs and SGSs were measured by UV-vis spectrometer (Fig. 5-16e). Their main plasmon peaks locate at 660 nm and 680 nm, respectively. The red-shift of the plasmon peak from GS to SGS is due to a slight

change in a dielectric constant of media after the outer silica shell was coated. Compared to water or air, silica has a higher dielectric constant, which decreases the plamonic frequency of embedded metallic nanostructures.

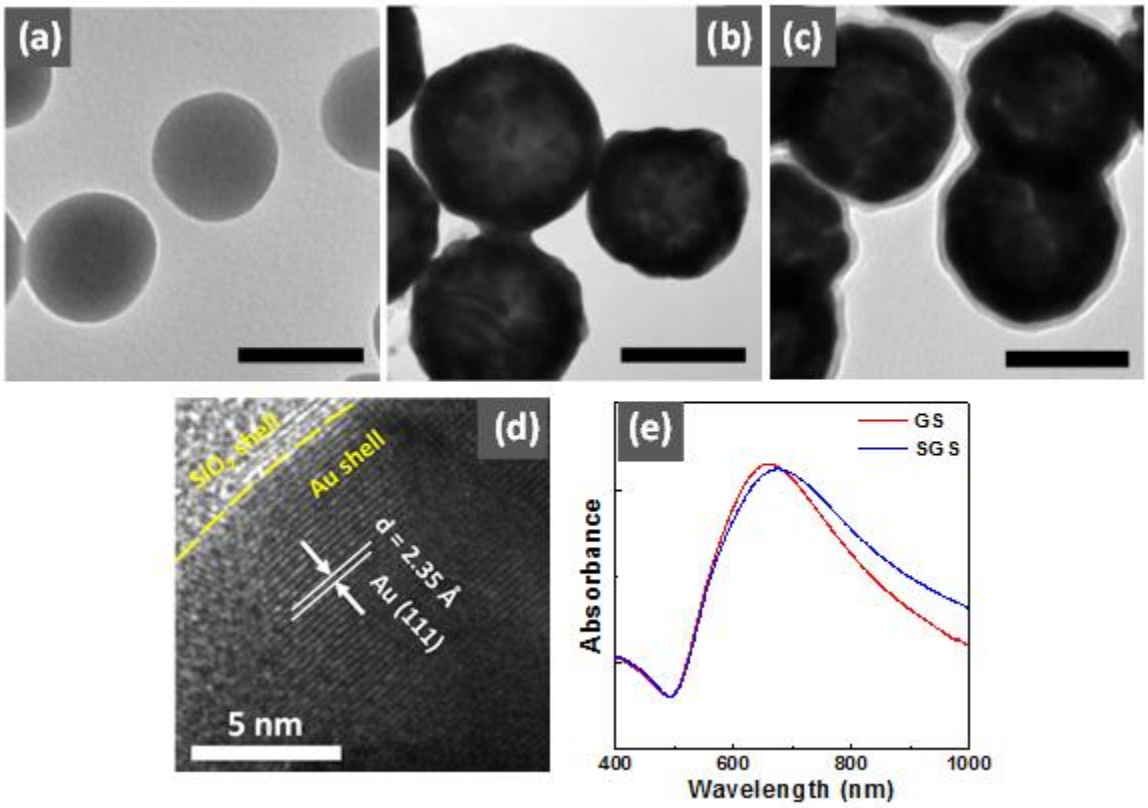

Figure 5-16. Morphology evolution of the SGSs. (a) bare silica spheres with a diameter of ~ 90 nm. (b) Au@SiO_2 core-shell particles with an Au shell of ~20 nm thick. (c) SGSs with another outer silica shell of ~7 nm thick. Insert scale bar in (a-c) is 100 nm. (d) The HRTEM of the Au nanoshell. The d-spacing of 2.35 Å corresponds to the (111) plane of Au. (e) Absorbance spectra of GSs and SGSs dispersed in deionized water

Figure 5-17 shows the schematics of the device structures. A controlled solar cell without the plasmonic particles consists of four layers deposited on FTO coated glass substrate: 80 nm thick TiO_2 hole blocking layer, 1 μm thick TiO_2 mesoporous film, 150 nm thick PbS QDs film and 20 nm thick Au electrode. In principle, PbS film acts as light absorber and hole

transportation layer, and TiO_2 film works as the electron transportation layer. The energy level diagram of the device is illustrated in Figure 5-17e. The electron is injected from the conduction band of PbS QDs to that of TiO_2 and moves to FTO, and the hole path is formed from the valance band of PbS QDs to the valence band of Au anode. A built-in potential at the TiO_2/PbS interface promotes electron-hole separation and carrier injection.

To investigate the dual effect of the plasmonic particles on the performance of thin film solar cells, plasmonic SGSs are added into the devices in two different ways (Figure 5-17b,c). One is to coat a monolayer of SGSs on top of the PbS film via a dip coating before Au electrode deposition, and the other is to place the SGSs on TiO_2 film first and coat the PbS film on SGS decorated TiO_2 film. In the latter case, SGSs covers 20% of FTO surface. Figure 5-17f shows the distribution of SGSs on the substrate before the dip coating of PbS QDs. SGSs cover 20% of the surface area and an average distance between adjacent SGSs is about 400 nm. These two different structures are expected to manage incoming light differently. SGSs on the top of the PbS QD film are intended couple LSPRs with photons after light passes through PbS film. An advantage of this design is to minimize energy dissipation at the Au shell, since photons hit PbS film first. On the other hand, SGSs between the PbS film and TiO_2 film cause a dual effect. In this configuration, SGSs at the bottom increases the near-field intensity and nanodomes formed on the top Au layer induce additional light scattering and near-field enhancement effects.

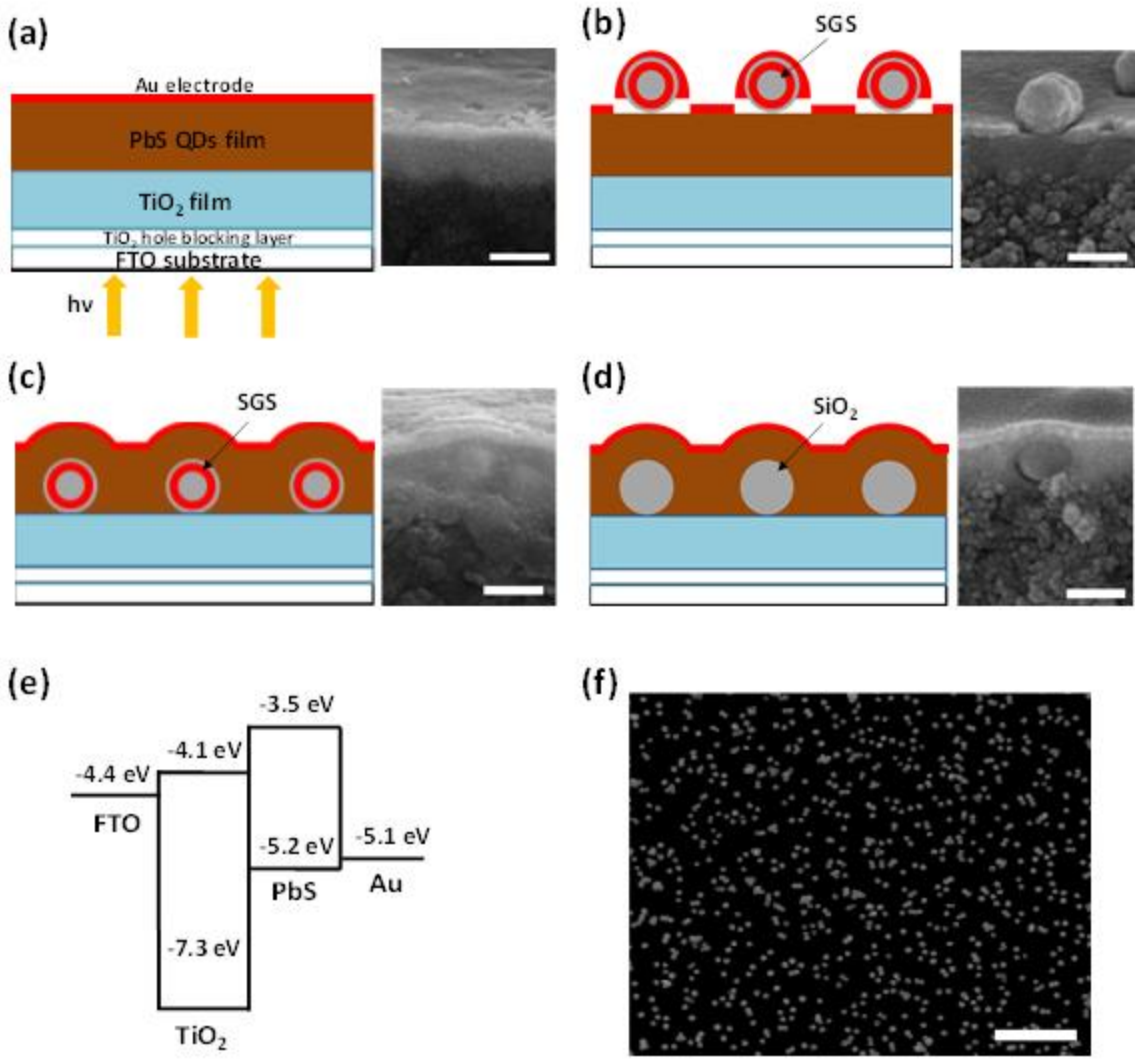

Figure 5-17. Device architectures with cross-section view of the SEM images. (a) Standard sample without SGSs, (b) device with SGSs embedded between the PbS film and Au anode (SGS on top), (c) SGSs merged in PbS film (SGS inside) and (d) SiO_2 spheres merged in PbS film (SiO_2 inside). The insert scale bar is 200 nm. (e) Energy level diagram of the standard device. (f) SEM image of a monolayer of SGSs prepared by spin coating and covering the surface area of a substrate by ~ 20 %. Scale bar is 2 μm

A theoretical simulation predicts that the second nanodome effect facilitates additional light absorption in the wavelength range of 500 nm ~ 800 nm.[174] Though this geometry causes small light absorption in a front end of the device, the plasmonic particles and nanodomes

located at both interfaces of PbS films may compensate light loss and creates a synergistic effect. In order to investigate a pure effect of the nanodomes on the top surface of Au electrode, bare silica spheres with an average diameter of 150 nm were added to the device, as shown in Figure 5-17d. In addition, the cross-sectional SEM image of each device confirms its schematic structure. Extra SEM images of the nanodome structures in the SGS_inside device is shown in Figure 5-18.

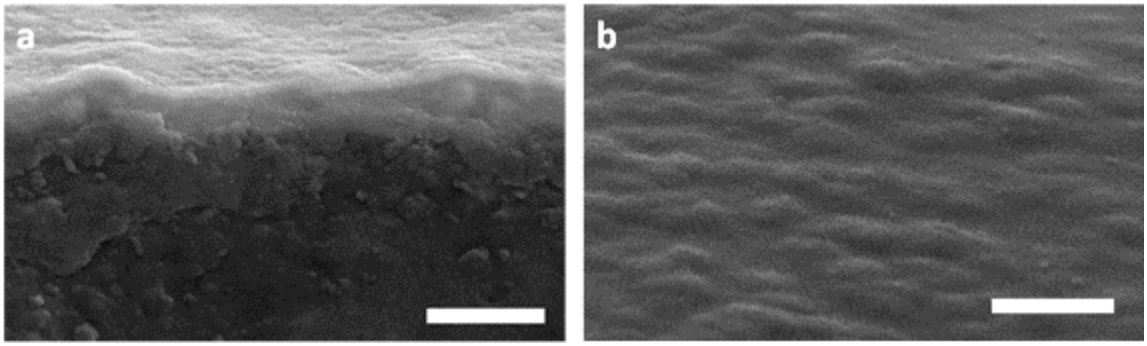

Figure 5-18. Cross-section view and top view of the SGS_inside device. The scale bar is 500 nm

The performance of the photovoltaic devices were tested under AM 1.5 condition. Current-voltage (*J-V*) characteristics of solar cells with four structures are shown in Figure 5-19a, and performance parameters of the solar cells are summarized in Table 5-1. Addition of the SGSs to the top of PbS film increased the short circuit current (J_{sc}) from 12.52 mA cm^{-2} to 15.10 mA cm^{-2}. When the SGSs were placed between PbS film and TiO_2 film, a further enhancement was observed and J_{sc} was as high as 16.15 mA cm^{-2}, giving a 29% improvement over the control device. Consequently, power conversion efficiency (PCE) increased from 3.09 % (without SGSs) to 3.83 % (SGSs inside PbS film), and an enhancement of 24% was achieved. To elucidate the physics underlying the enhancement of the photocurrent by SGSs, incident photon-to-electron conversion efficiency (IPCE) and UV-Vis absorption spectra of the different solar cells were analyzed. Figure 5-19b shows the IPCE spectra of control devices and plasmonic assisted

devices. SGSs on top of the PbS film promote photon-to-electron conversion in the red and near IR regions. A positive effect of the surface plasmons on the IPCE in a broad range is consistent with the result of the theoretical study demonstrating that SGSs intensify the near-field at wavelengths longer than 600 nm. Compared with the previous case, the insertion of SGSs between PbS film and TiO_2 film increases IPCE more in wavelength range of 600 nm to 750 nm. The device containing only bare SiO_2 particles exhibits an increase in IPCE mainly at the wavelength ranging from 600 nm to 750 nm. Since only nanodomes influence the photo-electron conversion in the solar cell embedded with bare SiO_2 particles, the additional enhancement of IPCE at 600 – 750 nm in the case of SGS inside is attributed to the increase in the near-field intensity and light scattering by the nanodomes of Au electrode.

A relative ratio of the change in IPCE spectra over the control solar cell is plotted in Figure 5-19c. IPCE values at 600 nm - 1000 nm are higher for plasmonic solar cells than for bare solar cells. Light absorbance spectra of the multilayer films are shown in Figure 5-19d. The light absorption at 600 nm - 1000 nm by SGSs matches well with the improved light harvesting ranges in the IPCE spectra. This indicates that overlap of absorption spectra of PbS QDs and SGSs improve light absorption in the visible and near-IR regime. A slight redshift of the absorption peak in the PbS/SGS/TiO_2 structure is due to a high refractive index of the PbS matrix.

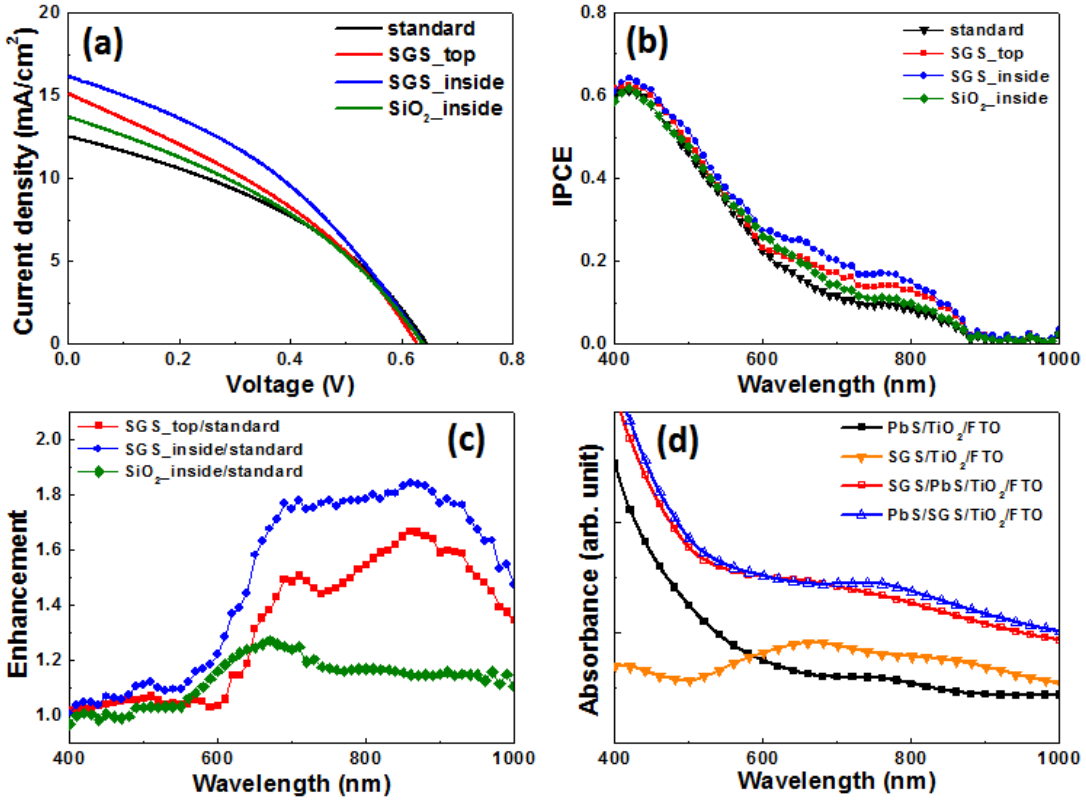

Figure 5-19. (a) *J-V* curve and (b) IPCE spectra of the devices including standard sample without SGS, SGS on top, SGS inside and SiO_2 spheres inside. (c) IPCE enhancement spectra. i.e. (IPCE of device with SGS on top/IPCE of the standard device). (d) Absorbance spectra of various tandem films: PbS/TiO_2/FTO, SGS/TiO_2/FTO, SGS/PbS/TiO_2/FTO, and PbS/SGS/TiO_2/FTO

Table 5-1. Response of FTO/TiO_2/PbS/Au photovoltaic devices with and without SGSs under Simulated AM 1.5 (100 mW/cm^2)[a]

Device Description	J_{sc} (mA/cm^2)	V_{oc} (V)	FF (%)	η (%)	R_{SH} (Ωcm^2)
FTO/TiO_2/PbS/Au (standard)	12.52	0.65	38.16	3.09	112.3
(SGS on top)	15.10	0.63	34.83	3.30	71.8
(SGS inside)	16.15	0.64	37.04	3.83	93.9
(SiO_2 inside)	13.71	0.64	35.90	3.15	85.4

[a]**The shunt resistance (R_{SH}) is calculated from $\partial V/\partial J$ at -0.1-0 V in *J-V* curve of the devices.**

SGSs improve IPCE of the solar cells via multiple different mechanisms. First, an increase in the photocurrent by SGS is due to plasmonic near-field coupling by LSPRs, which decays concentrically from the outer surface of SGSs. A coupling of plasmon with incident light generates a strong local electromagnetic field which stores the incident energy and facilitates light absorption by the PbS films.[65] Second, when SGSs are placed below PbS film, the nanodomes are formed in the top Au electrode and produces an additional surface plasmonic effect in visible region. Therefore, in SGS inside device, light intensity is locally increased from the top and bottom surfaces of PbS film, leading to an even higher light absorption in near IR regime. Third, the nanodome of Au electrode provides the second surface plasmon resonance. This surface wave propagates along PbS-Au interface and gives more chance of light absorption to the PbS film.[195] These multiple effects of SGSs improve J_{sc} of SGS inside device at plasmonic frequencies, which is manifested in IPCE spectra.

To further investigate the impact of the SGSs on the PbS-QD solar cells, we carried out numerical simulation using a finite-difference time-domain (FDTD) method. In order to do the simulation analysis of the plasmonic effect in PbS QD based solar cells, the geometric parameters were approximated from electron microscopy pictures (Fig. 5-18), and the real refractive index of the PbS QDs film was required and measured by a spectroscopic phase modulated ellipsometer (Ellipsometer VUV-NIR, Horiba Jobin Yvon), since the optical properties of the semiconductor materials are size dependent. The complex refractive index contains real part and imaginary part and described as $\dot{n}(\lambda) = n(\lambda) + ik(\lambda)$. The resulting $n(\lambda)$ and $k(\lambda)$, captured from a ~ 150 nm thick PbS QDs film deposited on quartz substrate by dip coating, are shown in Figure 5-20, in which the real values of the optical constants are much smaller than

those for bulk PbS.[196] This detection is similar to the optical parameters of lead chalcogenide QDs found elsewhere.[155, 197, 198]

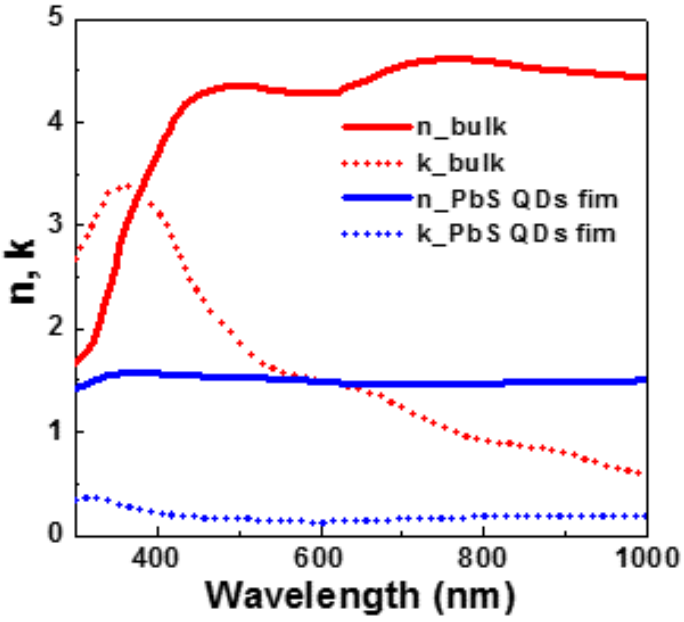

Figure 5-20. The optical constants of the PbS QDs film relative to values for bulk PbS

Schematics of the simulated structures are shown in Fig. 5-21(a) where the incident light is from the bottom. Fig. 5-21(ai) shows the control sample, which consists of a 150 nm thick PbS QD film on a 20 nm gold thin film back reflector. This structure was compared to the same active region with SGSs located in a 2D square lattice at the back side of the active region (Fig. 5-21(aii)). The optical constants for the SiO_2 and Au were taken from experimental measurement results in Palik's Handbook of Optical Constants of Solids.[199] For the 150 nm thick PbS QDs layer, the optical refractive index was directly obtained from ellipsometric measurement. The pitch of the SGSs in the simulation was 400 nm, which corresponds to the approximate density of the SGSs as observed under SEM. The SGSs consist of a silica core with 90 nm diameter, 20

nm gold intermediate layer, and 7 nm outer silica shell. The position dependent absorption per unit volume is calculated from the divergence of the Poynting vector $\vec{P}$:

$$A(r,\lambda) = \frac{1}{2} real\{\vec{\nabla} \cdot \vec{P}\} = \frac{1}{2}\epsilon_i(\lambda)\omega|\mathbf{E}(\boldsymbol{r},\lambda)|^2 \quad (5\text{-}4)$$

where εi(λ) is the imaginary part of the permittivity, ω = 2πc/λ is the photon angular frequency, c is the speed of light, and E(r, λ) is the position and wavelength-dependent electric field vector. The absorption spectra A(λ) is obtained by integrating over the PbS, $A(\lambda) = \int A(\boldsymbol{r},\lambda) dV_{PbS}$. This eliminates any parasitic absorption that may occur in the SGSs.

This eliminates any parasitic absorption that may occur in the SGSs. Results of the calculations indicate that the addition of the plasmonic SGSs enhances the absorption for wavelengths larger than 520 nm. Fig. 5-21(b) shows the local absorption per unit volume (in units of 1/nm3) for the two structures shown in Fig. 5-21(a) at λ = 680 nm where a significant increase in IPCE by SGS particles was experimentally observed (Fig. 5-19). The incident light is from the PbS QD layer toward the Au layer and the electric vector of the incident light is parallel to x-axis in the simulation. Dashed white lines indicate the location of the 150 nm thick PbS QD layer, the 20 nm thick Au reflector, as well as the outline of the SGSs. About 60% enhancement in absorption occurs through the photoactive region at this wavelength (λ = 680 nm) when the localized surface plasmon is excited by the SGS. This clearly supports the experimental observation that the SGS at the backside of the PbS film increased the IPCE by 50%.

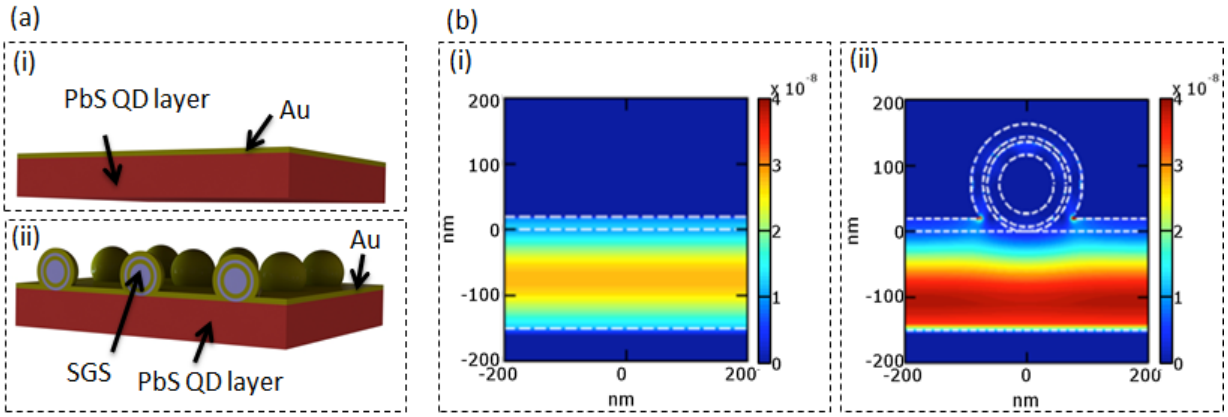

Figure 5-21. (a) Schematics of the (i) 150 nm PbS QD thin film on 20 nm Au back reflector and (ii) same structure with SGSs on the backside, (b) absorption per volume (in units of $1/nm^3$) at λ = 680 nm for the two structures (the incident light is from the bottom and hits the PbS QD layer first).

Apart from the plasmon effect introduced by SGSs on the backside of the PbS QD film, the dual effect of SGSs placed at PbS-TiO_2 interface on the light absorption was also examined theoretically. First, we simulated the PbS QD film embedded with SGS at the TiO_2/PbS interface on the assumption that Au reflector film was flat. As shown in Fig. 5-22(a), the embedded SGSs strongly enhances the absorption of light (λ = 680 nm) in the PbS QD layer due to localized surface plasmons. Quantitative comparison of the light absorption in Fig. 5-22(a) and Fig. 5-21(b) indicates that the effect of the embedded SGS is stronger than that of the SGS on the backside of Au film. This is consistent with the experimental results in Fig. 5-19. Then, we investigated the effect of introducing a curved PbS QD layer surface on the local electric field intensity concentration and the light absorption by the PbS QD film. As determined by SEM pictures, the radius of curvature of the spherical dome is 230 nm and the height is 40 nm. Fig. 5-22(b) plots the local absorption per volume at λ = 680 nm of the PbS QD layer with the curved

surface to illustrate the role of the nanodome separately. The result means that an additional increase in the local electric field intensity by the uneven surface is introduced due to scattering incident sunlight into the solar cell. These two effects may be combined to further enhance the photoactive region absorption as shown in Fig. 5-22(c). A series of simulation results supports the dual effect SGSs on the performance of PbS solar cells once the SGSs are placed between the PbS film and the TiO_2 film.

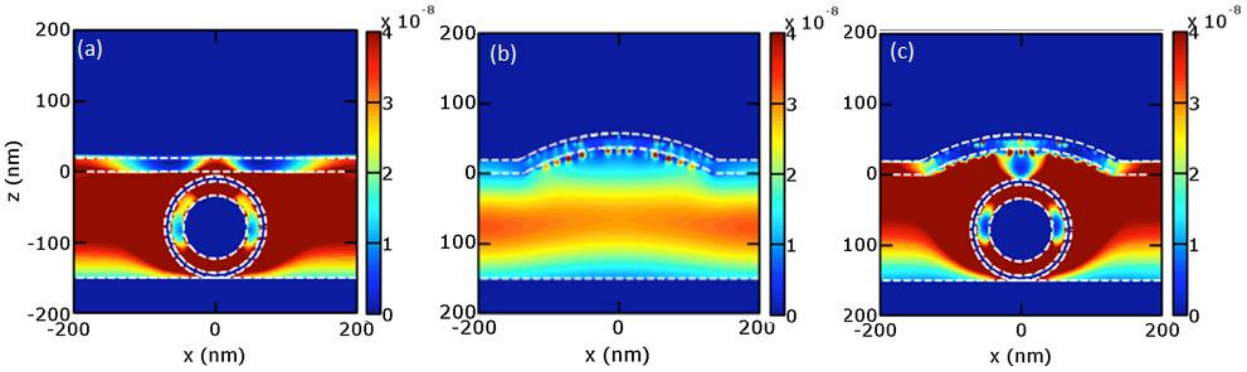

Figure 5-22. Absorption per volume at λ = 680 nm for (a) PbS QD thin film with embedded SGS, (b) PbS QD thin film with the curved PbS surface, and (c) PbS QD thin film with SGS and the curved Au surface .

In order to illustrate the possible reason why, to some extent, the V_{oc} and ff in the plasmonic assisted device are suppressed, electron lifetime (τ) of the device was measured by the open-circuit voltage decay (OCVD) technique, in which transient of V_{oc} was measured as a function of time using a 633 nm photodiode laser as the illumination source. Figure 5-23a shows the τ in different devices, calculated from the decay curves of the V_{oc}. When the SGSs are submerged into the PbS film, the electron lifetime slightly decreased, indicating a higher charge carrier recombination rate. This is due to the increased carrier diffusion length under the

protuberance of the PbS film and the decreased recombination resistance at the TiO_2/PbS interface. When the recombination rate is increase, V_{oc} and ff are lowered. On the other hand, if the SGSs are attached to the upper surface of the PbS film, the SGSs covered a part of the PbS film beneath them and blocked the Au electrode penetration, leading to insufficient Schottky contact. These result in small hollows which work as carrier recombination sites.

The electrochemical impedance spectroscopy (EIS) analysis was performed to study the internal electrical parameters of the devices. For the FTO/TiO_2/PbS/Au heterojunction device, low frequency response ranging from ~kHz to mHz corresponds to the TiO_2/PbS interface.[160] Figure 5-23b shows the Nyquist plots of the devices with and without SGSs. In order to study the impedance of the TiO_2/PbS interface, complex impedance was measured from 0.1 Hz to 1 kHz in illuminated condition under an external bias with a magnitude of open circuit voltage. The results of the impedance measurement were fitted using a ZARC element which contains a parallel resistance and a non-intuitive circuit element (CPE). The experimental data, plotted as hollow dots, are simulated using multiple ZARC elements. The results of fitting for three cases were presented in solid lines of Fig. 5-23b. Fitting results indicate that the recombination resistance is 518 Ω for the control device, 486 Ω for the SGS top case, and 406 Ω for the SGS bottom case. Lower recombination resistance means higher charge carrier recombination probability. A difference in the recombination resistance results from the non-conformal coating of PbS QDs. Since PbS films were deposited by a solution method, PbS QDs fill empty space under the SGSs in the SGS inside case. However, when Au electrode was deposited on SGS particles by E-beam evaporation technique (the SGS top case), Au did not conformally coat SGS particles and photogenerated charges of PbS QDs were temporarily trapped in the empty space and the carrier recombination rate was increased.

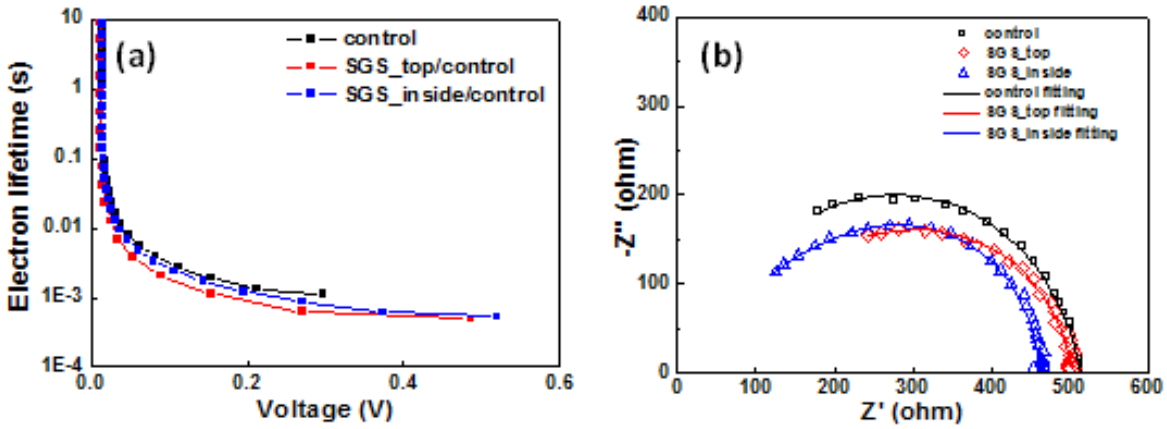

Figure 5-23. (a) Electron lifetime of the devices measured by an open-circuit voltage decay (OCVD) technique. (b) Comparison of the Nyquist plots of the devices with real data (hollow dot), generated from electrochemical impedance spectroscopy (EIS) test, and fitting data (solid line)

6.0 CONCLUSIONS AND FUTURE WORK

6.1 CONCLUSIONS

The research topics discussed in this dissertation cover the preparation of two kinds of plasmon core-shell particles, $Ag@SiO_2$ and $SiO_2@Au@SiO_2$, and their application in DSSCs and PbS QDs based thin film heterojunction solar cells, respectively. In addition, plasmon tuning effect in DSSCs has also been studied. Detail conclusions are summarized as following.

Core-shell particles coated with a uniform Ag layer were synthesized by a two-step method. Light absorption and scattering in the visible range is significantly enhanced in composite films containing the core-shell particles, leading to higher optical cross section of dyes adsorbed on the mesoporous mixed films. The effect of the core-shell particles is theoretically explained from the viewpoint of local field intensity and scattering efficiency. For 22 vol% core-shell particles, the conversion rate of incident photons to electrons increases by more than 20%. It is found that a balance among the near-field intensity, light scattering efficiency, and surface area in the photoanodes determines the energy conversion efficiency of DSCs containing core-shell particles.

Plasmon tuning effect was investigated in the DSSCs. It demonstrated that the observed light harvesting enhancement is strongly size dependent. As the size of core increases, light interacts with the surface plasmons of the core-shell particles in longer wavelength regime.

Tuning of the surface plasmons frequency is also found to benefit the energy conversion efficiency of DSSCs with different sensitizing dyes. When the extinction spectrum of the plasmonic particles is overlaid with the absorption spectrum of black dye with small optical cross section, the short circuit current of DSSCs is almost doubled, with a negligible change in the open circuit voltage. Our results provide a facile method to enhance light absorption of various dyes with different light absorption spectra, via the surface plamsons.

Another plasmonic SGSs were prepared using the seeded metallization of silica spheres, and successfully applied in the PbS based thin film heterojunction solar cell for light harvesting enhancement. The SGSs can make up improved light absorption at visible and near IR regime, 600 nm ~ 700 nm and 800 nm ~ 1000 nm which PbS QDs (~ 1.67 eV) absorb photons weakly. It proves from practical and theoretical studies that, either locating the SGSs on top of the PbS film or inside of it, enhanced light absorption is attributed to the LSPRs of the SGSs. In addition, a dual effect is realized by submerging the SGSs in the thin PbS film, since nanodome structures are formed in the top Au anode. This self-made dual plasmon resonance can be further applied to the other thin film photovoltaic devices for improved cell performance contribution.

6.2 FUTURE WORK

6.2.1 SGSs Application in DSSCs with Low Temperature UV Annealing

As mentioned above, the SGSs can enhance the light harvesting efficiency in the PbS QDs film based solar cell. Initial trial also shows that the SGSs have the potential to increase the conversion efficiency of the DSSCs, especially at longer wavelength region, since the plasmon

improved light absorption from Au nanoshell can cover a longer wavelength region comparing with that from Ag nanoshell (Fig. 6-1a). However, initial trial shows that photoanode annealing at high temperature will lose some light absorption enhancement at 600 nm ~ 900 nm (Fig. 6-1b), revealing that the Au nanoshell is not stable at high temperature, so low temperature annealing is necessary for the Au nanoshell case.

So far, low temperature photoanode annealing for DSSCs has attracted a great amount of attention due to the potential application with the low cost flexible substrate, since the melting point of the conductive polymer substrate, like polyethylene terephthalate (PET), is usually lower than 250 ^{o}C. Thus, a modified UV annealing process combing a UV lamp (λ = 354 nm) with a hot plate is demonstrated here. After annealing at 200 ^{o}C for 30 min under simultaneously UV light exposure, the optical property of the composite film is retained.

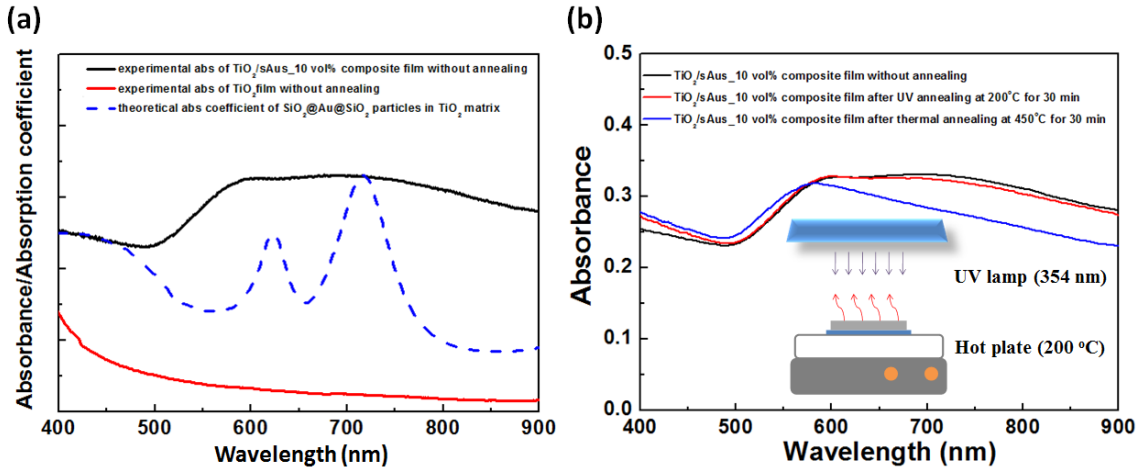

Figure 6-1. (a) Absorbance spectra of the TiO_2 and TiO_2/SGSs_10 % composite films, as well as the theoretical absorption coefficient spectrum of the SGSs. (b) Absorbance spectra of the composite film after different annealing treatments. Inset shows the schematic setup of UV annealing

6.2.2 Applying MoO_x Layer in Plasmon Assisted PbS QDs Solar Cell

We noticed that the conversion efficiency of the SGSs assisted PbS QDs solar cell is still low, which is particularly attributed to the low FF within the cell. This is because hole accumulation happens at the PbS/metal interface due to the as-formed Schottky barrier, leading to increased recombination at the interface.[200] Recently, researchers found that by sandwiching a thin MoO_x hole extraction layer between the PbS and Au film (Fig. 6-2), the FF can be improved to 47 %.[201, 202] On one hand, insertion of MoO_x layer brings in the interfacial dipole, which will enhance the band bending and facilitate the hole extraction at the PbS/MoO_x interface. On the other hand, as shown in Figure 6-2b, oxygen vacancies in the MoO_x layer will introduce gap states with edge of 0.35 eV as hole transport levels.

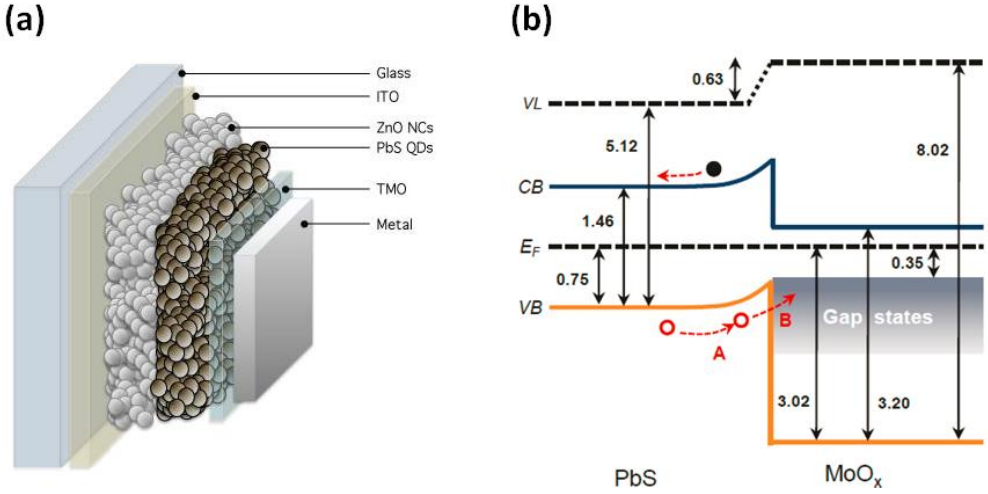

Figure 6-2. (a) Schematic PbS heterojunction solar device structure with a MoOx hole extraction layer.[200] (b) Schematic energy diagram of interfacial layers PbS/MoO_x[201]

In addition, as shown in Table 6-1, with the help of this MoO_x hole extraction layer, low cost metal, like Al, can also be used as the counter electrode without sacrificing the conversion

efficiency of the solar cell. Thus, applying an extra MoO_x layer in the SGSs assisted PbS QDs solar cell will further enhance the total conversion efficiency of the device.

Table 6-1. PbS QD Solar Cell Operation Parameters for Devices with Various Anodes[201]

anode	V_{oc} (mV)	J_{sc} (mA/cm^2)	FF (%)	PCE (%)
10 nm MoO_x/Al	524.5	17.9	48.7	4.46
20 nm MoO_x/Al	549.5	17.9	41.5	4.20
10 nm MoO_x/Ag	530.4	18.7	47.6	4.53
10 nm MoO_x/Au	540.0	17.4	47.0	4.41
Al	83.8	5.6	26.0	0.12
Ag	212.1	11.4	30.2	0.73
Au	399.5	15.5	43	2.66

BIBLIOGRAPHY

1. Barnes, W. L.; Dereux, A.; Ebbesen, T. W. *Nature* **2003,** *424*, 824.

2. Wang, H.; Goodrich, G. P.; Tam, F.; Oubre, C.; Nordlander, P.; Halas, N. J. *J. Phys. Chem. B* **2005,** *109*, 11083.

3. Maier, S. A.; Atwater, H. A. *J. Appl. Phys.* **2005,** *98*, 011101.

4. Ozbay, E. *Science* **2006,** *311*, 189.

5. Atwater, H. A. *Sci. Am.* **2007,** *296*, 56.

6. Wood, R. W. *Phil. Mag.* **1902,** *4*, 396.

7. Brongersma, M. L., *Surface Plasmon Nanophotonics*. Springer: New York, 2007.

8. Mie, G. *Ann. Phys.* **1908,** *25*, 377.

9. Ritchie, R. H. *Phys. Rev.* **1957,** *106*, 874.

10. Otto, A. *Z Phys.* **1968,** *216*, 398.

11. Kretschmann, E. R., H. *Z. Naturf.* **1968,** A 23, 2135.

12. Stewart, M. E.; Anderton, C. R.; Thompson, L. B.; Maria, J.; Gray, S. K.; Rogers, J. A.; Nuzzo, R. G. *Chem. Rev.* **2008,** *108*, 494.

13. Cunningh.Sl; Maradudi.Aa; Wallis, R. F. *Phys. Rev. B* **1974,** *10*, 3342.

14. Wark, A. W.; Lee, H. J.; Corn, R. M. *Anal. Chem.* **2005,** *77*, 3904.

15. Bohren, C. F.; Huffman, D. R., *Absorption and Scattering of Light by Small Particles*. John Wiley and Sons: New York, 1983.

16. Willets, K. A.; Van Duyne, R. P. *Ann. Rev. Phys. Chem.* **2007,** *58*, 267.

17. Kreibig, U.; Vollmer, M. *Optical Properties of Metal Clusters*. Springer: New York, 1995.

18. Su, K. H.; Wei, Q. H.; Zhang, X.; Mock, J. J.; Smith, D. R.; Schultz, S. *Nano Lett.* **2003,** *3*, 1087.

19. Grand, J.; Adam, P. M.; Grimault, A. S.; Vial, A.; De la Chapelle, M. L.; Bijeon, J. L.; Kostcheev, S.; Royer, P. *Plasmonics* **2006,** *1*, 135.

20. Prikulis, J.; Hanarp, P.; Olofsson, L.; Sutherland, D.; Kall, M. *Nano Lett.* **2004,** *4*, 1003.

21. Whitesides, G. M.; Love, J. C. *Sci. Am.* **2001,** *285*, 38.

22. Turkevitch, J. S., P. C.; Hillier, J. *Discuss. Faraday Soc.* **1951,** 11.

23. Sun, Y. G.; Xia, Y. N. *Science* **2002,** *298*, 2176.

24. Sau, T. K.; Rogach, A. L. *Adv. Mater.* **2010,** *22*, 1781.

25. Murphy, C. J.; San, T. K.; Gole, A. M.; Orendorff, C. J.; Gao, J. X.; Gou, L.; Hunyadi, S. E.; Li, T. *J. Phys. Chem. B* **2005,** *109*, 13857.

26. Perez-Juste, J.; Pastoriza-Santos, I.; Liz-Marzan, L. M.; Mulvaney, P. *Coordin. Chem. Rev.* **2005,** *249*, 1870.

27. Xia, Y. N. X., Y. J.; Lim, B. K.; Skrabalak, S. E. *Angew. Chem. Int. Ed.* **2009,** *48*, 60.

28. Sau, T. K.; Rogach, A. L.; Jackel, F.; Klar, T. A.; Feldmann, J. *Adv. Mater.* **2010,** *22*, 1805.

29. Giannini, V.; Fernandez-Dominguez, A. I.; Sonnefraud, Y.; Roschuk, T.; Fernandez-Garcia, R.; Maier, S. A. *Small* **2010,** *6*, 2498.

30. Oldenburg, S. J.; Averitt, R. D.; Westcott, S. L.; Halas, N. J. *Chem. Phys. Lett.* **1998,** *288*, 243.

31. Prodan, E.; Nordlander, P.; Halas, N. J. *Nano Lett.* **2003,** *3*, 1411.

32. Wang, H. B., D. W.; Nordlander, P.; Halas, N. J. *Acc. Chem. Res.* **2007,** *40*, 53.

33. Brinson, B. E.; Lassiter, J. B.; Levin, C. S.; Bardhan, R.; Mirin, N.; Halas, N. J. *Langmuir* **2008,** *24*, 14166.

34. Graf, C.; van Blaaderen, A. *Langmuir* **2002,** *18*, 524.

35. Loo, C.; Lin, A.; Hirsch, L.; Lee, M. H.; Barton, J.; Halas, N. J.; West, J.; Drezek, R. *Technol. Cancer Res. T.* **2004,** *3*, 33.

36. Jain, P. K.; El-Sayed, M. A. *Nano Lett.* **2007,** *7*, 2854.

37. Halas, N. J.; Lal, S.; Chang, W. S.; Link, S.; Nordlander, P. *Chem. Rev.* **2011,** *111*, 3913.

38. Halas, N. J. *Mrs Bull.* **2005,** *30*, 362.

39. Prodan, E.; Radloff, C.; Halas, N. J.; Nordlander, P. *Science* **2003,** *302*, 419.

40. Oregan, B.; Gratzel, M. *Nature* **1991,** *353*, 737.

41. Frank, A. J.; Kopidakis, N.; van de Lagemaat, J. *Coordin. Chem. Rev.* **2004,** *248*, 1165.

42. Chen, C. Y.; Wang, M. K.; Li, J. Y.; Pootrakulchote, N.; Alibabaei, L.; Ngoc-le, C. H.; Decoppet, J. D.; Tsai, J. H.; Gratzel, C.; Wu, C. G.; Zakeeruddin, S. M.; Gratzel, M. *Acs Nano* **2009,** *3*, 3103.

43. Li, L.; Hao, Y.; Yang, X. C.; Zhao, J. Z.; Tian, H. N.; Teng, C.; Hagfeldt, A.; Sun, L. C. *Chemsuschem* **2011,** *4*, 609.

44. Green, M. A.; Emery, K.; Hishikawa, Y.; Warta, W. *Prog. Photovoltaics* **2010,** *18*, 346.

45. Lee, J. K.; Yang, M. J. *Mat. Sci. & Eng. B* **2011,** *176*. 1142.

46. Robel, I.; Subramanian, V.; Kuno, M.; Kamat, P. V. *J. Am. Chem. Soc.* **2006,** *128*, 2385.

47. Tisdale, W. A.; Williams, K. J.; Timp, B. A.; Norris, D. J.; Aydil, E. S.; Zhu, X. Y. *Science* **2010,** *328*, 1543.

48. Gratzel, M. *Nature* **2001,** *414*, 338.

49. Teng, C.; Yang, X. C.; Yuan, C. Z.; Li, C. Y.; Chen, R. K.; Tian, H. N.; Li, S. F.; Hagfeldt, A.; Sun, L. C. *Org. Lett.* **2009,** *11*, 5542.

50. Sapp, S. A.; Elliott, C. M.; Contado, C.; Caramori, S.; Bignozzi, C. A. *J. Am. Chem. Soc.* **2002,** *124*, 11215.

51. Wang, M. K.; Chamberland, N.; Breau, L.; Moser, J. E.; Humphry-Baker, R.; Marsan, B.; Zakeeruddin, S. M.; Gratzel, M. *Nat. Chem.* **2010,** *2*, 385.

52. Daeneke, T.; Kwon, T. H.; Holmes, A. B.; Duffy, N. W.; Bach, U.; Spiccia, L. *Nat. Chem.* **2011,** *3*, 211.

53. Boschloo, G.; Hagfeldt, A. *Acc. Chem. Res.* **2009,** *42*, 1819.

54. Bai, Y.; Cao, Y. M.; Zhang, J.; Wang, M.; Li, R. Z.; Wang, P.; Zakeeruddin, S. M.; Gratzel, M. *Nat. Mater.* **2008,** *7*, 626.

55. Cao, Y. M.; Zhang, J.; Bai, Y.; Li, R. Z.; Zakeeruddin, S. M.; Gratzel, M.; Wang, P. *J. Phys. Chem. C* **2008,** *112*, 13775.

56. Bach, U.; Lupo, D.; Comte, P.; Moser, J. E.; Weissortel, F.; Salbeck, J.; Spreitzer, H.; Gratzel, M. *Nature* **1998,** *395*, 583.

57. Ding, I. K.; Tetreault, N.; Brillet, J.; Hardin, B. E.; Smith, E. H.; Rosenthal, S. J.; Sauvage, F.; Gratzel, M.; McGehee, M. D. *Adv. Funct. Mater.* **2009,** *19*, 2431.

58. Wang, P.; Zakeeruddin, S. M.; Comte, P.; Exnar, I.; Gratzel, M. *J. Am. Chem. Soc.* **2003,** *125*, 1166.

59. Stergiopoulos, T.; Arabatzis, I. M.; Katsaros, G.; Falaras, P. *Nano Lett.* **2002,** *2*, 1259.

60. Shah, A.; Torres, P.; Tscharner, R.; Wyrsch, N.; Keppner, H. *Science* **1999,** *285*, 692.

61. Krebs, F. C.; Tromholt, T.; Jorgensen, M. *Nanoscale* **2010,** *2*, 873.

62. Hoppe, H.; Sariciftci, N. S. *J. Mater. Res.* **2004,** *19*, 1924.

63. Deckman, H. W.; Roxlo, C. B.; Yablonovitch, E. *Opt. Lett.* **1983,** *8*, 491.

64. Polman, A. *Science* **2008,** *322*, 868.

65. Atwater, H. A.; Polman, A. *Nat. Mater.* **2010,** *9*, 205.

66. Hagglund, C.; Zach, M.; Petersson, G.; Kasemo, B. *Appl. Phys. Lett.* **2008,** 92, 053110.

67. Westphalen, M.; Kreibig, U.; Rostalski, J.; Lüth, H.; Meissner, D. *Sol. Energy Mater. Sol. C* **2000,** *61*, 97.

68. Slooff, L. H.; Veenstra, S. C.; Kroon, J. M.; Moet, D. J. D.; Sweelssen, J.; Koetse, M. M. *Appl. Phys. Lett.* **2007,** 90, 143506.

69. Moskovits, M. *Rev. Mod. Phys.* **1985,** *57*, 783.

70. Souza, G. R.; Levin, C. S.; Hajitou, A.; Pasqualini, R.; Arap, W.; Miller, J. H. *Anal. Chem.* **2006,** *78*, 6232.

71. Jiang, J.; Bosnick, K.; Maillard, M.; Brus, L. *J. Phys. Chem. B* **2003,** *107*, 9964.

72. Jackson, J. B.; Westcott, S. L.; Hirsch, L. R.; West, J. L.; Halas, N. J. *Appl. Phys. Lett.* **2003,** *82*, 257.

73. Jackson, J. B.; Halas, N. J. *P. Natl. Acad. Sci.* **2004,** *101*, 17930.

74. Kim, K.; Huang, S. W.; Ashkenazi, S.; O'Donnell, M.; Agarwal, A.; Kotov, N. A.; Denny, M. F.; Kaplan, M. J. *Appl. Phys. Lett.* **2007,** *90*, 223901.

75. Chen, Y. S.; Frey, W.; Kim, S.; Kruizinga, P.; Homan, K.; Emelianov, S. *Nano Lett.* **2011,** *11*, 348.

76. Kim, J. W.; Galanzha, E. I.; Shashkov, E. V.; Moon, H. M.; Zharov, V. P. *Nat. Nanotechnol.* **2009,** *4*, 688.

77. Oraevsky, A. A.; Karabutov, A. A.; Savateeva, E. V. *Proc. SPIE* **2001,** 4434.

78. Agarwal, A.; Huang, S. W.; O'Donnell, M.; Day, K. C.; Day, M.; Kotov, N.; Ashkenazi, S. *J. Appl. Phys.* **2007,** *102*, 064701.

79. Skrabalak, S. E.; Chen, J. Y.; Sun, Y. G.; Lu, X. M.; Au, L.; Cobley, C. M.; Xia, Y. N. *Acc. Chem. Res.* **2008,** *41*, 1587.

80. Kim, K.; Kim, H. S.; Park, H. K. *Langmuir* **2006,** *22*, 8083.

81. Pol, V. G.; Srivastava, D. N.; Palchik, O.; Palchik, V.; Slifkin, M. A.; Weiss, A. M.; Gedanken, A. *Langmuir* **2002,** *18*, 3352.

82. Jiang, Z. J.; Liu, C. Y. *J. Phys. Chem. B* **2003,** *107*, 12411.

83. Kobayashi, Y.; Salgueirino-Maceira, V.; Liz-Marzan, L. M. *Chem. Mater.* **2001,** *13*, 1630.

84. Deng, Z. W.; Chen, M.; Wu, L. M. *J. Phys. Chem. C* **2007,** *111*, 11692.

85. Brown, M. D.; Suteewong, T.; Kumar, R. S. S.; D'Innocenzo, V.; Petrozza, A.; Lee, M. M.; Wiesner, U.; Snaith, H. J. *Nano Lett.* **2011,** *11*, 438.

86. Qi, J. F.; Dang, X. N.; Hammond, P. T.; Belcher, A. M. *Acs Nano* **2011,** *5*, 7108.

87. Novotny, L.; Hecht, B.; Pohl, D. W. *J. Appl. Phys.* **1997,** *81*, 1798.

88. Prodan, E.; Nordlander, P.; Halas, N. J. *Chem. Phys. Lett.* **2003,** *368*, 94.

89. Weeber, J. C.; Dereux, A.; Girard, C.; Krenn, J. R.; Goudonnet, J. P. *Phys. Rev. B* **1999,** *60*, 9061.

90. Purcell, E. M.; Pennypac, Cr. *Astrophys. J.* **1973,** *186*, 705.

91. Draine, B. T.; Flatau, P. J. *J. Opt. Soc. Am. A* **1994,** *11*, 1491.

92. Jain, P. K.; Lee, K. S.; El-Sayed, I. H.; El-Sayed, M. A. *J. Phys. Chem. B* **2006,** *110*, 7238.

93. Taflove, A. *Computational Electrodynamics*. Artech House: Boston, 1995.

94. Vial, A.; Laroche, T. *J. Phys. D Appl. Phys.* **2007,** *40*, 7152.

95. Stratton, J. A., *Electromagnetic Theory*. McGraw-Hill: New York, 1941.

96. Smith, D. D.; Fuller, K. A. *J. Opt. Soc. Am. B* **2002,** *19*, 2449.

97. Hamann, T. W.; Jensen, R. A.; Martinson, A. B. F.; Van Ryswyk, H.; Hupp, J. T. *Energ. Environ. Sci.* **2008,** *1*, 66.

98. Argazzi, R.; Iha, N. Y. M.; Zabri, H.; Odobel, F.; Bignozzi, C. A. *Coordin. Chem. Rev.* **2004,** *248*, 1299.

99. Raether, H., *Surface Plasmons on Smooth and Rough Surfaces and on Gratings*. Springer-Verlag: Berlin, New York, 1988.

100. Hallermann, F.; Rockstuhl, C.; Fahr, S.; Seifert, G.; Wackerow, S.; Graener, H.; Plessen, G. V.; Lederer, F. *Phys. Stat. Sol. (a)* **2008,** *205*, 2844.

101. Nakayama, K.; Tanabe, K.; Atwater, H. A. *Appl. Phys. Lett.* **2008,** *93*, 121904.

102. Morfa, A. J.; Rowlen, K. L.; Reilly, T. H.; Romero, M. J.; Van de Lagemaat, J. *Appl. Phys. Lett.* **2008,** *92*, 013504.

103. Kim, S. S.; Na, S. I.; Jo, J.; Kim, D. Y.; Nah, Y. C. *Appl. Phys. Lett.* **2008,** *93*, 073307.

104. Standridge, S. D.; Schatz, G. C.; Hupp, J. T. *J. Am. Chem. Soc.* **2009,** *131*, 8407.

105. Chou, C. S.; Yang, R. Y.; Yeh, C. K.; Lin, Y. J. *Powder Technol.* **2009,** *194*, 95.

106. Wen, C. I., K.; Kishima, M.; Yamada, K. *Sol. Energ. Mat. Sol. Cells* **2000,** *61*, 339.

107. Zaban, A.; Greenshtein, M.; Bisquert, J. *Chemphyschem* **2003,** *4*, 859.

108. Bisquert, J.; Zaban, A.; Greenshtein, M.; Mora-Sero, I. *J. Am. Chem. Soc.* **2004,** *126*, 13550.

109. Nakade, S.; Kanzaki, T.; Wada, Y.; Yanagida, S. *Langmuir* **2005,** *21*, 10803.

110. Nakade, S.; Kanzaki, T.; Kambe, S.; Wada, Y. J.; Yanagida, S. *Langmuir* **2005,** *21*, 11414.

111. Wang, Q.; Moser, J. E.; Gratzel, M. *J. Phys. Chem. B* **2005,** *109*, 14945.

112. Kalyanasundaram, K. *Dye-sensitized solar cells*. EPFL Press: 2010.

113. Ding, B.; Lee, B. J.; Yang, M. J.; Jung, H. S.; Lee, J. K. *Adv. Energy Mater.* **2011,** *1*, 415.

114. Stober, W.; Fink, A.; Bohn, E. *J. Colloid Interf. Sci.* **1968,** *26*, 62.

115. Zaban, A.; Ferrere, S.; Sprague, J.; Gregg, B. A. *J. Phys. Chem. B* **1997,** *101*, 55.

116. Park, N. G.; Kim, K. M.; Kang, M. G.; Ryu, K. S.; Chang, S. H.; Shin, Y. J. *Adv. Mater.* **2005,** *17*, 2349.

117. Preston, T. C.; Signorell, R. *Acs Nano* **2009,** *3*, 3696.

118. Wei, H.; Reyes-Coronado, A.; Nordlander, P.; Aizpurua, J.; Xu, H. X. *Acs Nano* **2010,** *4*, 2649.

119. Zuloaga, J.; Prodan, E.; Nordlander, P. *Acs Nano* **2010,** *4*, 5269.

120. Lal, S.; Link, S.; Halas, N. J. *Nat. Photonics* **2007,** *1*, 641.

121. Le, F.; Brandl, D. W.; Urzhumov, Y. A.; Wang, H.; Kundu, J.; Halas, N. J.; Aizpurua, J.; Nordlander, P. *Acs Nano* **2008,** *2*, 707.

122. Love, S. A.; Marquis, B. J.; Haynes, C. L. *Appl. Spectrosc.* **2008,** *62*, 346a.

123. Loo, C.; Lowery, A.; Halas, N. J.; West, J.; Drezek, R. *Nano Lett.* **2005,** *5*, 709.

124. Hirsch, L. R.; Stafford, R. J.; Bankson, J. A.; Sershen, S. R.; Rivera, B.; Price, R. E.; Hazle, J. D.; Halas, N. J.; West, J. L. *P. Natl. Acad. Sci.* **2003,** *100*, 13549.

125. Sershen, S. R.; Westcott, S. L.; Halas, N. J.; West, J. L. *J. Biomed. Mater. Res.* **2000,** *51*, 293.

126. Huang, C. Y.; Hsu, Y. C.; Chen, J. G.; Suryanarayanan, V.; Lee, K. M.; Ho, K. C. *Sol. Energ. Mat. Sol. C* **2006,** *90*, 2391.

127. Kang, M. G.; Ryu, K. S.; Chang, S. H.; Park, N. G.; Hong, J. S.; Kim, K. J. *B Kor. Chem. Soc.* **2004,** *25*, 742.

128. Chou, C. S.; Yang, R. Y.; Yeh, C. K.; Lin, Y. J. *Powder. Technol.* **2009,** *194*, 95.

129. Gratzel, M. *Prog. Photovoltaics* **2000,** *8*, 171.

130. Hara, K.; Nishikawa, T.; Kurashige, M.; Kawauchi, H.; Kashima, T.; Sayama, K.; Alka, K.; Arakawa, H. *Sol. Energ. Mat. Sol. C* **2005,** *85*, 21.

131. Altobello, S.; Argazzi, R.; Caramori, S.; Contado, C.; Da Fre, S.; Rubino, P.; Chone, C.; Larramona, G.; Bignozzi, C. A. *J. Am. Chem. Soc.* **2005,** *127*, 15342.

132. Wang, Z. S.; Cui, Y.; Dan-Oh, Y.; Kasada, C.; Shinpo, A.; Hara, K. *J. Phys. Chem. C* **2007,** *111*, 7224.

133. Chang, S.; Li, Q.; Xiao, X. D.; Wong, K. Y.; Chen, T. *Energ. Environ. Sci*. **2012,** *5*, 9444.

134. Averitt, R. D.; Sarkar, D.; Halas, N. J. *Phys. Rev. Lett.* **1997,** *78*, 4217.

135. Wang, Z. S.; Kawauchi, H.; Kashima, T.; Arakawa, H. *Coordin. Chem. Rev.* **2004,** *248*, 1381.

136. Ding, B.; Yang, M. J.; Lee, B. J.; Lee, J. K. *RSC Advances* **2013,** *3*, 9690.

137. Nazeeruddin, M. K.; Kay, A.; Rodicio, I.; Humphrybaker, R.; Muller, E.; Liska, P.; Vlachopoulos, N.; Gratzel, M. *J. Am. Chem. Soc.* **1993,** *115*, 6382.

138. Nazeeruddin, M. K.; Pechy, P.; Renouard, T.; Zakeeruddin, S. M.; Humphry-Baker, R.; Comte, P.; Liska, P.; Cevey, L.; Costa, E.; Shklover, V.; Spiccia, L.; Deacon, G. B.; Bignozzi, C. A.; Gratzel, M. *J. Am. Chem. Soc.* **2001,** *123*, 1613.

139. Lee, S.; Cho, I. S.; Lee, J. H.; Kim, D. H.; Kim, D. W.; Kim, J. Y.; Shin, H.; Lee, J. K.; Jung, H. S.; Park, N. G.; Kim, K.; Ko, M. J.; Hong, K. S. *Chem. Mater.* **2010,** *22*, 1958.

140. Huang, F. Z.; Chen, D. H.; Zhang, X. L.; Caruso, R. A.; Cheng, Y. B. *Adv. Funct. Mater.* **2010,** *20*, 1301.

141. Lee, J. K.; Jeong, B. H.; Jang, S. I.; Yeo, Y. S.; Park, S. H.; Kim, J. U.; Kim, Y. G.; Jang, Y. W.; Kim, M. R. *J. Mater. Sci.-Mater. El.* **2009,** *20*, 446.

142. Talapin, D. V.; Lee, J. S.; Kovalenko, M. V.; Shevchenko, E. V. *Chem. Rev.* **2010,** *110*, 389.

143. Tang, J. A.; Sargent, E. H. *Adv. Mater.* **2011,** *23*, 12.

144. Hines, M. A.; Scholes, G. D. *Adv. Mater.* **2003,** *15*, 1844.

145. McDonald, S. A.; Konstantatos, G.; Zhang, S. G.; Cyr, P. W.; Klem, E. J. D.; Levina, L.; Sargent, E. H. *Nat. Mater.* **2005,** *4*, 138.

146. Nozik, A. J. *Annu. Rev. Phys. Chem.* **2001,** *52*, 193.

147. Nozik, A. J. *Physica E* **2002,** *14*, 115.

148. Ellingson, R. J.; Beard, M. C.; Johnson, J. C.; Yu, P. R.; Micic, O. I.; Nozik, A. J.; Shabaev, A.; Efros, A. L. *Nano Lett.* **2005,** *5*, 865.

149. Sukhovatkin, V.; Hinds, S.; Brzozowski, L.; Sargent, E. H. *Science* **2009,** *324*, 1542.

150. Sambur, J. B.; Novet, T.; Parkinson, B. A. *Science* **2010,** *330*, 63.

151. Semonin, O. E.; Luther, J. M.; Choi, S.; Chen, H. Y.; Gao, J. B.; Nozik, A. J.; Beard, M. C. *Science* **2011,** *334*, 1530.

152. Sargent, E. H. *Adv. Mater.* **2008,** *20*, 3958.

153. Klem, E. J. D.; MacNeil, D. D.; Levina, L.; Sargent, E. H. *Adv. Mater.* **2008,** *20*, 3433.

154. Koleilat, G. I.; Levina, L.; Shukla, H.; Myrskog, S. H.; Hinds, S.; Pattantyus-Abraham, A. G.; Sargent, E. H. *Acs Nano* **2008,** *2*, 833.

155. Law, M.; Beard, M. C.; Choi, S.; Luther, J. M.; Hanna, M. C.; Nozik, A. J. *Nano Lett.* **2008,** *8*, 3904.

156. Luther, J. M.; Law, M.; Beard, M. C.; Song, Q.; Reese, M. O.; Ellingson, R. J.; Nozik, A. J. *Nano Lett.* **2008,** *8*, 3488.

157. Law, M.; Luther, J. M.; Song, O.; Hughes, B. K.; Perkins, C. L.; Nozik, A. J. *J. Am. Chem. Soc.* **2008,** *130*, 5974.

158. Luther, J. M.; Law, M.; Song, Q.; Perkins, C. L.; Beard, M. C.; Nozik, A. J. *Acs Nano* **2008,** *2*, 271.

159. Pattantyus-Abraham, A. G.; Kramer, I. J.; Barkhouse, A. R.; Wang, X. H.; Konstantatos, G.; Debnath, R.; Levina, L.; Raabe, I.; Nazeeruddin, M. K.; Gratzel, M. Sargent. E. H. *ACS Nano* **2010,** *4*, 3374.

160. Etgar, L.; Moehl, T.; Gabriel, S.; Hickey, S. G.; Eychmuller, A.; Gratzel, M. *Acs Nano* **2012,** *6*, 3092.

161. Luther, J. M.; Gao, J. B.; Lloyd, M. T.; Semonin, O. E.; Beard, M. C.; Nozik, A. J. *Adv. Mater.* **2010,** *22*, 3704.

162. Barkhouse, D. A. R.; Pattantyus-Abraham, A. G.; Levina, L.; Sargent, E. H. *Acs Nano* **2008,** *2*, 2356.

163. Johnston, K. W.; Pattantyus-Abraham, A. G.; Clifford, J. P.; Myrskog, S. H.; Hoogland, S.; Shukla, H.; Klem, J. D.; Levina, L.; Sargent, E. H. *Appl. Phys. Lett.* **2008,** *92*, 122111.

164. Gao, J. B.; Luther, J. M.; Semonin, O. E.; Ellingson, R. J.; Nozik, A. J.; Beard, M. C. *Nano Lett.* **2011,** *11*, 1002.

165. Szendrei, K.; Gomulya, W.; Yarema, M.; Heiss, W.; Loi, M. A. *Appl. Phys. Lett.* **2010,** *97*, 061103.

166. Klem, E. J. D.; Shukla, H.; Hinds, S.; MacNeil, D. D.; Levina, L.; Sargent, E. H. *Appl. Phys. Lett.* **2008,** *92*, 151115.

167. Turyanska, L.; Elfurawi, U.; Li, M.; Fay, M. W.; Thomas, N. R.; Mann, S.; Blokland, J. H.; Christianen, P. C. M.; Patane, A. *Nanotechnology* **2009,** *20*, 315604.

168. Baik, S. J.; Kim, K.; Lim, K. S.; Jung, S.; Park, Y. C.; Han, D. G.; Lim, S.; Yoo, S.; Jeong, S. *J. Phys. Chem. C* **2011,** *115*, 607.

169. Zhao, N.; Osedach, T. P.; Chang, L. Y.; Geyer, S. M.; Wanger, D.; Binda, M. T.; Arango, A. C.; Bawendi, M. G.; Bulovic, V. *Acs Nano* **2010,** *4*, 3743.

170. Gao, J. B.; Jeong, S.; Lin, F.; Erslev, P. T.; Semonin, O. E.; Luther, J. M.; Beard, M. C. *Appl. Phys. Lett.* **2013,** *102*, 043506.

171. Ferry, V. E.; Verschuuren, M. A.; Li, H. B. T.; Verhagen, E.; Walters, R. J.; Schropp, R. E. I.; Atwater, H. A.; Polman, A. *Opt. Express* **2010,** *18*, A237.

172. Spinelli, P.; Ferry, V. E.; van de Groep, J.; van Lare, M.; Verschuuren, M. A.; Schropp, R. E. I.; Atwater, H. A.; Polman, A. *J. Optics* **2012,** *14*, 24002.

173. Deceglie, M. G.; Ferry, V. E.; Alivisatos, A. P.; Atwater, H. A. *Nano Lett.* **2012,** *12*, 2894.

174. Ding, I. K.; Zhu, J.; Cai, W. S.; Moon, S. J.; Cai, N.; Wang, P.; Zakeeruddin, S. M.; Gratzel, M.; Brongersma, M. L.; Cui, Y.; McGehee, M. D. *Adv. Energy Mater.* **2011,** *1*, 52.

175. Li, X. H.; Choy, W. C. H.; Huo, L. J.; Xie, F. X.; Sha, W. E. I.; Ding, B. F.; Guo, X.; Li, Y. F.; Hou, J. H.; You, J. B.; Yang, Y. *Adv. Mater.* **2012,** *24*, 3046.

176. Wang, D. H.; Kim, D. Y.; Choi, K. W.; Seo, J. H.; Im, S. H.; Park, J. H.; Park, O. O.; Heeger, A. J. *Angew. Chem. Int. Edit* **2011,** *50*, 5519.

177. Kulkarni, A. P.; Noone, K. M.; Munechika, K.; Guyer, S. R.; Ginger, D. S. *Nano Lett.* **2010,** 10, (4), 1501-1505.

178. Schwartzberg, A. M.; Olson, T. Y.; Talley, C. E.; Zhang, J. Z. *J. Phys. Chem. B* **2006,** *110*, 19935.

179. Chen, J. Y.; McLellan, J. M.; Siekkinen, A.; Xiong, Y. J.; Li, Z. Y.; Xia, Y. N. *J. Am. Chem. Soc.* **2006,** *128*, 14776.

180. Skrabalak, S. E.; Chen, J. Y.; Sun, Y. G.; Lu, X. M.; Au, L.; Cobley, C. M.; Xia, Y. N. *Accounts Chem. Res.* **2008,** *41*, 1587.

181. Wang, H.; Wu, Y. P.; Lassiter, B.; Nehl, C. L.; Hafner, J. H.; Nordlander, P.; Halas, N. J. *P. Natl. Acad. Sci.* **2006,** *103*, 10856.

182. Lassiter, J. B.; Knight, M. W.; Mirin, N. A.; Halas, N. J. *Nano Lett.* **2009,** *9*, 4326.

183. Lu, Y.; Liu, G. L.; Kim, J.; Mejia, Y. X.; Lee, L. P. *Nano Lett.* **2005,** *5*, 119.

184. Sau, T. K.; Murphy, C. J. *Langmuir* **2004,** *20*, 6414.

185. Dreaden, E. C.; Alkilany, A. M.; Huang, X. H.; Murphy, C. J.; El-Sayed, M. A. *Chem. Soc. Rev.* **2012,** *41*, 2740.

186. Huang, X. H.; El-Sayed, I. H.; Qian, W.; El-Sayed, M. A. *J. Am. Chem. Soc.* **2006,** *128*, 2115.

187. Dang, X. N.; Qi, J. F.; Klug, M. T.; Chen, P. Y.; Yun, D. S.; Fang, N. X.; Hammond, P. T.; Belcher, A. M. *Nano Lett.* **2013,** *13*, 637.

188. Paz-Soldan, D.; Lee, A.; Thon, S. M.; Adachi, M. M.; Dong, H.; Maraghechi, P.; Yuan, M.; Labelle, A. J.; Hoogland, S.; Liu, K.; Kumacheva, E.; Sargent, E. H. *Nano Lett.* **2013,** *13*, 1502.

189. Tang, J.; Kemp, K. W.; Hoogland, S.; Jeong, K. S.; Liu, H.; Levina, L.; Furukawa, M.; Wang, X. H.; Debnath, R.; Cha, D. K.; Chou, K. W.; Fischer, A.; Amassian, A.; Asbury, J. B.; Sargent, E. H. *Nat. Mater.* **2011,** *10*, 765.

190. Watts, J. F.; Wolstenholme, J.; Wiley, J. *An introduction to surface analysis by XPS and AES*. Wiley Online Library: 2003.

191. Graf, C.; Vossen, D. L. J.; Imhof, A.; Van Blaaderen, A. *Langmuir* **2003,** *19*, 6693.

192. Duff, D. G.; Baiker, A.; Edwards, P. P. *Langmuir* **1993,** *9*, 2301.

193. Wang, H.; Brandl, D. W.; Le, F.; Nordlander, P.; Halas, N. J. *Nano Lett.* **2006,** *6*, 827.

194. Li, J. F.; Huang, Y. F.; Ding, Y.; Yang, Z. L.; Li, S. B.; Zhou, X. S.; Fan, F. R.; Zhang, W.; Zhou, Z. Y.; Wu, D. Y.; Ren, B.; Wang, Z. L.; Tian, Z. Q. *Nature* **2010,** *464*, 392.

195. Ferry, V. E.; Sweatlock, L. A.; Pacifici, D.; Atwater, H. A. *Nano Lett.* **2008,** *8*, 4391.

196. Kanazawa, H.; Adachi, S. *J. Appl. Phys.* **1998,** *83*, 5997.

197. Paquet, C.; Yoshino, F.; Levina, L.; Gourevich, I.; Sargent, E. H.; Kumacheva, E. *Adv. Funct. Mater.* **2006,** *16*, 1892.

198. Ehrler, B.; Wilson, M. W. B.; Rao, A.; Friend, R. H.; Greenham, N. C. *Nano Lett.* **2012,** *12*, 1053.

199. Palik, E. D., *Handbook of Optical Constants of Solids*. Academic Press: 1997.

200. Gao, J. B.; Jeong, S. H.; Semonin, O. E.; Ellingso, R. J.; Nozik, A. J.; Beard, M. C., Annealing Effect of PbS Quantum Dot Solar Cells. In *Photovoltaic Specialists Conference (PVSC), 2011 37th IEEE*, Seattle, WA, 2011; pp 002619.

201. Gao, J. B.; Perkins, C. L.; Luther, J. M.; Hanna, M. C.; Chen, H. Y.; Semonin, O. E.; Nozik, A. J.; Ellingson, R. J.; Beard, M. C. *Nano Lett.* **2011,** *11*, 3263.

202. Jean, J.; Chang, S.; Brown, P. R.; Cheng, J. J.; Rekemeyer, P. H.; Bawendi, M. C.; Gradecak, S.; Bulovic, V. *Adv. Mater.* **2013,** *25*, 2790.